Model-supported identification of the reaction kinetics in lithium-sulfur batteries

Von der Fakultät für Maschinenbau
der Technischen Universität Carolo-Wilhelmina zu Braunschweig

zur Erlangung der Würde

einer Doktor-Ingenieurin oder eines Doktor-Ingenieurs (Dr.-Ing.)

genehmigte Dissertation

von: M.Sc. Patrick Schön
geboren in (Geburtsort): Hannover

eingereicht am: 23.01.2020
mündliche Prüfung am: 16.06.2020

Vorsitz: Frau Prof. Dr.-Ing. Ulrike Krewer
Gutachter: Herr Prof. Dr. Georg Garnweitner

2021

Acknowledgements

This dissertation thesis presents the major results of my research work performed between 2015 and 2019 at the Institute of Energy and Process Systems Engineering of the Technische Universität Braunschweig. First, I would like to express my deepest appreciation to Prof. Dr.-Ing. Ulrike Krewer for giving me the unique opportunity to work in her group along with a great team, for her continuous guidance and advice, whether scientific or personal. Further, my gratitude to the doctorate examination committee, the second examiner Prof. Dr. Georg Garnweitner and the chairman Prof. Dr. Julia Großeheilmann.

I also very much appreciate meeting my colleagues at InES, Theresa Haisch, Nicolas Wolff, Marco Heinrich, Fridolin Röder, Florian Baakes, Fabian Kubannek, Vincent Laue, Georg Lenze, Oke Schmidt and Maximilian Röhe, who made me enjoy the time at the institute. It was a real pleasure sharing my office with Nina Harting, I would not have missed out the nice conversations and her friendship. I would also like to acknowledge my former students Kerstin Hadler, Markus Nöske, Artak Müller, Frederik Hintz, Jintian Liu and Rajendra Singh Negi for supporting parts of the experimental and simulatien work. Furthermore, of course, thanks to Ina Schunke, Elke Drömer, Dr.-Ing. Horst Müller and Wilfried Janßen for the administrative and technical support.

I want to express my deep gratitude to my family for a lot of love and support throughout my education and for being such an important part in my life. To my child Keno, who makes me smile everyday and loves his dad no matter what.

The completion of my dissertation would not have been possible without the support and patience of my beloved wife Inga. I cannot express how grateful I am for her encouragement, motivation and love, when I spent countless hours on this thesis, that I should have spent with her.

Finally, I also wish to thank Michael Ende. The wisdom he shared with the world paved my way to finally get the work done!

"You see, Momo,' he [Beppo Roadsweeper] told her one day, 'it's like this. Sometimes, when you've a very long street ahead of you, you think how terribly long it is and feel sure you'll never get it swept.' He gazed silently into space before continuing. 'And then you start to hurry,' he went on. 'You work faster and faster, and every time you look up there seems to be just as much left to sweep as before, and you try even harder, and you panic, and in the end you're out of breath and have to stop - and still the street stretches away in front of you. That's not the way to do it.' He pondered a while. Then he said, 'You must never think of the whole street at once, understand? You must only concentrate on the next step, the next breath, the next stroke of the broom, and the next, and the next. Nothing else.' Again he paused for thought before adding, 'That way you enjoy your work, which is important, because then you make a good job of it. And that's how it ought to be.' There was another long silence. At last he went on, 'And all at once, before you know it, you find you've swept the whole street clean, bit by bit. What's more, you aren't out of breath.' He nodded to himself. 'That's important, too,' he concluded."

Michael Ende

Abstract

The current debate about replacing lithium-ion battery technology with a safer, more environmental friendly and affordable alternative, drives the breakthrough of lithium-sulfur batteries to the marked. The most severe limitations of this conversion battery on a cell level are linked to the reaction mechanism, which therefore represents a key feature of knowledge driven development. This study applies a complementary set of chemical and electrochemical characterization methods, including cyclic voltammetry, HPLC and galvanostatic discharge and computational simulation of cyclic voltammetry, to examine the reaction kinetics of sulfur reduction in detail. Cyclic voltammetry in combination with galvanostatic discharge and open circuit potential measurement reveals the electron transfer and chemical reactions at different states of charge, HPLC/MS determines dissolved sulfur quantitatively and dissolved polysulfides qualitatively in the electrolyte during the discharge processes. An E3C4-mechanism is proposed as reaction mechanism, based on the results of the conducted experiments and literature findings. The mechanism is able to reproduce the current signal of cyclic voltammetry experiments, showing all important characteristics. Besides the electrochemical reduction reactions of S_8 and S_8^{2-} during the higher voltage discharge plateau and the S_4^{2-} reduction during the lower voltage discharge plateau, circular routes by chemical reactions, that support a deeper discharge of the cell by producing S_8 and S_4^{2-}, are proven. The chemical reactions are also balanced to match the HPLC results, which revealed that short chain polysulfides, S_3^{2-} and S_4^{2-}, are favored. Although, sulfur is still present in bulk during the lower voltage discharge plateau, it is chemically converted to S_4^{2-} before reaching the electrode/electrolyte interface.

Cycling experiments of lithium-sulfur coin cells uncovered the current dependency of the higher and lower voltage discharge plateau. It can be explained by the circular routes of the mechanism since the conversion reaction is time dependent and therefore significantly influenced by the applied current.

This work gives detailed information about the proposed mechanism that enables improved analysis of the shuttle mechanism, Li_2S precipitation or overall cell performance. The proposed mechanism represents a great advance in the development of lithium-sulfur batteries by implementing a physically correct view in the interpretation of experimental results and modeling.

Kurzfassung

Die aktuelle Debatte die Lithium-Ionen Batterietechnologie mit einer sichereren, umweltfreundlicheren und kostengünstigeren Alternative zu ersetzen, bietet für die Lithium-Schwefel Batterie die Chance durch fortlaufende Entwicklung die Kommerzialisierung zu erreichen. Die maßgeblichen Limitierungen dieser Konversionsbatterie sind alle verbunden mit dem Reaktionsmechanismus von Schwefel, welcher daher ein wichtigen Baustein zur wissensbasierten Weiterentwicklung der Technologie darstellt. In dieser Arbeit wurden sich ergänzende Methoden der elektrochemischen und chemischen Analyse verwendet, um die Reaktionskinetik von Schwefel im Detail zu analysieren. Diese umfassen Cyclovoltammetrie, HPLC und galvanostatische Entladung und wurden durch die Simulation von Cyclovoltammetrieexperimenten im zuvor implementierten Modell ergänzt. Cyclovoltammetrie in Verbindung mit galvanostatischer Entladung und der Messung der Leerlaufspannung machten die elektrochemischen und chemischen Reaktionen bei verschiedenen Entladezuständen der Zelle sichtbar. Mittels HPLC/MS ließ sich die Konzentration von Schwefel im Entladeverlauf quantitativ bestimmen, die Konzentrationsverläufe der Polysulfide über die Entladung konnten qualitativ bestimmt werden. Basierend auf diesen Ergebnissen und den Erkenntnissen der Literatur wird ein E3C4-Mechanismus empfohlen. Die Simulation mit diesem Mechanismus zeigt übereinstimmende Ströme im Cyclovoltammogram mit den Experimenten. Alle charakteristischen Merkmale im Kurvenverlauf werden reproduziert. Neben den bekannten elektrochemischen Reduktionen von S_8 und S_8^{2-} auf dem oberen Spannungsplateau der Entladekurve und der Reduktion von S_4^{2-} auf dem unteren Spannungsplateau der Entladekurve, konnte zyklische Routen belegt werden, welche S_8 und S_4^{2-} reproduzieren und eine tiefere Entladung unterstützen. Das Gleichgewicht der chemischen Reaktionen wurde so gewählt, dass die HPLC Ergebnisse, welche S_3^{2-} und S_4^{2-} als primäre Produkte zeigen, berücksichtigt wurden. Obwohl S_8 im Elektrolyt auch während des unteren Spannungsplateaus vorhanden

ist, erreicht es durch eine Umwandlung zu S_4^{2-} nicht mehr die Elektrodenoberfläche. Es reagiert daher chemisch und nicht mehr elektrochemisch.

Zyklisierung von Lithium-Schwefel Knopfzellen zeigte die Abhängigkeit des oberen und unteren Spannungsplateaus von der applizierten Stromstärke während der Entladung. Die Erklärung liegt im Mechanismus. Die chemischen Reaktionen, welche S_8 und S_4^{2-} auf den beiden Plateaus bereitstellen, sind zeitabhängig. Daher wird die Produktion von Substrat für die elektrochemische Reduktion erheblich von der Stromstärke beeinflusst.

Diese Arbeit stellt detaillierte Informationen über den empfohlenen Reaktionsmechanismus bereit. Dieser ermöglicht es zukünftigen Studien einen tieferen Einblick in die limitierenden Prozesse der Lithium-Schwefel Batterie zu erhalten. Analysen des Shuttle-Mechanismus, des Ausfallens von Li_2S oder der Gesamtperformance der Zellen profitieren von der detaillierten Abbildung der inneren Abläufe. Der empfohlene Reaktionsmechanismus repräsentiert daher einen großen Schritt für die Entwicklung von Lithium-Schwefel Batterien, indem er physikalisch korrekte Einblicke in die Interpretation experimenteller Ergebnisse und die Modellierung gewährt.

Publications within this thesis

- Model based and experimental analysis of sulfur reduction; Patrick Schön, Ulrike Krewer; Poster, Electrochemistry 2016, Goslar
- Titscher, P., Schön, P., Horst, M., Krewer, U., & Kwade, A. (2018). Increasing Energy Densities of Sulfur Cathodes using Dispersing and Calendering Processes for Lithium–Sulfur Batteries. Energy Technology, 6(6), 1139-1147.
- Model-supported identification of LiS reduction mechanism and kinetics; Patrick Schön, Ulrike Krewer; Vortrag, Electrochemistry 2018, Ulm
- Identifying Sulfur Reduction Kinetics for Li-Sulfur Batteries; Patrick Schön, Ulrike Krewer; Vortrag, ISE 2018, Bologna
- Schön, P., Hintz, F., & Krewer, U. (2019). Electrochemical analysis of the reaction mechanism of sulfur reduction as a function of state of charge. Electrochimica Acta, 295, 926-933.
- Schön, P., & Krewer, U. (2021). Revealing the complex sulfur reduction mechanism using cyclic voltammetry simulation. Electrochimica Acta, 373, 137523.

Contents

List of Figures

List of Tables

Acronyms

C_{18}	octadecyl carbon xvi, 34, 35, 54
Li^+	lithium ion 1, 4–6
Li_2S_2	lithium disulfide 16, 17, 43
Li_2S_n	lithium polysulfide 3
Li_2S	lithium sulfide 4–8, 11, 15–17, 43, 95
Li	lithium 1, 3–7, 14, 39, 40, 54
S_2^{2-}	disulfide 8, 16, 50, 68, 79, 81, 82, 85
S_3^{2-}	trisulfide 16, 50, 58, 82, 85, 99
S_4^{2-}	tetrasulfide 8, 14, 16, 42, 50, 51, 57, 58, 68, 79, 81, 85, 99–101
S_5^{2-}	pentasulfide 16
S_8^{2-}	octasulfide 8, 12, 16, 42, 49, 51, 57, 59, 68, 79
S_8^{4-}	octasulfide 42, 49, 50, 79, 81, 99
S_8	cyclic octasulfur xxi, 3–8, 11, 12, 14–19, 40, 42, 43, 45, 46, 49, 51–55, 57–59, 61, 62, 66, 68, 70, 71, 78, 79, 81, 82, 84–86, 89–93, 95, 96, 98–101
S^{2-}	sulfide 8, 46, 51, 53, 58, 59, 66, 71, 79, 81, 82, 85, 86, 99, 100
m/z-ratio	mass-to-charge ratio 36, 37, 54
APCI	atmospheric-pressure chemical ionization 36, 54
b	backward 31
CV	cyclic voltammetry xvii, 8, 14, 15, 18, 19, 21–23, 25, 29, 39–44, 47, 49, 51, 57, 59, 61, 63–65, 68, 70, 71, 73, 74, 76–78, 81, 84–86, 99, 100

CVG	cyclic voltammogram 15, 18, 23, 25, 26, 29, 40, 43, 47, 49, 51, 62, 64, 99
DAD	diode array detector 54
DME	1,2-dimethoxyethane 3, 14, 15, 39, 40, 42, 49, 54, 70, 84
DMSO	dimethyl sulfoxide 14, 15
DOL	1,3-Dioxolan 3, 14, 15, 39, 40, 42, 49, 54, 55, 70, 84
E/S	electrolyte/sulfur 17
ed	educt of a reaction 31
EPR	electron paramagnetic resonance 17
ESI	electrospray ionization 36
f	forward 31
GT	galvanostatic discharge 4, 6, 14, 16, 18, 19, 51, 53–55, 57, 58, 79, 99, 100
HPLC	high performance liquid chromatography 8, 16, 18, 33, 34, 36, 52–55, 57, 58, 61, 68, 81, 84, 99
ICP-OES	inductively coupled plasma optical emission spectrometry 16
LC-MS	liquid chromatography with mass spectrometry 16
LIB	lithium-ion battery 1, 3, 81, 89
LiTFSI	bis(trifluoromethane)sulfonimide lithium salt 39, 40, 42, 49, 54, 70
LSB	lithium-sulfur battery 3–6, 8, 14, 16–19, 46, 53, 55, 61, 86, 87, 89, 90, 96, 98–101
MeOTf	methyl trifluoromethanesulfonate 54

MS	mass spectrometry 8, 33, 35, 36, 53–55, 57, 58
OCP	open circuit potential 39, 40, 43–49, 51, 68, 99
OCV	open circuit voltage 82, 92, 93, 96
prod	product of a reaction 31
PS	polysulfide 3, 4, 7, 15–17, 46, 47, 58, 61, 66, 99
RP-HPLC	reverse phase chromatography 34
RRDE	rotating ring disk electrode 14, 15
SEI	solid electrolyte interface 5
SoC	state of charge 3, 6, 18, 41, 51–55, 57, 68, 81, 86, 99
UHPLC	ultra high performance liquid chromatography 34
UV-Vis	ultraviolet–visible spectrophotometry xvi, 33, 35, 36

Symbols

α	transfer coefficient	
γ	activity coefficient	
A_λ	absorbance at wavelength λ	
c	concentration of analyte in solution	$\mathrm{mol\,m^{-3}}$
D	diffusion coefficient	$\mathrm{m^2\,s^{-1}}$
δ	thickness of the diffusion layer	m
$\Delta E_{\mathrm{p}/2}$	half-wave peak potential	V
Δx_{f}	size of volume element	m
E	potential	V
E_0	standard potential	V
$E_{\mathrm{f},0}$	formal potential	V
ϵ_λ	absorbitivity of species at wavelength λ	$\mathrm{m^3\,mol^{-1}\,m^{-1}}$
ℓ	optical path length	m
E_{p}	anodic peak potential	V
$E_{\mathrm{p,a}}$	anodic peak potential	V
$E_{\mathrm{p,c}}$	cathodic peak potential	V
F	Faraday constant ($96\,485.33\,\mathrm{A\,s\,mol^{-1}}$)	$\mathrm{A\,s\,mol^{-1}}$
I	current	A
i	current density	$\mathrm{A\,m^{-2}}$
i_{p}	peak current density	$\mathrm{A\,m^{-2}}$
$i_{\mathrm{p,a}}$	anodic peak current density	$\mathrm{A\,m^{-2}}$
$i_{\mathrm{p,c}}$	cathodic peak current density	$\mathrm{A\,m^{-2}}$
k	chemical reaction rate constant	$\mathrm{mol^{1-\sum\nu}m^{3(\sum\nu-1)}s^{-1}}$
L	distance between electrolyte and bulk	m
λ	wavelength	m
m	molar mass	$\mathrm{kg\,mol^{-1}}$
n	number of electrons transferred per mole	

ν	stoechiometric coefficient	
Q	total number of volume elements	
q	number of volume element	
R	gas constant ($8.314\,\mathrm{J\,mol^{-1}\,K^{-1}}$)	$\mathrm{J\,mol^{-1}\,K^{-1}}$
r	chemical reaction rate	$\mathrm{mol\,m^{-3}\,s^{-1}}$
R	resistance	Ω
S	source term in mass balance	$\mathrm{mol\,m^{-3}\,s^{-1}}$
T	absolute temperature	K
t	time	s
U	cell voltage	V
U^0	open circuit voltage	V
v	scan rate	$\mathrm{V\,s^{-1}}$
w	growth factor	
x	distance normal to the electrode surface	m
z	ionic charge	

Glossary

E-mechanism Mechanism with one electron transfer reaction. 23, 26

EEC$_{irr}$-mechanism Two electron transfer reactions with a subsequent irreversible chemical follow-up reaction. xxi, 62, 65–68, 70, 71, 73, 78, 79, 84–86, 99

EC$_{irr}$-mechanism Electron transfer with a subsequent first-order, irreversible chemical follow-up reaction. xv, 23, 26, 28

EC$_{rev}$-mechanism Electron transfer with a subsequent first-order, reversible chemical follow-up reaction. 23, 29

EE-mechanism Mechanism with two electron transfer reactions. xv, 23, 25

E3C4-mechanism Physically motivated reaction mechanism to represent S_8 reduction. xxi, 62, 65, 68, 69, 71, 72, 78, 79, 86

Chapter 1

Introduction[1]

1.1 Motivation

In 1991, Sony Corporation commercialized the first lithium-ion battery (LIB) [2], which has profoundly affected our daily life ever since. Especially, in powering portable electronic devices and electric vehicles LIBs are currently dominant in the market of secondary batteries. Advancements over the past 28 years increased the practical gravimetric and volumetric energy density of LIBs at cell level to $700\,\mathrm{W\,h\,L^{-1}}$ and $260\,\mathrm{W\,h\,kg^{-1}}$ [3, 4]. Regarding the rapidly increasing demands of portable electronic devices, stationary energy storage and electric vehicles, batteries with a higher energy density are urgently needed. However, the underlying intercalation chemistry of LIBs restricts the energy density, which is already approaching its theoretical physical maximum [5, 6]. Innovations in all areas of battery research are therefore eagerly anticipated to improve chemistry, structure, formation and production processes of battery cells. [7–11]

Viable alternatives to intercalation electrodes are conversion anodes and cathodes that undergo a chemical transformation during the insertion and extraction of lithium ions (Li^+s). Depending on the electron transfer reaction, more than one electron per mol can be transferred when oxidizing or reducing the active species, which has the potential to deliver higher specific capacities and energy densities compared to intercalation electrodes [12]. Using lithium (Li) conversion anodes ca. 10 times higher specific capacities, compared to a graphite anode, can be achieved. Combination with conversion cathodes, such as sulfur, significantly improves the energy density and specific capacity of the rechargeable battery system (Fig. 1.1) [13].

[1] Parts of this chapter have been published in Schön, Hintz, and Krewer [1]

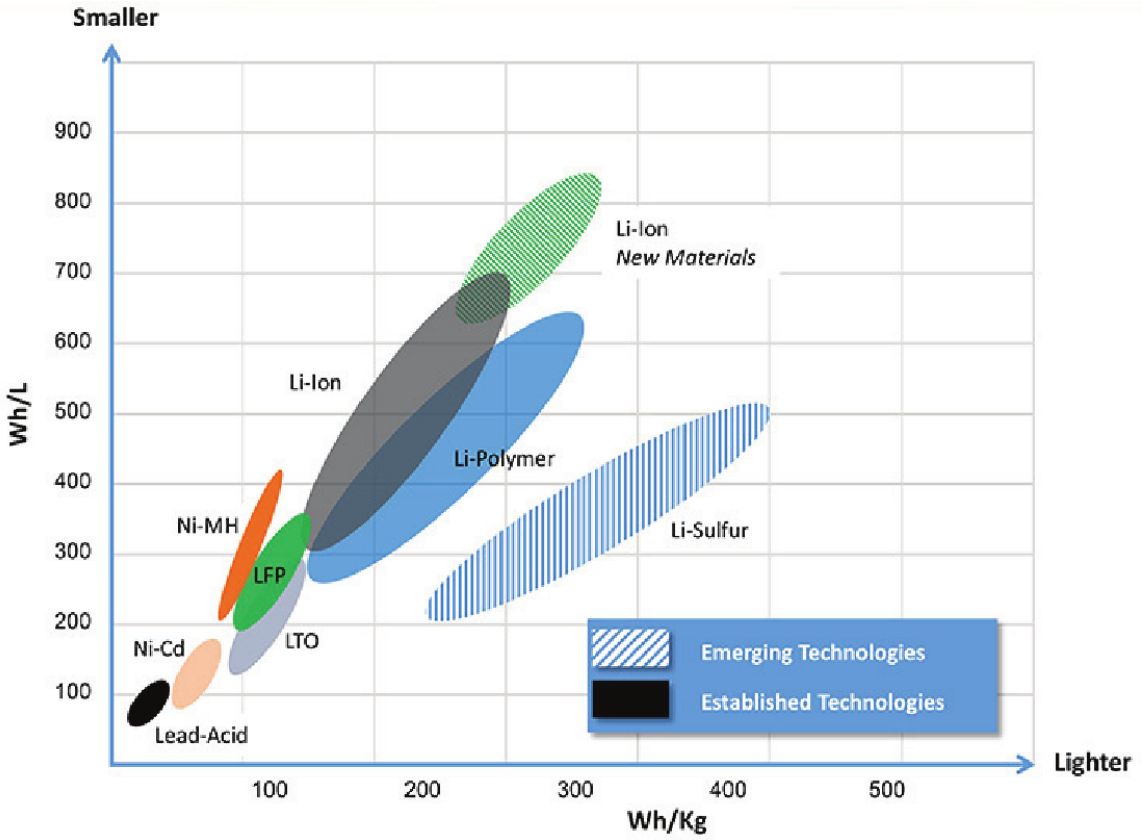

Figure 1.1: Progress of the battery technology in terms of volumetric and gravimetric energy density the on cell level. [15]

Although certain types of conversion electrodes are already commercialized, being on the market even before the release of intercalation electrodes, inherent problems such as poor reversibility of electrode reactions, large volume fluctuations causing severe safety concerns and short lifespan prevent their practical application [12, 14].

Battery cell development involves many research areas that have made great progress in recent years. Computational simulations and advanced characterization technologies provide deeper understanding that can be used by innovative production processes including, e.g. nanotechnology, to manufacture optimized electrodes.

1.2 Lithium-sulfur batteries

Sulfur is an abundant and therefore cheap, non-toxic material that represents a safer, cost-effective and environmentally friendly alternative to Li-ion cathodes. In particular, the usage of heavy metals can be significantly reduced [16, 17]. Cost reduction of cathodes is assumed to be $\sim \$100\,\mathrm{kW^{-1}\,h^{-1}}$ [18]. In addition, lithium-sulfur batterys (LSBs) are not subject to aging processes when stored at 0 % state of charge (SoC) enabling a simple handling of the cells [18].

In applications where weight is a critical parameter, LSBs can be favorable. The LSB has been applied to power the Zephyr high-altitude pseudosatellite aircraft, which flew for over 14 days [19]. The utilized LSBs was supplied by Sion Power Company and had a high usable energy of $350\,\mathrm{W\,h\,kg_{pack}^{-1}}$ after minimization of the total pack weight. Besides classical battery configuration, lithium polysulfide (Li_2S_n) systems show promising characteristics for application in stationary flow batteries. Here, efforts must be made to increase the effective concentration of sulfur in the catholyte and minimize the conductive current collector mass [20]. Furthermore, because of abundant resources, low costs, and high biocompatibility, LSBs are attractive for reliable bulk energy storage applications [20–25].

The most stable allotrope of sulfur is S_8 [26]. S_8 exhibits a high capacity of $1672\,\mathrm{mA\,h\,g_{S_8}^{-1}}$. Typically, LSBs are fabricated with S_8 dispersed in a conductive matrix of carbon materials to form the cathode [27–32]. Metallic Li serves as anode material, because it combines high theoretical specific capacity of $3860\,\mathrm{mA\,h\,g_{Li}^{-1}}$ and a low standard electrode potential of $-3.04\,\mathrm{V}$ relative to the standard hydrogen electrode. This system exhibits relatively high output voltages 2.5 V to 1.7 V resulting in a theoretical energy density of up to $2600\,\mathrm{W\,h\,kg_{cell}^{-1}}$. [33] In practical terms, it is assumed that the accessible capacity of LSBs could reach $\sim 600\,\mathrm{W\,h\,kg^{-1}}$, about 25 % of the theoretical value [33]. Ether-based electrolytes, e.g. a combination of 1,3-Dioxolan (DOL) and 1,2-dimethoxyethane (DME) as solvents, are used, because carbonate-based electrolytes utilized for LIBs immediately react irreversibly with polysulfides. In ether-based electrolytes, polysulfide intermediates are dissolving which leads to a multi-step reduction of S_8 [34–37]. Variations of the system are possible by changing the active material to either short-chain sulfur [31, 32, 38–42], lithium sulfides [43–45], or catholyte [46–50]. Furthermore, the carbon material in the conductive matrix may be substituted by conductive polymers [51] or conductive

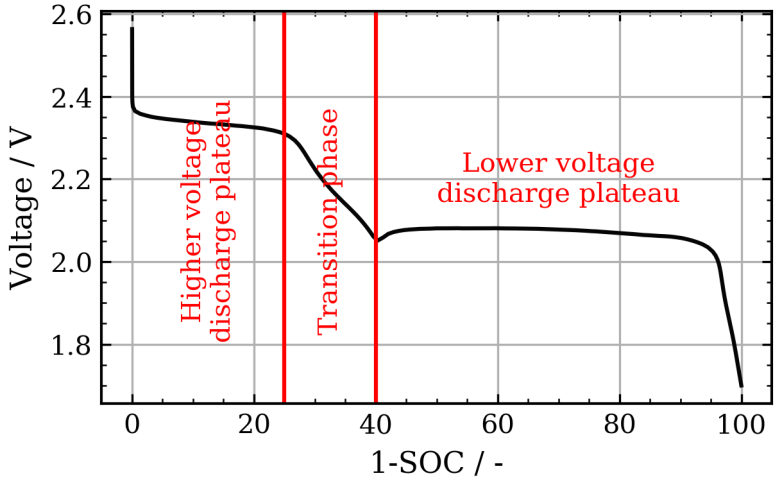

Figure 1.2: Typical discharge curve of a LSB showing the two characteristic discharge plateaus and the transition phase. [53]

metal oxides [52]. Finally, alternative anode materials like Li compounds (C-Li, Si-Li etc.) or Li free anodes, such as carbon-containing or silicon-containing materials, can be introduced. A suitable electrolyte has to be chosen according to the electrode material.

Galvanostatic discharge of LSBs exhibit two characteristic voltage plateaus, which can be seen in Fig. 1.2. The higher voltage discharge plateau with a theoretical specific capacity of $418\,\mathrm{mA\,h\,g_{S_8}^{-1}}$ and the lower voltage discharge plateau with a theoretical specific capacity of $1254\,\mathrm{mA\,h\,g_{S_8}^{-1}}$.

Limitations can be seen in Fig. 1.3 and are listed in the following: (i) Both S_8 and lithium sulfide (Li_2S) are insulating for electrons and Li^+ transport, hindering educt material to reach the electrode/electrolyte interface, which is limiting the reaction rate and results in low utilization of electroactive material. Therefore, the theoretical capacity of the higher voltage discharge plateau is hardly achievable. Reduction of S_8 to long-chain polysulfide requires good electrical contact with conductive additives and a homogeneous dispersion of S_8. In practical conditions, this involves the incorporation of S_8 in a conductive matrix [55–58], resulting in decreased theoretical specific capacity. In addition, the lower voltage discharge plateau exhibits a high polarization due to Li_2S precipitation, limiting kinetics of electron transfer reactions [59, 60], which results

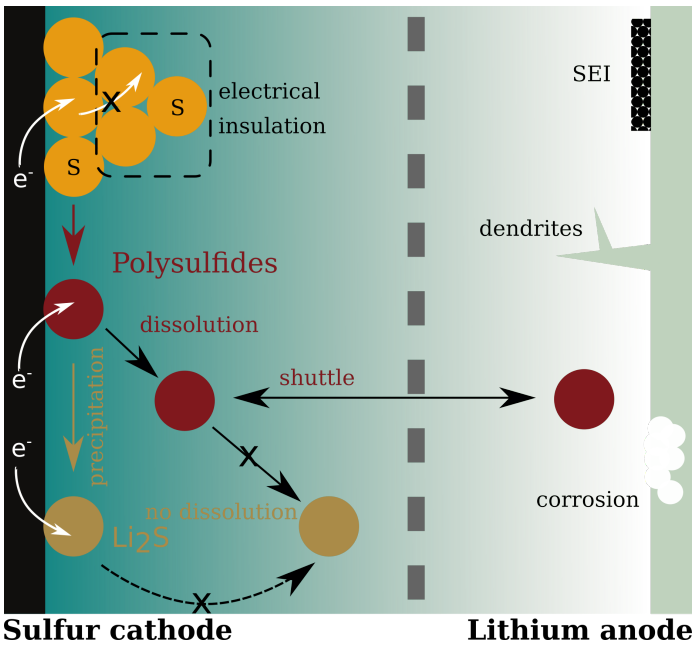

Figure 1.3: Schematic of internal processes limiting a typical LSB. Reproduced from Zhang et al. [54].

in a further decrease in practical energy density. (ii) During charging polysulfides are driven to the Li electrode by the concentration gradient. After reduction to short chain polysulfides or insoluble Li_2S the electric field causes the migration back to the positive electrode. The short chain polysulfides oxidize and repeat the circle, resulting in the shuttle mechanism and causing a low coulombic efficiency. In addition, this leads to degradation of the LSB, because of irreversible loss of active material. [20, 61] (iii) The steady dissolution and precipitation of electroactive species upon cycling leads to a unfavorable, inhomogeneous distribution of S_8 within the cathode, which increases the impedance and passivates the electrode. [20] (iv) The 80 % volume expansion going from S_8 to Li_2S upon lithiation leads to mechanical stress detaching parts of the conductive matrix and S_8, resulting in permanent capacity fade. (v) A major problem is the formation of Li dendrites induced by a Li^+ concentration gradient in the electrolyte close to the anode and an inhomogeneous distribution of current density on the surface, that lead to inhomogeneous lithium metal crystal nucleation and growth [62]. Dendrites potentially cause short circuits that are a safety concern [63]. (vi) Metallic Li is highly reactive and forms the solid electrolyte interface (SEI) when getting in contact with organic electrolytes. The SEI is unstable because

of the repeated Li plating and stripping upon cycling. This results in continuous irreversible consumption of active Li [64, 65].

The C-rate performance of LSBs is generally limited and galvanostatic discharge above 1 C suffers from dramatic reduction in specific capacity [18]. To overcome this issue modified cathode structures and material compositions are applied, allowing for rapid mass transfer of educt material from bulk to the active electrode surface [66, 67], as well as low density electrolytes designed for fast Li^+ diffusion [68].

Electrochemically, the LSB discharge is based on S_8 electron transfer reaction with Li^+s transferring 16 e^- per mol_{S_8} to the final product Li_2S as given in Eq. 1.1 and Eq. 1.2.

$$16\,Li \longrightarrow 16\,Li^+ + 16\,e^- \tag{1.1}$$

$$S_8 + 16\,e^- + 16\,Li^+ \longrightarrow 8\,Li_2S \tag{1.2}$$

However, there is no direct path from S_8 to Li_2S. During galvanostatic discharge, solid S_8 dissolves at the cathode into the electrolyte, forming liquid S_8. Liquid S_8 is then reduced by electron transfer reactions to form intermediate polysulfide species, which are soluble in the liquid electrolyte. A parallel oxidation of Li metal to Li^+ at the anode is balancing the electric charge. The polysulfides diffuse from the cathode to the electrolyte/separator, according to the concentration gradient. Generally, the length of the polysulfide chain is decreasing with decreasing SoC, which influences polysulfide solubility, their mobility and the viscosity of the electrolyte. At the end of discharge, S_8 is fully reduced at the cathode and the anode is completely stripped of Li metal, reaching the final product Li_2S. [68]

It is well-known that the S_8 chemistry depends heavily on the chemical environment, which predominantly means the electrolyte [69–75]. The exact mechanism is complex and still under debate, the next section discusses the current state of science regarding the mechanism.

1.3 Lithium-sulfur reaction mechanism

Understanding the fundamental kinetic of electron transfer and chemical reactions or electrode degradation of LSBs is an integral part of a knowledge driven optimization of LSBs to improve performance for commercial applications [76]. LSB limitations are

closely linked to the reaction kinetics. High utilization of S_8 is the most crucial factor for achieving a high energy density, formation of polysulfide regulates the "shuttle mechanism" and appearance of Li_2S electrically insulates the electrode.

Various electron transfer and chemical disproportionation reactions are possible to reach the final reduction product of Li_2S. In general, the electron transfer reactions can be expressed as:

$$S_n^{2-} + 2\,e^- \rightleftharpoons S_m^{2-} + S_{n-m}^{2-} \tag{1.3}$$

$$S_n^{2-} + 2\,(n/m - 1\,)e^- \rightleftharpoons (n/m)S_m^{2-} \tag{1.4}$$

where $n \in [2,8]$ and $m \,|\, m \in [1,7] \wedge (m < n) \wedge (m \geq 1)$. The chemical disproportionation reactions between polysulfides follow the general reaction scheme:

$$S_n^{2-} + S_m^{2-} \rightleftharpoons S_{n+x}^{2-} + S_{m-x}^{2-} \tag{1.5}$$

where $n \in [2,7]$, $m \,|\, (m \in [2,7]) \wedge (m \leq n)$ and $x \,|\, x \in [1,3] \wedge (x \leq n-8) \wedge (x \leq 1-m)$. Reactions of polysulfides with S_8 are also likely as shown by Berger et al. [77] and could follow the reaction scheme:

$$n/_8\,S_8 + S_m^{2-} \rightleftharpoons S_{n+m}^{2-} \tag{1.6}$$

where $m \in [1,7]$ and $n \,|\, n \in [1,7] \wedge (n \leq 8 - m)$. Additionally, these reactions are competing with chemical reactions described in Eq. (1.7), that can occur between polysulfides and Li of the anode.

$$(n-1\,)Li_2S_n + 2\,Li_{(s)} \longrightarrow nLi_2S_{n-1} \tag{1.7}$$

where $n \in [2,8]$. Polysulfides with short chain lengths ($n = 2-5$) can be formed stably in solution. The Gibbs free-energy of the polysulfide anions is so close that these anions are co-existing in the solution [78]. Eq. (1.3) to (1.7) yield a wide range of theoretically possible reaction mechanisms and intermediates, which are subject of discussion in this work.

The sulfur reduction mechanism and its kinetics have been under investigation

by various research groups using a large number of electrochemical methods like impedance spectroscopy [79, 80], CV [35, 81] and rotating disk electrode set-ups [35]. In addition, a large number of chemical analysis methods were used to address the change of the LSB system during discharge and charge and to identify changes of the electrode surface or reacting species. These include ex-situ investigations like high performance liquid chromatography (HPLC) with a ultraviolet (UV) or mass spectrometry (MS) [36, 82] and in-situ measurements using UV-visible absorption spectroscopy [83], X-ray absorption near-edge spectroscopy [84, 85], X-ray diffraction [86–89], X-ray transmission microscopy [87], nuclear magnetic resonance and raman spectroscopy [89–93].

Experimental findings representing the electron transfer reactions of the higher Voltage discharge plateau are shown in Tab. 1.1. Reduction of S_8 to octasulfide (S_8^{2-}) is the first electron transfer step, which is agreed between all research groups [35, 36, 82, 94, 95]. All polysulfides have been identified, while discharge is still at the higher voltage discharge plateau. This is interpreted differently. Electron transfer reactions of S_8 have been proposed [82], as well as disproportionation reactions [35, 36]. The proposed disproportionation reactions can be seen in Tab. 1.4. Circular routes have been introduced to produce more S_8 [35, 36]. Finally, two consecutive steps to form tetrasulfide (S_4^{2-}) have been proposed [35]. Electron transfer reactions of the higher voltage discharge plateau are summarized in Tab. 1.1.

The transition phase between 2.1 V to 2.3 V is characterized by electron transfer reactions of polysulfides with longer chain length (S_x^{2-}, x=8-4), see Tab. 1.2 [36, 82, 94, 95]. Disproportionation reaction products lead to the formation of sulfide (S^{2-}). Therefore, precipitation of Li_2S begins.

At the lower voltage discharge plateau, electron transfer reactions of short chain polysulfides and heterogeneous electron transfer reactions have been identified. The result of these electron transfer reactions are the two most oxidized reaction products, disulfide (S_2^{2-}) and S^{2-}, as shown in Tab. 1.3.

Wild et al. [37] summarized the published experimental results and proposed a simplified discharge mechanism that results in the characteristic two plateau discharge curve. The proposed mechanism will be discussed in the following as an example of the various reaction paths.

The higher potential discharge plateau at around 2.3 V vs. Li/Li^+ occurs because of two reduction steps that consume four electrons in total. After dissolution, the

Table 1.1: Electron transfer reactions during the higher voltage discharge plateau proposed by several research groups with different analysis methods.

Plateau	Reaction	Group
>2.3 V	$S_8 + 2\,e^- \longrightarrow S_8^{2-}$	Barchasz et al. [36]
	$S_8 + 2\,e^- \longrightarrow S_8^{2-}$ $S_8 + 4\,e^- \longrightarrow S_7^{2-} + S^{2-}$ $S_8 + 4\,e^- \longrightarrow S_6^{2-} + S_2^{2-}$ $S_8 + 4\,e^- \longrightarrow S_5^{2-} + S_3^{2-}$ $S_8 + 4\,e^- \longrightarrow S_4^{2-} + S_4^{2-}$	Kawase et al. [82]
	$S_8 + 2\,e^- \longrightarrow S_8^{2-}$ $S_8^{2-} + 2\,e^- \longrightarrow S_8^{4-}$	Lu, He, and Gasteiger [35]
	$S_8 + n\,Li + n\,e^- \longrightarrow Li_nS_8 (n = 1, 2)$	Zhu et al. [94]
	$S_8 + 2\,e^- \longrightarrow S_8^{2-}$	Wang et al. [95]

Table 1.2: Electron transfer reactions during the transition between the two discharge plateaus proposed by several research groups with different analysis methods.

Plateau	Reaction	Group
2.3 V to 2.1 V	$2\,S_6^{2-} + 2\,e^- \longrightarrow 3\,S_4^{2-}$	Barchasz et al. [36]
	$S_8^{2-} + 2\,e^- \longrightarrow S_6^{2-} + S_2^{2-}$ $S_8^{2-} + 2\,e^- \longrightarrow S_5^{2-} + S_3^{2-}$ $S_8^{2-} + 2\,e^- \longrightarrow 2\,S_4^{2-}$ $S_7^{2-} + 2\,e^- \longrightarrow S_4^{2-} + S_3^{2-}$ $S_6^{2-} + 2\,e^- \longrightarrow S_3^{2-} + S_3^{2-}$ $S_5^{2-} + 2\,e^- \longrightarrow S_3^{2-} + S_2^{2-}$ $S_4^{2-} + 2\,e^- \longrightarrow S_2^{2-} + S_2^{2-}$	Kawase et al. [82]
	$S_8^{2-} + 2\,e^- \longrightarrow 2\,S_4^{2-}$ $S_6^{2-}(2\,S_3^{*-}) + 2\,e^- \longrightarrow 2\,S_3^{2-}$	Wang et al. [95]
	$Li_2S_8 + 2\,Li^+ + 2\,e^- \longrightarrow 2\,Li_2S_4$	Zhu et al. [94]

Table 1.3: Electron transfer reactions during the lower voltage discharge plateau proposed by several research groups with different analysis methods.

Plateau	Reaction	Group
≤2.1 V	$2\,S_4^{2-} + 2\,e^- \longrightarrow 4\,S^{2-}$ $2\,S_3^{2-} + 2\,e^- \longrightarrow 3\,S_2^{2-}$ $S_2^{2-} + 2\,e^- \longrightarrow 2\,S^{2-}$ or $S_4^{2-} + 2\,e^- \longrightarrow 2\,S_2^{2-}$ $S_2^{2-} + 2\,e^- \longrightarrow 2\,S^{2-}$	Barchasz et al. [36]
	$S_3^{2-} + 2\,e^- \longrightarrow S_2^{2-} + S^{2-}$ $S_2^{2-} + 2\,e^- \longrightarrow 2\,S^{2-}$	Kawase et al. [82]
	$S_4^{2-} + 2\,e^- \longrightarrow 2\,S_2^{2-}$	Lu, He, and Gasteiger [35]
	$S_3^{*-} + e^- \longrightarrow S_3^{2-}$	Lowe, Gao, and Abruña [86]
	$S_4^{2-} + 2\,e^- + 4\,Li^+ \longrightarrow 2\,Li_2S_2$ $Li_2S_2 + 2\,e^- + 2\,Li^+ \longrightarrow 2\,Li_2S$	Wang et al. [95]
	$Li_2S_4 + 2\,Li^+ + 2\,e^- \longrightarrow 2\,Li_2S_2$ $Li_2S_2 + 2\,Li^+ + 2\,e^- \longrightarrow 2\,Li_2S$	Zhu et al. [94]

Table 1.4: Chemical reactions proposed by several research groups with different analysis methods.

Reaction	Group
$S_8^{2-} \rightleftharpoons S_6^{2-} + \frac{1}{4}\,S_8$ $S_8^{2-} \rightleftharpoons S_5^{2-} + \frac{3}{8}\,S_8$ $S_6^{2-} \rightleftharpoons 2\,S_3^{*-}$ $S_6^{2-} \longrightarrow S_5^{2-} + S_7^{2-}$ $S_4^{2-} \longrightarrow S_5^{2-} + S_3^{2-}$ $S_2^{2-} + S_4^{2-} \longrightarrow 2\,S_3^{2-}$	Barchasz et al. [36]
$S_8^{2-} \rightleftharpoons S_6^{2-} + \frac{1}{4}\,S_8$ $S_6^{2-} \rightleftharpoons 2\,S_3^{*-}$ $S_4^{2-} \rightleftharpoons \frac{3}{5}\,S_6^{2-}(S_3^{*-}) + \frac{2}{5}\,S^{2-}$	Wang et al. [95]
$2\,Li_2S_8 \longrightarrow 2\,Li_2S_4 + S_8$ $3\,Li_2S_2 \longrightarrow Li_2S_4 + 2\,Li_2$	Zhu et al. [94]

first electron transfer step reduces S_8 according to Eq. (1.8):

$$S_8 + 2\,e^- + 2\,Li^+ \rightleftharpoons Li_2S_8 \tag{1.8}$$

The second reduction step takes place either as in Eq. (1.9) or Eq. (1.10):

$$Li_2S_8 + 2\,e^- + 2\,Li^+ \rightleftharpoons Li_2S_6 + Li_2S_2 \tag{1.9}$$

$$Li_2S_8 + 2\,e^- + 2\,Li^+ \rightleftharpoons 2\,Li_2S_4 \tag{1.10}$$

The main part of the electric charge is released at the lower voltage discharge plateau with around 2.0 V. Here, reaction Eq. (1.12) is assumed to proceed via a radical that is generated in the chemical reaction according to Eq. (1.11).

$$Li_2S_6 \rightleftharpoons 2\,LiS_3\cdot \tag{1.11}$$

$$LiS_3\cdot + e^- + Li^+ \longrightarrow Li_2S_3 \tag{1.12}$$

The product Li_2S_3 may react with the reactant of Eq. (1.11) by association and precipitation according:

$$Li_2S_3 + Li_2S_4 \rightleftharpoons Li_2S_6 + Li_2S_{(s)} \tag{1.13}$$

The reviewed simulation studies are based on one of the four options: (i) a pure mathematical model [99], (ii) an equivalent circuit model [79, 80, 100], (iii) the physicochemical model of Mikhaylik and Akridge [96] (Fig. 1.4 green arrows) [61, 101] , and (iv) the physicochemical model of Kumaresan, Mikhaylik, and White [97] (Fig. 1.4 black arrows) [102–104].

Mikhaylik and Akridge [96] implement a two step reaction mechanism:

$$S_8 + 4\,e^- \rightleftharpoons 2\,S_4^{2-}$$

$$S_4^{2-} + 4\,e^- \rightleftharpoons 2\,S^{2-} + S_2^{2-}$$

The mechanism has been extended by implementing chemical precipitation of Li_2S

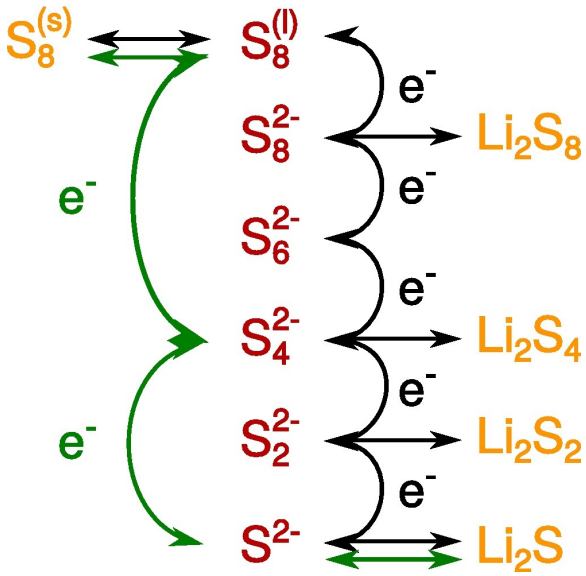

Figure 1.4: Sulfur reaction mechanisms used in simulation studies. The green arrows indicate the mechanism developed by Mikhaylik and Akridge [96]. The red arrows show the mechanism first implemented by Kumaresan, Mikhaylik, and White [97]. [98]

[61, 101] and S_8 [61].

$$S_{8(l)} \rightleftharpoons S_{8(s)} \tag{1.14}$$

$$S^{2-} + 2\,Li^{+} \rightleftharpoons Li_2S_{(s)} \tag{1.15}$$

Kumaresan, Mikhaylik, and White [97] have considered consecutive electron transfer reactions, with reduction of S_8 and S_8^{2-} at a high potential and the remaining reactions

at a lower potential:

$$\begin{aligned}
\frac{1}{2}\,S_8 + e^- &\rightleftharpoons \frac{1}{2}\,S_8^{2-} \\
\frac{3}{2}\,S_8^{2-} + e^- &\rightleftharpoons 2\,S_6^{2-} \\
S_6^{2-} + e^- &\rightleftharpoons \frac{3}{2}\,S_4^{2-} \\
\frac{1}{2}\,S_4^{2-} + e^- &\rightleftharpoons S_2^{2-} \\
\frac{1}{2}\,S_2^{2-} + e^- &\rightleftharpoons S^{2-} \\
S_{8(l)} &\rightleftharpoons S_{8(s)} \\
S_x^{2-} + 2\,Li^+ &\rightleftharpoons Li_2S_{x(s)}, \quad x = 8, 4, 2, 1
\end{aligned}$$

The mechanism has been extended by implementing a disproportionation reaction [102]:

$$3\,S_2^{2-} \rightleftharpoons S_4^{2-} + 2\,S^{2-}, \tag{1.16}$$

and various precipitation reactions [98]:

$$S_8^{2-} + 2\,Li^+ \rightleftharpoons Li_2S_8 \tag{1.17}$$

$$S_4^{2-} + 2\,Li^+ \rightleftharpoons Li_2S_4 \tag{1.18}$$

$$S_2^{2-} + 2\,Li^+ \rightleftharpoons Li_2S_2 \tag{1.19}$$

$$S^{2-} + 2\,Li^+ \rightleftharpoons Li_2S \tag{1.20}$$

On the one hand, experimental findings are not consistent and more work has to be done in order to find more evidence for the mechanistic steps. On the other hand, modeling approaches are not based on a physically motivated mechanism. Experimental findings that revealed a more complex reaction mechanisms are not incorporated, so far. In the next chapter experimental findings regarding the kinetics of the reaction mechanism are introduced.

1.4 Electrochemical and spectroscopic methods for kinetic analysis

Kinetic analysis is usually done by combining microscopy, spectroscopy or macroscopic testing with electrochemical analysis methods in order to obtain comprehensive results and maximize knowledge gained especially from in-situ and in-operando characterization experiments [76].

However, it extremely difficult to isolate individual polysulfide species and their reaction behavior in experiments, so the elucidation of mechanistic steps and their kinetic is problematic [105]. Furthermore, the kinetic is likely to depend on the properties of specific cell components. It can be significantly influenced by the physical and chemical properties of the electrolyte including reactivity to Li, dielectric constant, viscosity or polysulfide affinity and also the structure and chemical characteristics of the cathode [37, 105]. However, important information have already been presented in various studies summarized in the following.

Among the most commonly used electrochemical analysis methods are CV [35, 70, 81, 106, 107] and galvanostatic discharge, which have been widely applied in investigating the kinetic behavior of LSBs.

CV results for elemental S_8 cathodes exhibit two cathodic peaks that appear between 2.2 V to 2.4 V and 1.9 V to 2.1 V, respectively, in ether-based electrolytes. These originate from S_8 reduction to polysulfides and further reduction reactions. The appearing anodic peaks correspond to a consecutive oxidation of produced polysulfides that have been produced earlier during reduction. [108]

The difference in peak potentials of the electron transfer reactions between the examined systems, see Fig. 1.5, are strongly affected by the used electrolyte and its ability to solvate primary formed polysulfides. Thus, the used electrolyte significantly influence the reaction kinetic [35, 81]. In low dielectric solvents the two reduction steps are much less separated in potential compared to high dielectric solvents and moreover the first oxidation peak nearly disappears, because of overlapping potential ranges. This effect leads to an additional peak in dimethyl sulfoxide (DMSO)-based solvent at -1.2 V vs Ag/AgCl attributed to S_4^{2-} reduction compared to DOL/DME based solvent. [35]

Rotating ring disk electrode (RRDE) experiments combine CV with forced

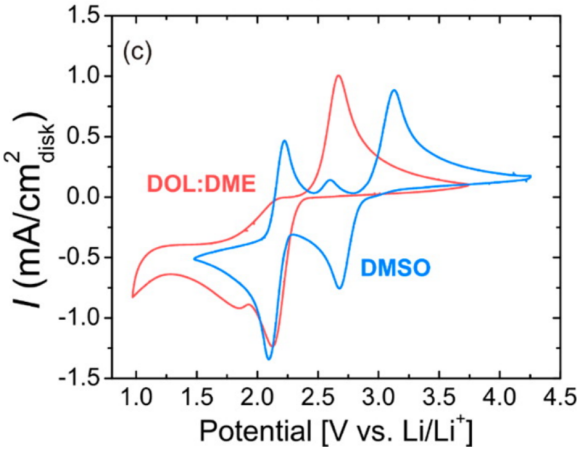

Figure 1.5: CVGs indicating the mechanism change between the two electrolytes DOL/DME and DMSO. [35]

convection by varying the rotation speed of the electrode. This allows for a calculation of reaction rates and therefore to examine the reaction kinetics of S_8 and polysulfides. Lu, He, and Gasteiger [35] calculated the number of transferred electrons per S_8 during reduction by applying the Koutecký–Levich equation [109]. S_8 and polysulfide diffusion coefficients have been determined in potential step experiments using the RRDE. The two evaluated electrolytes have been high dielectric DMSO and low dielectric DOL/DME. They conclude, that only 25 % to 34 % of total reduction capacity are contributed by electron transfer steps, corresponding to four electrons transferred per S_8 in DMSO and 5.4 electrons per S_8 in DOL/DME, respectively. They propose multiple chemical polysulfide recombination and dissociation to account for the conversion of S_8 to Li_2S. In addition, low dielectric solvents tolerate higher discharge rates, because electron transfer and disproportionation reactions are faster. [35]

However, unraveling the reaction kinetics in detail only using CV is impossible because of its limitation to the current signal. Chemical reactions such as disproportionation of polysulfides are not easily observed. Mechanism insights are further limited when electron transfer reactions occur at the same potential, which make them difficult to be separated or by reactions that occur faster or slower than testing time and are therefore not detected. Furthermore, experiments are conducted with fully dissolved species, which excludes cathode structure effects and quantitative analysis is difficult.

In galvanostatic discharge experiments the voltage response can reveal information about the electron transfer reactions based on the plateaus in the voltage capacity curves. In addition to the overall capacity, the capacity ratio between the two main plateaus and their rate dependency can be analyzed. The LSB plateau potentials during charge and discharge are influenced by the used electrolyte. It was found that the measured electrode potential is unequal to the Nernst potential and therefore could not only depend on species concentration. The gap can be assigned to solvation/complexation energies contributing to the Gibbs energy. High dielectric electrolytes resulted in higher open circuit voltages and lower plateau potentials, revealing that precipitation of Li_2S starts at the end of the higher potential discharge plateau. The cell voltage decreases when Li_2S begins to precipitate, because species are removed from solution which favor the formation of additional Li_2S. [106]

In addition to electrochemical analysis, chromatography methods can be applied. One of which is HPLC, a powerful separation technique based on adsorption capacity in two phases that is widely applied in qualification as well as quantification. Dissolved polysulfides in LSBs in the electrolyte have been identified in recent work utilizing HPLC [36, 82, 107, 110–112]. Polysulfides are methylated or benzylated for instance to stabilize them for HPLC analysis. The retention time of polysulfides increases with chain length, therefore a distinct separation is possible. At 3 V, S_8, S_8^{2-} and S_4^{2-} were detected. At 1.95 V during reaction peaks for, pentasulfide (S_5^{2-}), S_4^{2-}, trisulfide (S_3^{2-}) and S_2^{2-} have been visible in the chromatogram. After reaction, no polysulfide species were detected suggesting complete conversion to lithium disulfide (Li_2S_2)/Li_2S which precipitates. Therefore, the change from elemental S_8 to long-chain polysulfides, and then to short-chain polysulfides can be clearly confirmed as the discharge reaction. [36, 82, 107, 110–112]

Diao et al. [113] observed polysulfide species at various states of charge using liquid chromatography with mass spectrometry (LC-MS) without derivatization. They found that even with electrospray mass spectrometry to reduce fragmentation of the polysulfides, the dominant species were polysulfide clusters making interpretation difficult. Using a combination of inductively coupled plasma optical emission spectrometry to determine total S_8 content in the electrolyte and LC-MS, it was concluded that, (i) the total dissolved S_8 content in the electrolyte peaked in the middle of the high potential discharge plateau plateau at potentials >2.2 V rather than at the end before the voltage decrease suggesting a non-linear mechanism, (ii) the total

S_8 content in the electrolyte is reduced throughout the lower voltage discharge plateau corresponding to the precipitation of Li_2S at the start of the lower voltage discharge plateau plateau. At the end of discharge 20 % of S_8 remains in the electrolyte, whereas at the end of charge 45 % of S_8 remains, when cycling between 1.7 V to 2.4 V. These amounts of S_8 at the end of charge and discharge did not vary significantly with cycle life despite capacity fade, thus the final concentration of S_8 in the electrolyte when in equilibrium with the polysulfides does not impact capacity fade.

Other characterization techniques give further insight into certain aspects of the LSB reaction mechanism, but are not in focus of this work. Spectroscopic techniques also promote the understanding of the electron transfer and disproportionation reactions in LSBs. Wang et al. [95] directly observed sulfur radicals by using in-situ electron paramagnetic resonance technique. Based on the results, they found that the concentration of sulfur radicals differ at different potentials, proposing that the reaction mechanism in LSBs involve chemical or electrochemical reactions associated with sulfur radicals. Another emphasized point is that multiple factors, e.g., the loading of electrode materials, the electrolyte/sulfur (E/S) ratio, and the charge rate, can greatly influence the electron transfer reaction mechanism of LSBs, which may result in different characterization results. Therefore, the characterization conditions should be taken into account when pursuing the reaction mechanism of LSBs using different in-situ or in-operando characterization techniques. [114]

The higher voltage discharge plateau shows fast reaction kinetics enabled by high solubility of long-chain polysulfide [34], whereas at the lower voltage discharge plateau the conversion solid Li_2S_2 and Li_2S shows much slower reaction kinetics [115].

It is very challenging and resource consuming to explore the reaction mechanisms its kinetics only by experimental methods. However, experimental findings can be supplemented through physicochemical modeling giving comprehensive information about the system. Therefore, both, the reaction pathway and thermodynamic and kinetic properties can be further inferred. The reaction progress with time can be visualized showing the reaction rates and concentrations of participating species at each point in time and space [116]. Modeling of LSBs is a fundamental demand within development and is vital for applications [37, 117]. For example, knowing the state of the variables and processes due to physicochemical modeling allows for capacity determination under current load or predict remaining useful life and in addition, enables to ensure safe charging and discharging, optimal utilization of batteries, fast

charging and other applications. Several modeling approaches have been made to enlighten different aspects of the LSB reaction mechanism, kinetics and transport properties. For example temperature dependency of state of charge [100], transport limitations [103], shuttle mechanism [61, 99], rate capability [79], capacity loss [61], and charge transfer limitations [80, 101] have been investigated.

1.5 Scope of this Work

Taking into account the previous studies in literature, CV and HPLC have been identified as most promising methods to investigate the reaction mechanism of sulfur. Therefore, applying a complementary set of chemical and electrochemical characterization methods, including HPLC, CV and galvanostatic discharge, benefits from deep insights into the proceeding reactions and occurring species. In combination with physicochemical simulation of CV a set of methods is applied, that cannot be found in literature, so far. The simulation results complete the analysis, yielding kinetic parameters and electrolyte concentration in course of the experiment. Implementation of physically motivated reaction mechanisms has also not been published. On the other hand, current experimental studies lack in deeper insights into the results, because of missing simulations.

Within this study, the knowledge driven development of LSB will be supported by revealing the underlying reaction kinetics of the S_8 conversion cathode. At first, CV in combination with galvanostatic discharge reveals the electron transfer and chemical reactions at different SoC. So far, CV has only be used to analyze freshly assembled electrodes. The approach of this study incorporates the production of polysulfides, which significantly changes the resulting CVGs and provides information about the potential and reversibility of the electron transfer reactions and transport properties of polysulfides. Until now, there is no systematic experimental electrochemical study, which gives an insight into the changes of the electron transfer and chemical reaction kinetics during discharge.

Second, investigation utilizing HPLC measures dissolved S_8 quantitatively and dissolved S_8 and polysulfides qualitatively in the electrolyte during the discharge processes. Because the analyzed system is identical to the CV study, the electrolyte composition can be correlated to the CVGs at different SoC. The electron transfer

reactions responsible for the current signal and the interplay of chemical reactions are further determined.

A physically motivated, physicochemical model is derived from experimental results of this study, that exploits in depth interpretation to further determine LSB processes by applying CV simulation. In contrast to previous simulation studies the implemented mechanism represents the results of latest published scientific knowledge. The reaction mechanism of the two discharge plateaus of S_8 reduction and the corresponding transport and kinetic parameters are derived. A sensitivity study reveals the importance of different processes during the experiment. Finally, galvanostatic discharge of LSBs uncovers the current dependency of transport and kinetics of the reactions during the higher and lower voltage discharge plateau.

Chapter 2

Fundamentals

2.1 Cyclic voltammetry

CV is the measurement of current response (Fig. 2.1b) of an electrode to a linearly increasing and decreasing potential, performed in a cycle (Fig. 2.1a) [118]. The CV input defines the change of potential over time by the scan rate v,

$$v = \left| \frac{\partial E}{\partial t} \right|. \tag{2.1}$$

At any time t on the forward sweep, the potential, E, is given by

$$E = E_{\mathrm{i}} - vt \tag{2.2}$$

with E_{i} the initial potential. At any time $t = t_{\mathrm{switch}}$, the potential reaches the vertex potential E_v where the sweep direction reverses. For $2t_{\mathrm{switch}} > t > t_{\mathrm{switch}}$,

$$E = E_v + v\,(t - t_{\mathrm{switch}}) \tag{2.3}$$

since

$$t_{\mathrm{switch}} = \frac{|E_{\mathrm{i}} - E_{\mathrm{v}}|}{v}. \tag{2.4}$$

It is usually implemented with a three electrode setup with all species in solution. The experiment is normally started at a potential below the formal potential of the investigated species, when the species are in a reduced state or at a potential above the formal potential of the investigated species, when the species are in an oxidized state. The formal potential, $E_{\mathrm{f},0}$, describes the measured potential of a half-cell, when the concentration of an oxidized and reduced species of an electron transfer reaction are equal and other concentrations can be neglected [109]. It incorporates

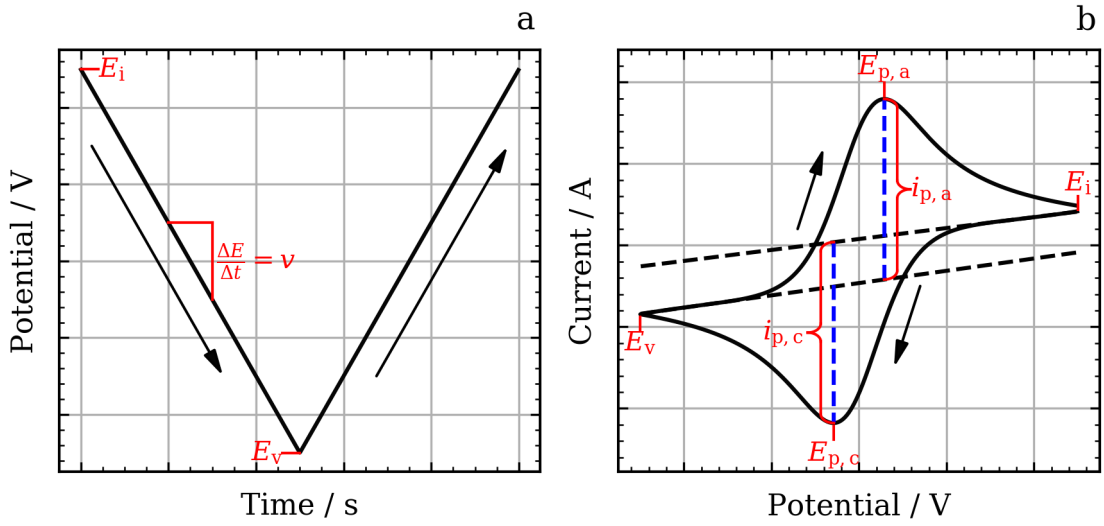

Figure 2.1: Cyclic voltammetry experiment showing the input potential (a) and the resulting current (b). The marked parameters indicate characteristic points of the cyclic voltammogram.

the standard potential, E_0, and activity coefficients, γ, as in Eq. 2.5:

$$E_{f,0} = E_0 + \frac{RT}{nF} \ln \prod_i \gamma_i^{\nu_i}. \tag{2.5}$$

In addition, all species are in chemical equilibrium and there are no concentration gradients within the examined sample at the initial state. Therefore, no electron transfer or transport processes occur in the beginning. Assuming an initial state with only oxidized species, the potential is changed starting from a high potential with a fixed scan rate to the switching potential, Fig. 2.1a. Due to the electron transfer reaction of the electroactive species present in the solution, a cathodic current peak at the potential $E_{p,c}$ is detected with the peak current density $i_{p,c}$, Fig. 2.1b. Transport to the electron/electrolyte interface is caused by diffusion due to a concentration gradient when species are reacting. When the scan rate is changed the potential increases from the switching potential to the initial value, an anodic current peak (see $E_{p,a}$) may be observed with a peak current density $i_{p,a}$. [119]

CV is an exceptional technique to evaluate the reaction mechanism of new materials or compounds and can provide information about: (i) the potential, kinetics and the

number of electrons transferred in an electron transfer reaction, (ii) the reversibility of electron transfer reactions in the investigated voltage range, (iii) transport parameters of the investigated species, (iv) the oxidation state of the electroactive species, (v) possible chemical processes associated with the electron transfer, (vi) adsorption effects, and (vii) time dependency of electrode processes, when CV is conducted at a range of different scan rates. [35, 70, 81, 106, 108, 109, 120–122]

In the following, the most basic mechanisms, E-mechanism, EE-mechanism, EC_{irr}-mechanism and EC_{rev}-mechanism, are introduced. These allow for qualitative interpretation of CVGs. However, apart from the reversible E-mechanism, there is no analytical solution to describe the kinetics. Therefore, a physicochemical model is introduced that enables for detailed analysis of CVGs. This also allows for additional insights during the experiment.

2.1.1 Experimental analysis

E-mechanism

An electron transfer reaction of the type,

$$\mathrm{A} + \mathrm{e}^- \rightleftharpoons \mathrm{B} \tag{2.6}$$

is called E-mechanism. For the simplest case of a reversible E-mechanism, the magnitude of the peak current is given by an analytical solution, the Randles–Ševčík equation [123, 124]:

$$i_\mathrm{p} = 0.446 n \mathrm{F} c \sqrt{\frac{n \mathrm{F} v D}{\mathrm{R} T}}. \tag{2.7}$$

with i_p, the peak current density, n, the number of electrons transferred per mole of reactant diffusing to the electrode surface, F, the Faraday constant, c, the concentration of analyte in solution, R, the gas constant, T, the absolute temperature, v, the scan rate and D, the diffusion coefficient.

A reversible E-mechanism (Fig. 2.2 (black)) can be identified when the following criteria are fulfilled: [118, 120, 125]: (i) The anodic ($i_\mathrm{p,a}$) and cathodic peak current density ($i_\mathrm{p,c}$), are linear functions of the square root of the scan rate $v^{0.5}$, (ii) the ratio $i_\mathrm{p,c}/i_\mathrm{p,a} = 1$ for a wide range of scan rates, (iii) the half-wave peak potential ($\Delta E_{\mathrm{p}/2}$)

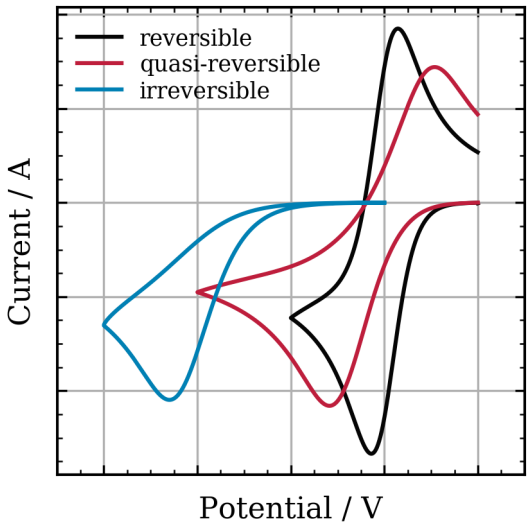

Figure 2.2: Cyclic voltammograms for a reversible (black), quasi-reversible (red) and a irreversible electron transfer reaction (blue).

does not change by altering the scan rate, (iv) the potential separation between the cathodic and anodic peak $\Delta E_\mathrm{p} = E_\mathrm{p,c} - E_\mathrm{p,a} \leq 57/n\,\mathrm{mV}$ at 25 °C.

For electrochemical systems with kinetic constraints electron transfer reaction is quasi-reversible (Fig. 2.2 (red)) or irreversible (Fig. 2.2 (blue)). Irreversibility can be identified by the following characteristics [118, 120, 125]: (i) For reduction processes the ratio between the peak currents follows $i_\mathrm{p,a}/i_\mathrm{p,c} < 1$, (ii) the half-wave peak potential ($\Delta E_{\mathrm{p}/2}$) shifts for reduction processes in negative direction, (iii) the cathodic peak current is proportional to the square root of the scan rate $v^{0.5}$ for reduction processes, (iv) the potential separation between the cathodic and anodic peak $\Delta E_\mathrm{p} = E_\mathrm{p,c} - E_\mathrm{p,a} > 57/n\,\mathrm{mV}$ at 25 °C and increases with increasing scan rate.

EE-mechanism

Transfer of multiple electrons usually takes place in separate steps. A mechanism containing two consecutive electron transfer reactions is called

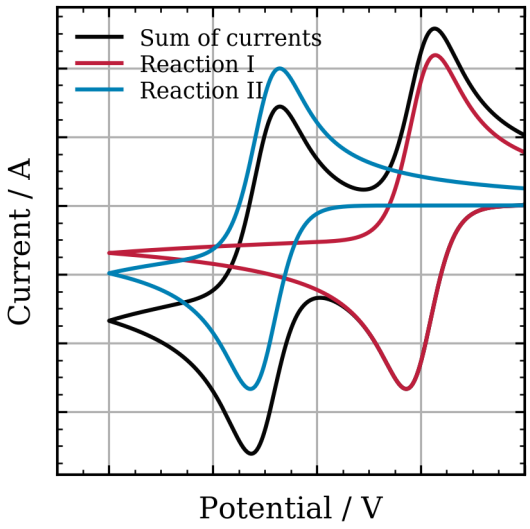

Figure 2.3: Cyclic voltammogram of an EE-mechanism. Currents of each electron transfer step, as well as the sum of these currents are given separately.

EE-mechanism (Fig. 2.3).

$$\mathrm{A} + \mathrm{e}^- \longrightarrow \mathrm{B} \qquad \text{(I)}$$

$$\mathrm{B} + \mathrm{e}^- \longrightarrow \mathrm{C} \qquad \text{(II)}$$

For each electron transfer, there is a rate relationship characterized by the reaction rate constant as well as the formal potential, Eq. (2.15). Depending on the separation between the formal potentials of the electron transfer reactions reactions, two cases have to be distinguished. Again, in the interest of simplicity only a reduction process is discussed here. [126]

Case 1: $E_{\mathrm{f},0_\mathrm{I}} > E_{\mathrm{f},0_\mathrm{II}}$: If the separation of the potentials between the electron transfer reactions is large ($E_{\mathrm{p},\mathrm{c}_\mathrm{II}} - E_{\mathrm{p},\mathrm{c}_\mathrm{I}} > 150\,\mathrm{mV}$) the resulting CVG consists of two typical, additive superimposed, one-electron transfer waves (Fig. 2.3). [126]

However, the electrode mechanism as a whole can be more complicated. In the same timescale chemical disproportionation (reaction III) may occur. The equilibrium position for the disproportionation is usually reached within the time scale of CV measurements.

$$A + e^- \rightleftharpoons B \quad \text{(I)}$$

$$B + e^- \rightleftharpoons C \quad \text{(II)}$$

$$2\,B \rightleftharpoons A + C \quad \text{(III)}$$

This causes the concentration profiles of the involved species to adapt to the equilibrium during diffusion, as indicated in Fig. 2.4. However, as long as no kinetic limitations are introduced by the chemical reaction at the electrode, the disproportionation is not directly visible in the CVG [127]. Significant changes occur only with quasi-reversible or irreversible charge transfer or with subsequent chemical follow-up reactions and these must be taken into account in interpreting experimental data. [126]

Case 2: $E_{f,0_I} = E_{f,0_{II}}$: If the difference between the formal potentials of the two reversible electron transfer reactions is less than ∼100 mV, only a single wave appears in the CVG. The resulting CVGs are consistent with the normal E-mechanism, but the current is the sum of currents of both electron transfer reactions.

EC_{irr}-mechanism

Assuming that the product (B) of a reversible electron transfer reaction (reaction I) is involved in an irreversible chemical reaction (reaction II), according to the scheme

$$A + e^- \rightleftharpoons B \quad \text{(I)}$$

$$B \longrightarrow C, \quad \text{(II)}$$

the mechanism is called EC_{irr}-mechanism.

A EC_{irr}-mechanism can be identified when the following criteria are valid [109, 118, 120]: (i) The ratio of cathodic and anodic peak currents $i_{p,c}/i_{p,a}$ (for reduction processes) is larger than 1 and it decreases by increasing the scan rate, (ii) for fast scan rates, the CVGs attain the shape typical for a unperturbed simple electron transfer reaction, (iii) the anodic current decreases when decreasing the scan rate (see Fig. 2.5), (iv) the peak currents are proportional to the $v^{0.5}$, (v) in the kinetic controlled region, the half-wave peak potential shifts in positive direction when increasing the scan rate.

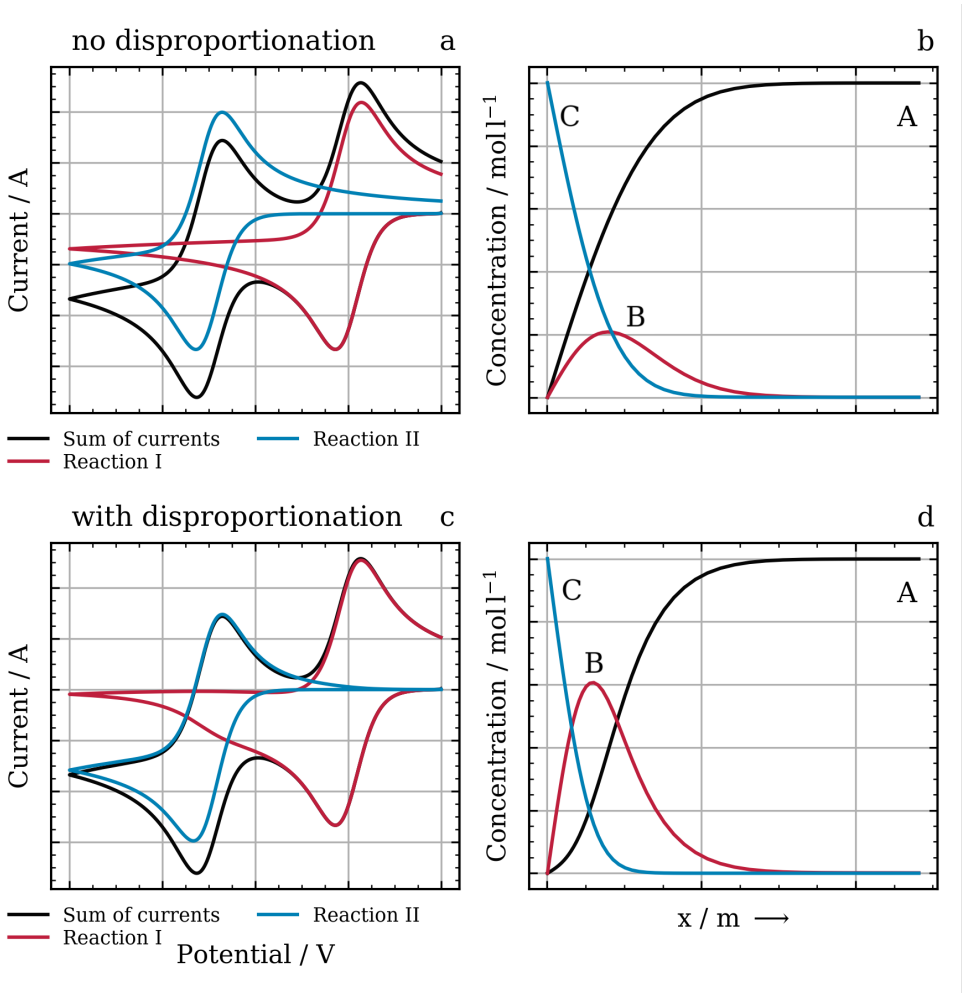

Figure 2.4: Cyclic voltammograms of an EE-mechanism with disproportionation (a) and without disproportionation (b). Individual currents of each electron transfer reaction are marked.

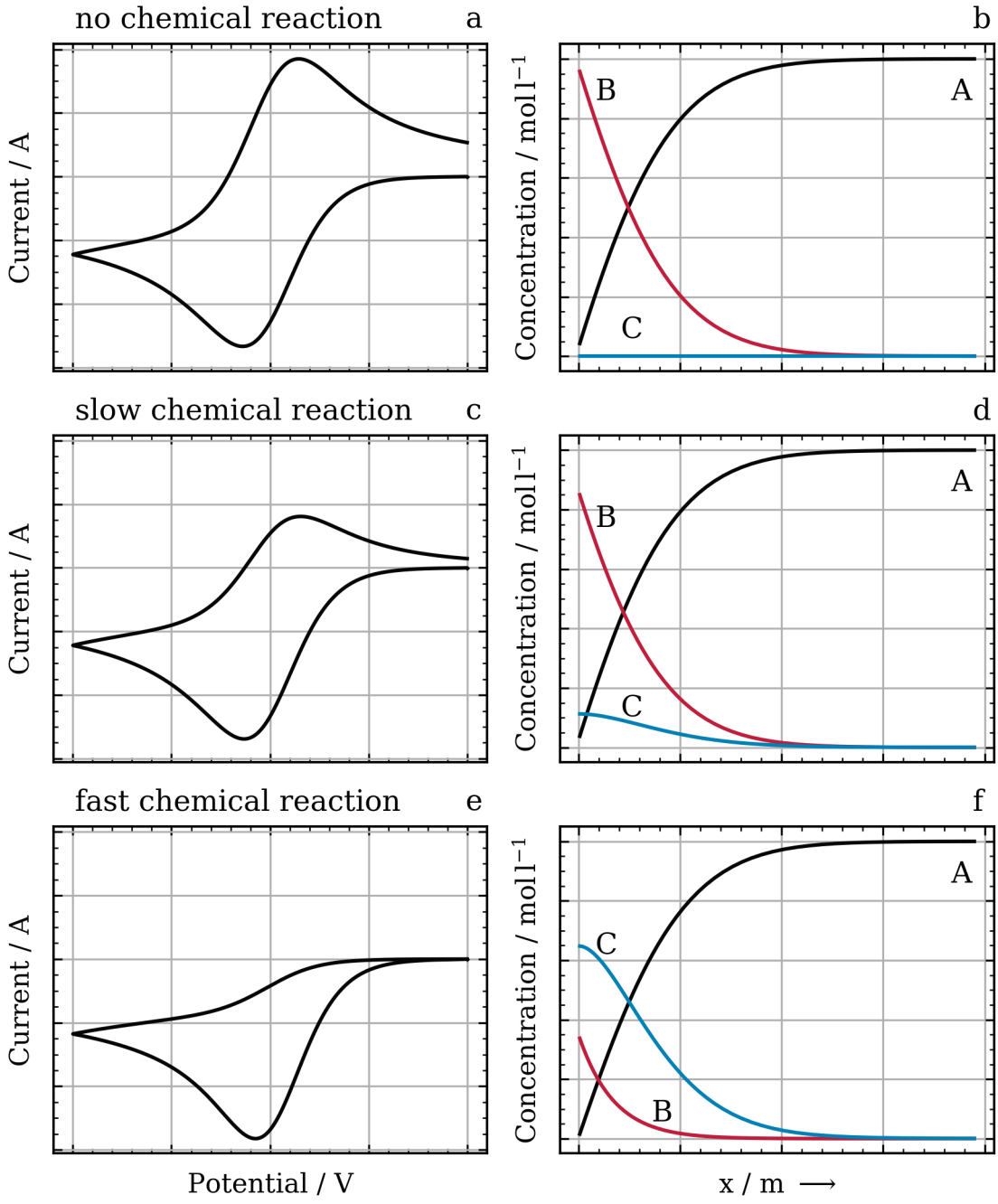

Figure 2.5: Cyclic voltammograms and accompanying concentration profiles for an EC_{irr}-mechanism.

EC_{rev}-mechanism

Assuming that the product (B) of an reversible electron transfer reaction (reaction I) is involved in additional irreversible chemical reaction (reaction II), according to the scheme

$$\mathrm{A} + \mathrm{e}^- \rightleftharpoons \mathrm{B} \qquad \text{(I)}$$

$$\mathrm{B} \rightleftharpoons \mathrm{C}, \qquad \text{(II)}$$

the mechanism is called EC_{rev}-mechanism.

For the EC_{rev}-mechanism, the following diagnostic criteria are valid for CV [109, 118, 120]. (i) The ratio of cathodic and anodic peak currents $i_{p,c}/i_{p,a}$ (for reduction processes) is larger than 1 and it decreases by decreasing the scan rate, (ii) for slow scan rates, the CVGs attain the shape typical for unperturbed simple electron transfer reactions, (iii) the anodic current decreases when increasing the scan rate, (iv) the peak currents are proportional to the $v^{0.5}$, (v) in the kinetically controlled region, the half-wave peak potential shifts in positive direction when increasing the scan rate.

2.1.2 Modeling of electrode kinetics for CV simulation

An appropriate model of CV response is required to obtain information about more complex reaction kinetics. Currently available CV simulation programs, either commercial [128–130] or open source [131–133], lack in functionality and flexibility for the desired investigations. Therefore, a new implementation is realized. CV simulation involves partial differential equation systems to be solved. Calculated concentration profiles (Fig. 2.6) of the different species are key to the current-potential-time response of the system to a given electrical perturbation. However, analytical methods provide exact solutions, applying a direct analysis of experimental parameters, only for the reversible E-mechanism. Therefore, approximation by numerical methods can be very accurate when conditions of the simulation are optimized.

Kinetic and transport equations

In general, the conservation of mass equation to describe the motion of charged chemical species in a fluid medium is described by the Nernst-Planck equation. In this

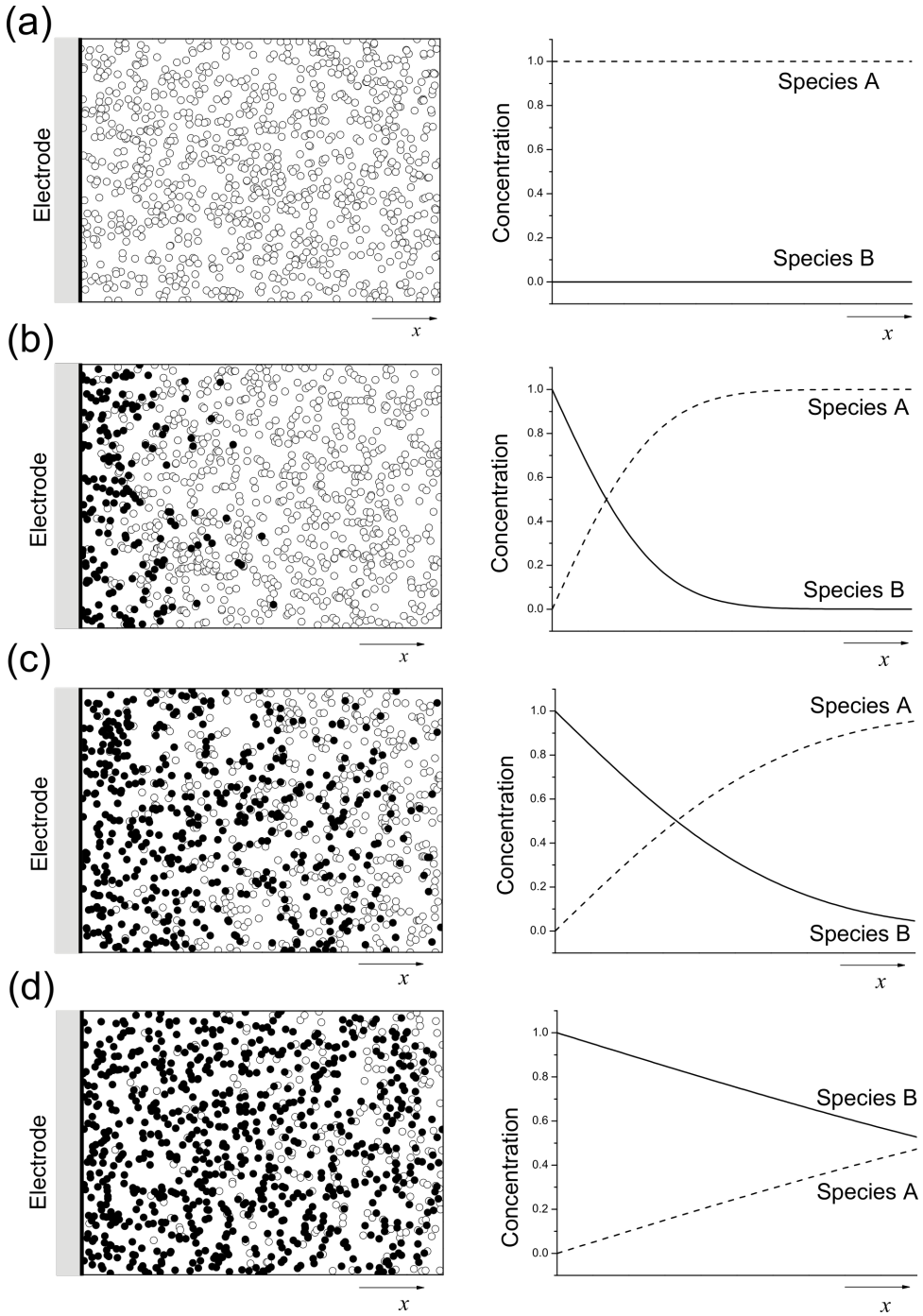

Figure 2.6: Schematic showing the distribution of particles (a) 0, (b) 1, (c) 5 and (d) 50 arbitrary time units after a potential pulse is applied to the electrode. White dots are the starting species, A, and black dots are the reduced species, B. Concentration profiles over the same space are also shown. [119]

particular case, migration due to electrostatic forces is neglected, and convection can also be neglected because the fluid has no velocity. Therefore, transport is described by diffusion. In addition to transport, a source term, S, is added to account for chemical reactions in the electrolyte. This yields the following mass balance for charged and neutral species:

$$\frac{\partial c_i}{\partial t} = -D_i \frac{\partial^2 c_i}{\partial x^2} + S_i \tag{2.8}$$

with c_i the concentration of species i, t the time, D_i the diffusion coefficient of species i. The time dependency of the source term is only due to local chemical reactions. Chemical reaction rates, r_j, follow mass action law:

$$r_j = k_{j,\mathrm{f}} \prod_{i_{\mathrm{ed}}} c_i^{\nu_{i,j}} - k_{j,\mathrm{b}} \prod_{i_{\mathrm{prod}}} c_i^{\nu_{i,j}} \tag{2.9}$$

with k_j the reaction rate constant of the forward (f) and backward (b) portion of reaction j, $\nu_{i,j}$ the stoechiometric coefficient of species i in the reaction j participating as an educt of a reaction (ed) or a product of a reaction (prod). The source term S_i of each species will consequently be the sum of all reaction rates of reactions where the species is participating:

$$S_i = \sum_{j=1}^{R} \nu_{i,j} r_j. \tag{2.10}$$

The boundary condition contains the electron transfer reactions at the electrode/electrolyte interface:

$$\left(-D_i \frac{\partial c_i}{\partial x}\right)_{x=0} = \sum_i \nu_{i,j} \frac{i_j}{n_j \mathrm{F}} \tag{2.11}$$

with i_j the partial current for electron transfer reaction j, n the number of transferred electrons and F the Faraday constant. The condition at the bulk boundary is:

$$\left(-D_i \frac{\partial c_i}{\partial x}\right)_{x=\delta} = 0. \tag{2.12}$$

Applying Faraday's law, the partial current density i_j of multiple electron transfer

reactions is calculated by:

$$i_j = -n_j \mathrm{F} r_j \Delta x \tag{2.13}$$

with n_j the number of electrons transferred Δx the distance normal to the electron surface of the first element and r_j the electrochemical reaction rate.

The reaction rate constants show an exponential dependence with the applied potential, according to the Butler-Volmer model. Only one electron can be transferred at a time to calculate the current density i [134]. Hence, for a given reaction, $n = 1$ is assumed in the exponent. Therefore, in case of electron transfer reactions the reaction rate constant of the forward reaction $k_{j,\mathrm{f}}$ and the backward reaction $k_{j,\mathrm{b}}$ are defined as:

$$\begin{aligned} k_{j,\mathrm{f}} =& k^*_{j,\mathrm{f}} \exp\left(\frac{\alpha_j \mathrm{F}}{\mathrm{R}T}\left(E - E_{\mathrm{f},0_j}\right)\right) \\ k_{j,\mathrm{b}} =& k^*_{j,\mathrm{b}} \exp\left(-\frac{(1-\alpha_j)\,\mathrm{F}}{\mathrm{R}T}\left(E - E_{\mathrm{f},0_j}\right)\right) \end{aligned} \tag{2.14}$$

with k_j the reaction rate constant, α_j the charge transfer coefficient, R the molar gas constant, T the temperature, E the potential and $E_{\mathrm{f},0_j}$ the formal potential. As a result, the reaction current i_j can be determined by:

$$\begin{aligned} i_j = -n_j \mathrm{F} \Delta x \Bigg(& k^*_{j,\mathrm{f}} \exp\left(\frac{\alpha_j \mathrm{F}}{\mathrm{R}T}\left(E - E_{\mathrm{f},0_j}\right)\right) \prod_{i_{\mathrm{ed}}} c_i^{\nu_{i,j}} \\ & - k^*_{j,\mathrm{b}} \exp\left(-\frac{(1-\alpha_j)\,\mathrm{F}}{\mathrm{R}T}\left(E - E_{\mathrm{f},0_j}\right)\right) \prod_{i_{\mathrm{prod}}} c_i^{\nu_{i,j}} \Bigg). \end{aligned} \tag{2.15}$$

The sum of partial current densities yields the total current density i:

$$i = \sum_{j=1}^{R} i_j \tag{2.16}$$

Initial concentrations

At the initial state, all involved species are in equilibrium. The concentrations can be obtained by solving an equation system of Nernst equations for each electron transfer reaction for the initial potential:

$$E_j = E_{\mathrm{f},0_j} + \frac{\mathrm{R}T}{\mathrm{F}} \ln \prod_i c_i^{\nu_{i,j}}. \tag{2.17}$$

Unequally spaced grid

An exponentially expanding grid with smaller grid size close to the electrode was used to account for larger gradients close to the electrode/electrolyte interface. Expansion is defined according to:

$$\Delta x_{\mathrm{f}_q} = \Delta x_{\mathrm{f}0} w^q \tag{2.18}$$

with Δx_f the size of modeled volume element, w the growth factor and q the volume element ($q = 1$ at the interface). w is restricted by the distance between electrolyte and bulk, L:

$$L = \sum_{q=1}^{Q} \Delta x_{\mathrm{f}q} \tag{2.19}$$

with Q the total number of volume elements.

2.2 High performance liquid chromatography

HPLC is the most commonly used liquid-chromatography method at present. Apart from the qualitative and quantitative analysis, a physical separation from both, different analytes as well as the sample matrix, is performed. Because of its separating characteristics HPLC is often used as upstream process for other detection methods like UV-Vis, MS or fluorescence spectroscopy. [135]

2.2.1 HPLC operation

The separation effect of HPLC is based on the ratio between the adsorption strength of the stationary phase and the dissolution ability of the mobile phase. An increasing retention of analytes is achieved with more interaction with the adsorbent stationary phase. [135]

The central component of an HPLC system is the separation column. The column properties are key to a successful separation, they can be adapted to the intended purpose. Adjustable properties are, the separation method (i.e. reverse phase chromatography (RP-HPLC), ion exchange chromatography), the stationary phase type (porous particles, monoliths), the morphology of the used particles (dimension, porosity), the column dimensions (length, diameter) and the macroscopic structure of the column. Typical particle diameters are between 3 µm to 10 µm. Particles smaller then 2.5 µm are used in ultra high performance liquid chromatography (UHPLC) systems [135]. The most common separation method in HPLC is RP-HPLC. In RP-HPLC the stationary phase is less polar than the mobile phase [135]. Typically, the stationary phase consists of silica gel derivatized with hydrocarbons. Mixtures of organic solvents like methanol or isopropanol and water are used as mobile phase. Unpolar analytes are subject to stronger retention by the unpolar stationary phase, while minor influence of the stationary phase is exhibited to polar species. This effect can be enhanced by increasing polarity of the mobile phase. [135]

In general, silica gel is deployed for the stationary phase in HPLC columns. Silica gel occurs in spherical or irregular formed porous particles [136]. Silanol groups of silica gel can be derivatized with functional groups like amino-, cyano-, diol-, or C_{18} groups to customize their properties. Within these alternatives, C_{18} is the most important [136]. Fig. 2.7 shows the chemical structure of a C_{18} column.

The polar surface of silica gel becomes unpolar by applying a derivatization reagent like C_{18}. Long-chain hydrocarbons are bound to the surface.

2.2.2 Detection methods and analysis

To provide qualitative or quantitative analysis, analytes and eluent are guided through a measurement cell and are analyzed by detectors. Key to detection ability are the physical and chemical properties of the analytes. These are interpreted to result in an

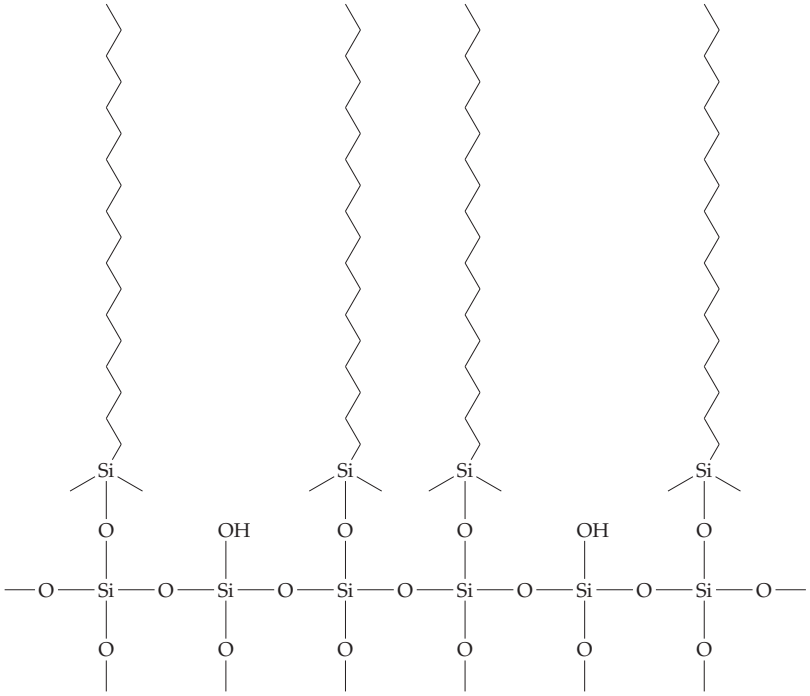

Figure 2.7: Chemical structure of a C_{18} column. [137]

electrical signal by the detector and visualized in a time-dependent chromatogram. The signal intensity is proportional to the concentration of the analyte in the measurement cell. Quantification of the concentration is enabled by integration of the measured signal to get the peak area. To quantify the analytes concentrations, they have to be calibrated.

The most commonly used detectors are UV-Vis, fluorescence, refractive index, chemiluminescence, light scattering electrochemical detectors and MS. The most important properties of detectors are sensitivity, reproducibility, stability to external disturbances, linearity of the signal in a wide concentration area, lower volume limits of analytes and a small peak widening. [135]

The concentration measurement in UV-Vis is based on the Lambert-Beer law. The Lambert-Beer law relates the attenuation of light to the properties of the material through which the light is traveling. Therefore, the amount of ultraviolet adsorption can be related to the concentration of the analytes:

$$A_\lambda = \epsilon_\lambda c \ell \tag{2.20}$$

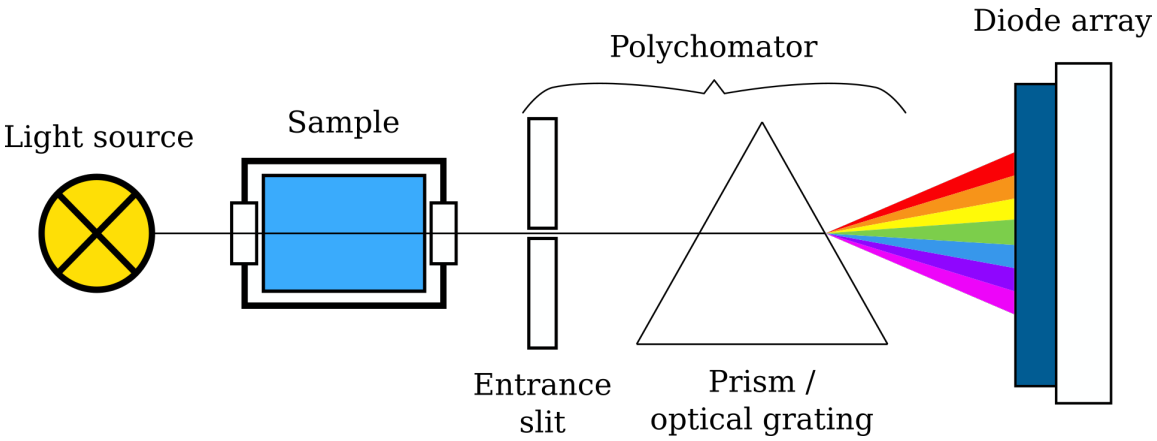

Figure 2.8: Principle of a UV-Vis diode array detector.

with A_λ the absorbance at a certain wavelength λ, ϵ_λ the absobitivity of species at wavelength λ, c the concentration of species and ℓ the optical path length. [138] The absorbance describes the reduction of light intensity through scattering and absorption [139].

$$A_\lambda = \log\left(\frac{l_0}{l_1}\right) \tag{2.21}$$

Especially analytes with double bounds and aromatic rings can be effectively analyzed by UV-Vis detectors. Detectors being able to measure the whole absorption spectrum are called diode array detector. Polychromatic light passes the measurement cell and is separated by a prism or optical grating. The separated wavelengths impinge on several photodiodes.

Another method to qualify and quantify the previously chromatographically separated analytes is MS. During MS analytes solved in the mobile phase are ionized in vacuum.

$$\mathrm{M} + \mathrm{e}^- \longrightarrow \mathrm{M}^+ + 2\,\mathrm{e}^- \tag{2.22}$$

Gaseous ions are accelerated using an electrical field and reach the detector based on their mass-to-charge ratio (m/z-ratio) with m, the molar mass and z, the ionic charge. Different methods to ionize the analytes are possible. Commonly used are atmospheric-pressure chemical ionization (APCI) and electrospray ionization (ESI). After separation using HPLC the sample enters the mass spectrometer. The sample

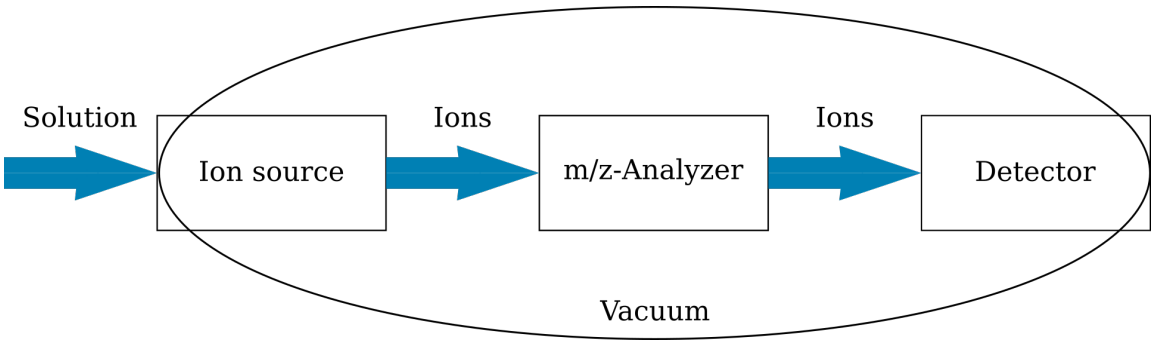

Figure 2.9: Components of a mass spectrometer.

gets atomized in a nitrogen stream to generate a spray which gets evaporated. A needle shaped electrode ionizes the vapor by applying high voltage. The ionized vapor is subject to a cone voltage which enables a separation to fragments. [140]

$$\begin{aligned} \mathrm{M}^+ &\longrightarrow \mathrm{EE}^+(\text{even ion}) + \mathrm{R}(\text{radical}) \\ &\longrightarrow \mathrm{OE}^+(\text{odd ion}) + \mathrm{N}(\text{molecule}) \end{aligned} \tag{2.23}$$

These two types of ions have different chemical properties. These primary product ion generated from the molecular ion can undergo further fragmentation, and so on. To satisfy individual demands of each analysis, the cone voltage has to be adjusted in a way to that unwanted formation of adducts as well as strong fragmentation is suppressed. The mass analyzer separates the ions according to their m/z-ratio. This is generally achieved by generation of electric or magnetic fields inside the instrument. These fields separate the ions influencing their spatial trajectories, velocity, or direction. The detector records the relative abundance of ions at each m/z-ratio. The resulting measurement called mass spectrum consists a plot of ion abundance versus its m/z-ratio. [135]

Chapter 3

Electrochemical analysis of sulfur reduction correlated to state of charge[1]

3.1 Introduction

The proposed reaction mechanism by Wild et al. described in Chapter 1.3 contains besides parallel and sequential steps also circular routes and thus would allow to explain complex relaxation behavior. To pave the way for more quantitative analysis and also simulation, a sequence of electrochemical experiments that allows to study the complex phenomena with classical electrochemical methods is presented. It is shown how the combination of CV, open circuit potential (OCP) and galvanostatic discharge reveals quantitative insights into the interplay of various electron transfer and chemical reactions and their progression over time. Based on the results a mechanism including electron transfer and chemical steps as function of state of charge is concluded. Detailed peak currents are given to facilitate quantitative modeling.

3.2 Experimental set-up

3.2.1 Preparation and cell setup

For the electrochemical investigations, a sealed three electrode set-up with 12 ml volume is used. A glassy carbon disk electrode with 5 mm in diameter (Pine Research Instrumentation, Durham, NC) is used as working electrode. Counter and reference electrode consist of Li metal (99.9 %, Merck KGaA). DOL and DME and bis(trifluoromethane)sulfonimide lithium salt (LiTFSI), Merck KGaA, are used

[1] Parts of this chapter have been published in Schön, Hintz, and Krewer [1]

without any further treatment. The electrolyte is made by mixing DOL and DME in equal volumetric parts with 1 M LiTFSI inside an argon filled glovebox. Elemental S_8 (99.9 %, Merck KGaA) is then dissolved into the electrolyte and stirred overnight to reach a 4 mM solution. Finally the cell is assembled and the electrodes are immersed into the electrolyte.

The electrochemical experiments are conducted in an argon atmosphere at room temperature of 25 °C using a Gamry Instruments Reference 3000 potentiostat. All working potentials are displayed vs. the Li reference electrode.

3.2.2 Electrochemical Measurements

CVGs are recorded in an unstirred and fresh solution with scan rates of $15\,\mathrm{mV\,s^{-1}}$, $25\,\mathrm{mV\,s^{-1}}$, $50\,\mathrm{mV\,s^{-1}}$, $100\,\mathrm{mV\,s^{-1}}$ in a potential range of 3.8 V to 1 V. After running five cycles, the scan rate is changed to the subsequent. Only the second cycle for each scan rate is used for analysis.

For discharge experiments, a constant current of 70 µA ($5.69\,\mathrm{mA\,g_{sulfur}^{-1}}$, $3.56\,\mathrm{A\,m^{-2}}$) is applied. The cell is stirred with a magnetic stirrer to hinder early transport limitations.

The measurement sequence to characterize electrode state for different states of charges of the S_8 electrode is given in Fig. 3.1. Starting from the assembled cell, CVGs are recorded with a scan rate of $50\,\mathrm{mV\,s^{-1}}$ for three cycles in a potential range of 3.8 V to 1 V unstirred. Again, the second cycle is used for analysis. Following an equilibration time of 20 min at OCP the cell is discharged for one hour at 70 µA. In case that the potential of the cell remains above 0.6 V during discharge, a second longer equilibration at OCP is conducted with a duration of 40 min. After this, the measurement cycle restarts with a CV. The cycle is continued until the potential during discharge reaches 0.6 V, which is defined as the truncation condition. The whole experiment in this configuration allowed to record 19 subsequent cycles.

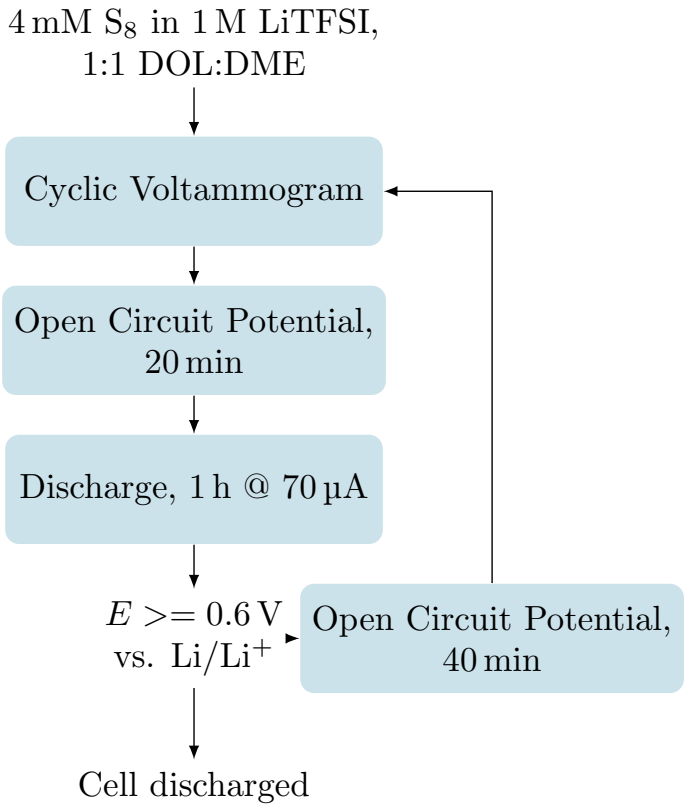

Figure 3.1: Experimental procedure for electrochemical characterization of the discharge process at the glassy carbon electrode.

3.3 Results and discussion

3.3.1 Cyclic Voltammetry

Before analyzing SoC influence, the electrode kinetics of the fresh solution is studied with CV as a reference point. As shown in Fig. 3.2a, the cathodic current at all scan rates increases at about 2.45 V. With increasing scan rates the peak potentials of the first cathodic peak decrease: 2.28 V; 2.25 V; 2.21 V and 2.21 V, whereas the absolute value of the cathodic peak current increase significantly: −157.35 µA, −238.18 µA, −337.21 µA and −428.94 µA.

For both peaks, the increase of the scan rate causes not only the expected increase in peak current but also a slight shift of the peaks to lower potentials.

In contrast to the reduction, only one peak is observed in the oxidation part of

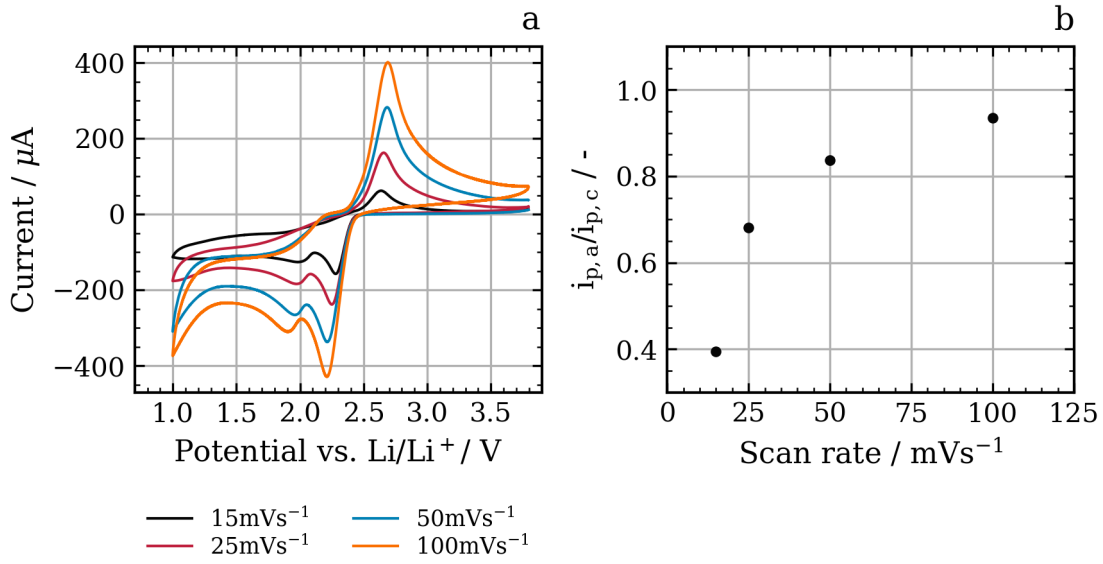

Figure 3.2: (a) Cyclic voltammograms of the glassy carbon electrode in 1:1 DOL:DME, 1 M LiTFSI electrolyte at scan rates of 15 mV s^{-1} to 100 mV s^{-1}. (b) Ratio of anodic peak current $i_{p,a}$ to cathodic peak current $i_{p,c}$ of the first peak at different scan rates.

the CV. The given peak potentials are 2.63 V, 2.66 V, 2.68 V and 2.69 V with peak currents of 62.17 µA, 162.41 µA, 282.55 µA and 401.03 µA. Similar to the reduction, the peak currents are increasing with increasing scan rate. The anodic peak potentials shift to higher values. At 50 mV s^{-1} the stagnant glassy carbon electrode shows the same behavior for a 1:1 DOL:DME with 1 M LiTFSI electrolyte and 4 mM S_8 as previously reported by Lu, He, and Gasteiger [35]. They have attributed the first and second cathodic peak to the reactions given in Eq. (1.8) producing S_8^{2-} and Eq. (1.10) producing S_4^{2-}. The octasulfide (S_8^{4-}) anion is not considered as it is believed to have only a short lifetime in low dielectric solvents, reacting directly to S_4^{2-} with similar magnitude as the reaction to S_8^{2-}.

The variation in scan rate allows to get additional information to possible chemical reactions. Indeed, the relation between anodic and cathodic peak currents $i_{p,a}/i_{p,c}$ increases with scan rate as indicated in Fig. 3.2b. The low ratio of anodic to cathodic current for low scan rates suggests that chemical reactions, e.g. as in Eq. (1.5) oxidize the electrochemically oxidizeable species with a certain rate. [141] Furthermore,

the current reaches ∼0 µA at the backward sweep after the potential 2.2 V where reactions resulting in the second cathodic peak are no longer causing a current. The electron transfer reaction of diffusing substrate to the electrode/electrolyte interface is hindered, therefore a chemical reaction between S_8 and polysulfides following the scheme in Eq. (1.6) must be present.

The above given experiment resembles a full state of charge, without accumulation of large amounts of intermediates. Reactions of such species may be observable mostly at lower state of charge. Thus, later sections analyze the CVGs for various states of charge during the discharge process to evaluate possible changes in species and reactions.

3.3.2 Cell discharge

Before conducting CVGs at various state of charge, the discharge behavior without disturbance by CV and OCP should be recorded as a reference. The discharge experiment is carried out in a stirred cell. The discharge curve, shown in Fig. 3.3, reveals two plateaus. The higher potential discharge plateau is at a potential of 2.36 V to 2.28 V and ends at a capacity of ca. 100 mA h g^{-1}. The lower plateau has a potential between 2.13 V and 2.00 V and yields an additional capacity of ca. 80 mA h g^{-1}. In between these plateaus is a transition phase starting at 2.28 V until 2.13 V with a capacity of ca. 30 mA h g^{-1}. In total the capacities add up to 238 mA h g^{-1}. This corresponds to 14.23 % of the theoretical value of 1672 mA h g^{-1} for the complete reduction of the dissolved S_8. There are various reasons for the low capacity of the cell that are well known in the literature [142], e.g. the formation of Li_2S_2 and Li_2S which block the electrode/electrolyte interface and transport limitations. The low ratio of active area to volume of reactants for the setup may explain the very low values observed here.

The two plateaus in Fig. 3.3 can be attributed to different electron transfer reactions that take place at different formal potentials. The first plateau corresponds to the first peak observed in the CV because of similar potentials. To further analyze the reactions, the discharge is combined with CV measurements in the procedure displayed in Fig. 3.1.

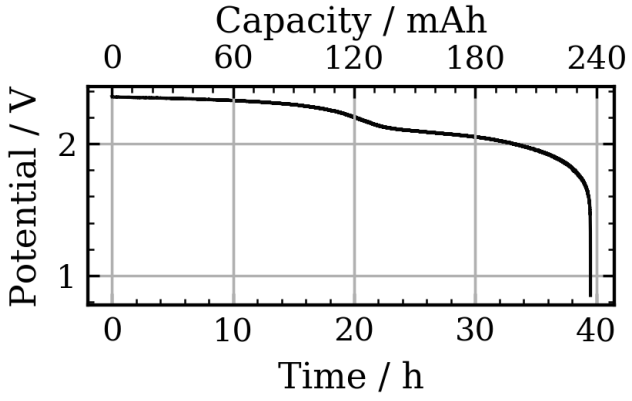

Figure 3.3: Discharge experiment with a cathodic current of 70 µA in the stirred three electrode cell. Reduction was performed at a glassy carbon electrode in 4 mM S_8 1.0 M LiTFSI, 1:1 DOL:DME.

3.3.3 Open circuit and cyclic voltammetry at different states of charge

The results of this combined experiment of OCP, CV and discharge measurements are shown in Fig. 3.4 and Fig. 3.5. Fig. 3.4 a and b display the current and potential behavior of the cell during cycle ten, which is used for illustration of the method. Directly after completing the discharge part of cycle nine, the progression of OCP vs. time of cycle ten can be studied. It is increasing from 2.365 V for ca. 10 min until it reaches a constant potential of 2.42 V. The subsequent CV is recorded from this equilibrium state. After the CV measurement, the OCP does not show any noticeable shift in potential, suggesting that no major changes occurred in solution or electrode due to CV or further equilibration during CV. The last step of the exemplary cycle is the discharge of the cell, where the potential drops fast at the beginning and reaches a lower gradient of $-3.17\,\mu A\,h^{-1}$ afterwards.

Fig. 3.4c displays the OCP in the period prior to the CV for all cycles. The behavior of each individual cycle, except for the first, is similar to the tenth, showing a rapid relaxation to higher potential and subsequent equilibration. The equilibrium value of the OCP is decreasing monotonously in the course of cycles. In contrast, the initial OCP values observed directly after the discharge sequence differ strongly and pass through a local minimum at the tenth cycle. These differences in relaxation behavior

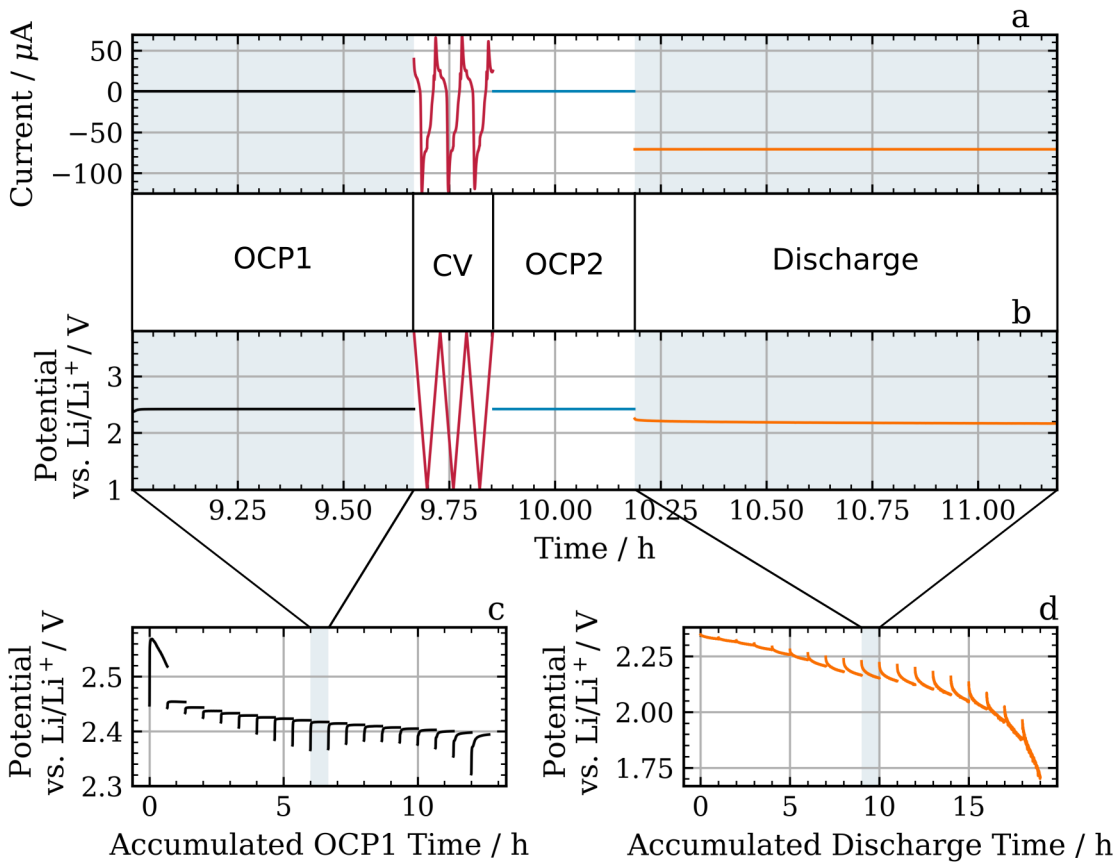

Figure 3.4: Results of cycle ten of the combined open circuit potential, cyclic voltammetry and discharge experiment according to Fig. 3.1. (a) Measured current during the experiment, (b) measured potential during the experiment, (c) Open circuit potential before the cyclic voltammetry in all cycles, (d) discharge curves of all cycles of 1 h discharge.

strongly indicate changes in the prevalent species and in the chemical reactions taking place during discharge. Overall, the monotonously decreasing equilibrium OCP indicates that the present polysulfides in solution causing the mixed potential are continuously decreasing in length. The initial OCP is strongly affected by the presence of medium size polysulfides directly after discharge. These disproportionate to longer and shorter polysulfides according to Eq. (1.5) or are reacting with S_8 to longer polysulfides according to Eq. (1.6) leading to the observed relaxation behavior. The amount of relaxation in the OCP has a local maximum around the tenth cycle

revealing the strongest influence of disproportionation in this cycle. Thus, the overall concentration of polysulfides during discharge reaches a maximum where also the initial OCP has a local minimum. Subsequently, the amount of short polysulfides in solution decreases resulting in the increasing initial OCP because longer chain polysulfides gain more influence on the mixed potential. The decreasing concentration of short polysulfides can be explained by the production of S^{2-} by disproportionation and its precipitation, as suggested by Kolosnitsyn et al. [143]. This is also supported by the fact that relaxation behavior decreases, implying that the solution is closer to equilibrium after discharge. The chemical equilibrium has shifted to shorter polysulfides explaining lower equilibrium OCP.

Based on these observations, the OCP reveals two phases of the S_8 reduction mechanism. In the first phase, the S_8 relaxation behavior increases and disproportionation of shorter polysulfides leads to long chain polysulfides. At the same time overall polysulfide concentration is increasing until reaching the local minimum in the initial OCP and the maximum in relaxation behavior. The second phase starts with the precipitating S^{2-} and the consequent decrease in polysulfide concentration in solution. Relaxation behavior decreases because the solution is closer to equilibrium after discharge.

The discharge potential shown in Fig. 3.4d can be divided in similar phases. The first seven cycles reveal no significant potential decrease during discharge. Maintaining this high discharge potential requires a sufficiently high concentration of long polysulfides. The initially dissolved amount of S_8 is the main factor here. Additionally, the OCP relaxation behavior revealed the important role of chemical production of long chain polysulfides during this discharge period to keep the OCP at high level. After this, the potential drops substantially at the beginning of discharge, reaching a lower value and is leveling off. In this second phase, the amount of long polysulfides is only sufficient to keep the potential high for a short instance. The main part of electrochemical reduction is caused by shorter polysulfides taking place at a lower potential. Diffusion of S_8 to the electrode/electrolyte interface might still be present, but due to chemical reactions with short polysulfides (Eq. (1.6)) polysulfides are produced that react at a lower potential. Relaxation and diffusion during the OCP phases of each cycle create the long polysulfides that cause the initial high potential during discharge.

The observed phases revealed by the OCP and the discharge potential correspond to the higher and lower potential discharge plateaus of typical LSB that are also visible in

Fig. 3.3. Therefore, cycle one to nine belong to the higher potential discharge plateau, cycle ten to 19 belong to the lower potential discharge plateau. The important role of relaxation behavior in the mechanism has already been pointed out. Analysis of the CVGs will give a deeper insight into the occurring electron transfer reactions on the two plateaus.

CV is the second part of each cycle starting from the equilibrium potential with a scan rate of $50\,\mathrm{mV\,s^{-1}}$. The results are displayed in Fig. 3.5. The qualitative shape of the initial CV of cycle one is similar to that of the CV experiment in Fig. 3.2a, initially showing two peaks during reduction and one during oxidation. Throughout the cycles of the higher potential discharge plateau, there is a steep increase of current at a potential of ca. 2.4 V which flattens only after the tenth cycle. The origin corresponds to the higher potential discharge plateau OCP. Thus, the following peak is caused by the main electron transfer reaction of the higher potential discharge plateau. The peak current of the first cathodic peak decreases constantly for each cycle, while shifting to lower potentials. The general shape of the peak does not change, as it stays narrow. In contrast to the first peak, the second disappears after the third cycle. Both effects suggest a decrease of reactant concentration or in case of the second peak, disappearance of certain species or inability of them to react with electron transfer after the third cycle. This supports the finding and conclusion drawn from Fig. 3.2c and d, that on the higher potential discharge plateau the reaction mechanism is dominated by long polysulfide reduction.

In Fig. 3.5 the anodic current initially exhibits one anodic peak and a small plateau. After three cycles, the peak splits up into two separated peaks from cycle three to ten. The first peak appears at a peak potential of 2.43 V and has a peak current of 17.23 µA while the second appears at a peak potential of 2.74 V and has a peak current of 82.60 µA. Thus, two electron transfer reactions were initially overlapping and invisible in the conventional CV in Fig. 3.2. These are caused by electrochemical oxidation of short polysulfides. Their independence is obvious, due to the fact that the first peak disappears in cycle eleven. The second cathodic peak is associated with the first anodic peak, as the disappearance of the cathodic peak correlates with the separation into two anodic peaks, where the first decreased significantly. This also points to an electron transfer reaction, that is unable to proceed.

During the lower potential discharge plateau, after cycle ten, the cathodic peak is getting broader, indicating overlapping electron transfer reactions. The origin has

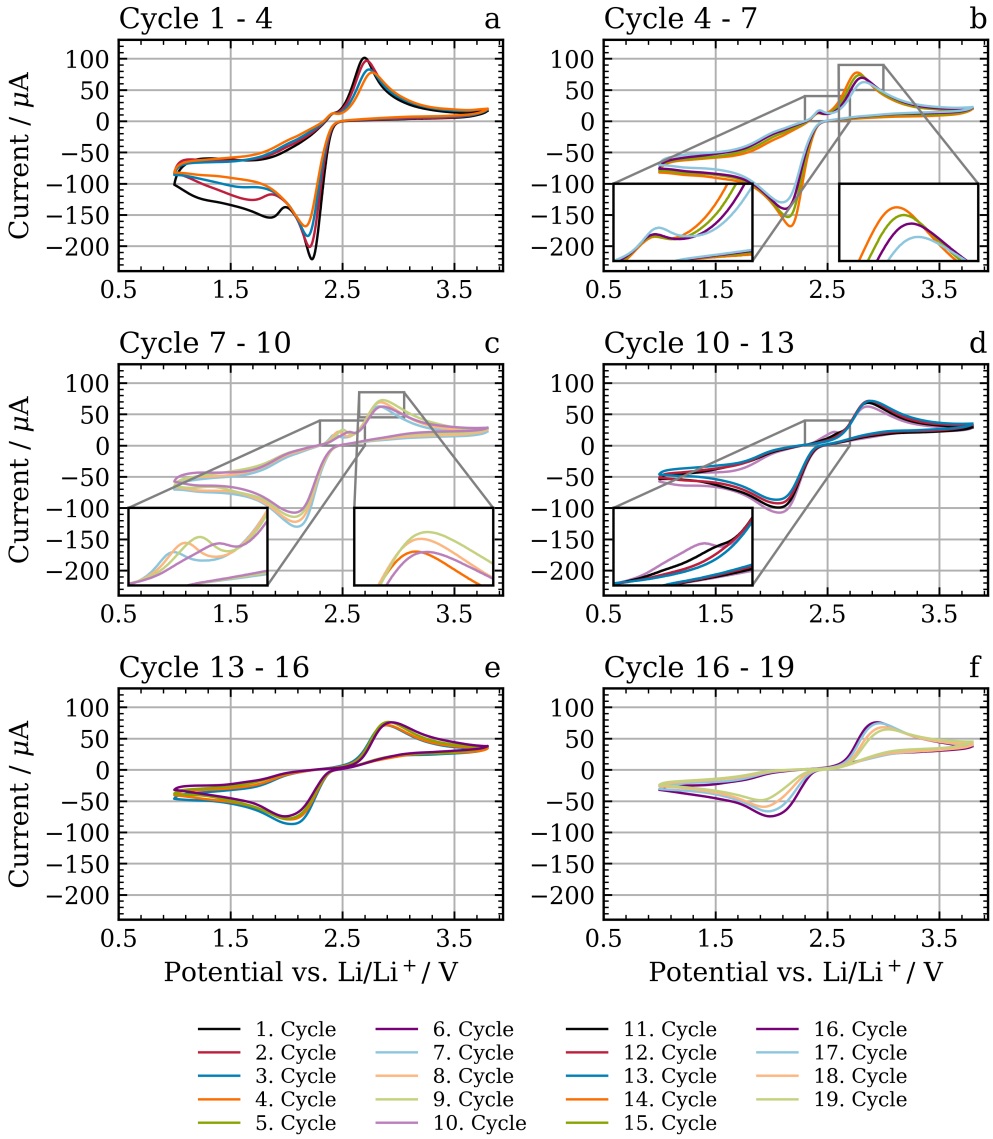

Figure 3.5: Cyclic voltammograms measured with a scan rate of 50 mV s^{-1} at different states of charge in a 1:1 DOL:DME with 1 M LiTFSI electrolyte and 4 mM S_8.

not changed because of the presence of long chain polysulfides that were formed through relaxation during OCP measurement. However, the former steep increase now flattens out and the peak potential is significantly shifted to lower potentials. Thus, the dominant electron transfer reactions are now due to shorter polysulfides

as in Eq. (1.11). Due to low S_8 utilization on the higher potential discharge plateau S_8 is still diffusing to the electrode/electrolyte interface. High reactivity of S_8 with polysulfides of short chain length reduces the amount to a point where there is no peak visible in the CVs.

The discharge experiment with CV was repeated with a variation of scan speeds in order to see if additional reactions may be visible that are covered at other scan rates. The resulting CVs are shown in Fig. 3.6. For all different scan rates, the reduction starts at the same potential of ca. 2.45 V. With increasing scan rate the potential of the first peak shifts slightly to lower potentials and the current is strongly increasing. The second cathodic peak is only visible for a scan rate of $10\,\mathrm{mV\,s^{-1}}$ and $100\,\mathrm{mV\,s^{-1}}$, at $1000\,\mathrm{mV\,s^{-1}}$ it disappears. The electron transfer reaction causing the cathodic current is dominant and overlaps the second at fast scan rates. Therefore, the process is either hindered by chemical reaction, a transport or an adsorption process that is not able to keep up with the scan rate. No further additional peaks are visible compared to $50\,\mathrm{mV\,s^{-1}}$. The observed increase in peak current ratios for increasing scan rates in Fig. 3.2 gets confirmed by the results in Fig. 3.6a however this effect is distinct after 3 h and 8 h. Thus, the influence of chemical reactions decreases on the lower potential discharge plateau.

3.3.4 Reduction mechanism of sulfur

The differences between discharge curves with and without relaxation time and the relaxation behavior of the OCP as well as the CVGs as a function of state of charge yield important information concerning the electron transfer reaction step, their interplay with chemical reactions and the prevalence of certain reactant species. Based on these observations, a reaction mechanism is proposed and discussed in the following. The first reaction appearing at the higher potential discharge plateau is attributed to dissolved S_8 reacting to S_8^{2-} as already reported various studies summarized in Chapter 1.3.

$$S_8 + 2\,e^- \rightleftharpoons S_8^{2-} \tag{3.1}$$

A further step taking place at this plateau is the reduction of S_8^{2-} to S_8^{4-}. Lu, He, and Gasteiger [35] already assigned a short lifetime to S_8^{4-} in DOL:DME with LiTFSI

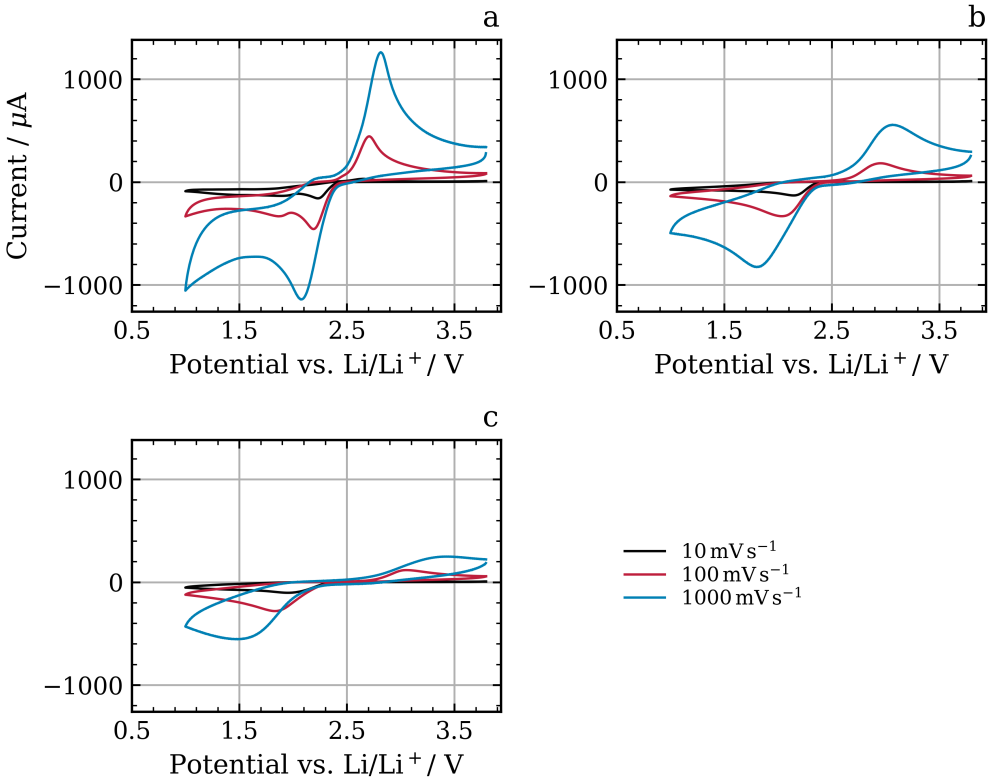

Figure 3.6: Cyclic voltammetry with scan rates of $10\,\mathrm{mV\,s^{-1}}$, $100\,\mathrm{mV\,s^{-1}}$ and $1000\,\mathrm{mV\,s^{-1}}$ in the combined experiment with open circuit potential measurements and discharge for a glassy carbon electrode at (a) initial state, (b) 3 h discharge and (c) 8 h discharge in a 1:1 DOL:DME with 1 M LiTFSI electrolyte and 4 mM S_8.

electrolyte. Therefore, the S_8^{4-} molecule decomposes further into two S_4^{2-}.

$$S_8^{2-} + 2\,e^- \rightleftharpoons S_8^{4-} \tag{3.2}$$

$$S_8^{4-} \longrightarrow 2\,S_4^{2-} \tag{3.3}$$

Taking into account the potential relaxation behavior and decreasing ratio of the peak currents in Fig. 3.2b at decreasing scan rates, the chemical reactions have to have a strong influence and are diminishing the amount of S_4^{2-}. Referring to Eq. (1.5) and (1.6) a chemical equilibrium will be reached by disproportionation of the S_4^{2-} ion and subsequent reactions. Assary, Curtiss, and Moore [78] identified S_2^{2-}, S_3^{2-} and

S_4^{2-} to be the major intermediates because their existence is advantageous, and Wang et al. [144] also named S_n^{2-} ($n = 2 - 5, 7, 8$) to be the most stable. Thus, the system seeks towards an equilibrium of polysulfides with longer and shorter chain length than initially present. The process of reaching this equilibrium seems to be relatively slow and is the cause of significant delay in establishing a stable OCP. The observed relaxation to almost the initial OCP is a good indicator for the production of long chain polysulfides, e.g. S_8^{2-}, and S_8 as they can be found at the start of discharge. At the minimum of the initial OCP, precipitation of S^{2-} is initiated which indicates the end of the higher potential discharge plateau.

After cycle ten, the recreated long polysulfides are present only at low concentrations and electron transfer reactions of shorter polysulfides become dominant as shown by the fast potential drop during discharge. The lower potential discharge plateau is therefore attributed to electron transfer reactions of short polysulfides as in Eq. 1.12; this study does not allow to identify a dominant reaction. Diffusing S_8 is not reacting directly at the electrode/electrolyte interface, but reacting chemically with produced polysulfides as no peak caused by Eq. (3.1) is visible in CV at low SoC. The anodic and cathodic peak currents are almost equal in the CVGs of the lower potential discharge plateau. Thus, these electron transfer reactions are reversible.

The OCP shows less relaxation behavior indicating, that the reduction products of the discharge phase are closer to chemical equilibrium. Fig. 3.7 shows the mechanism assumed to take place during discharge.

3.4 Conclusion

In this chapter further details of the S_8 reduction mechanism are determined by studying changes of relaxation behavior of galvanostatic discharge and OCP during discharge. Analysis of CV at different states of charge with different scan rates gave valuable insights into the nature of reactants and reactions as a function of SoC.

The prevailing reduction reactions, their reversibility and the electrode performance strongly depend on the chemical disproportionation and the equilibrium between the polysulfides. This is observable in the CV measurements and in the SoC-specific relaxation behavior during the OCP measurements. Furthermore, the CV measurements during discharge showed the dependency of the electron transfer

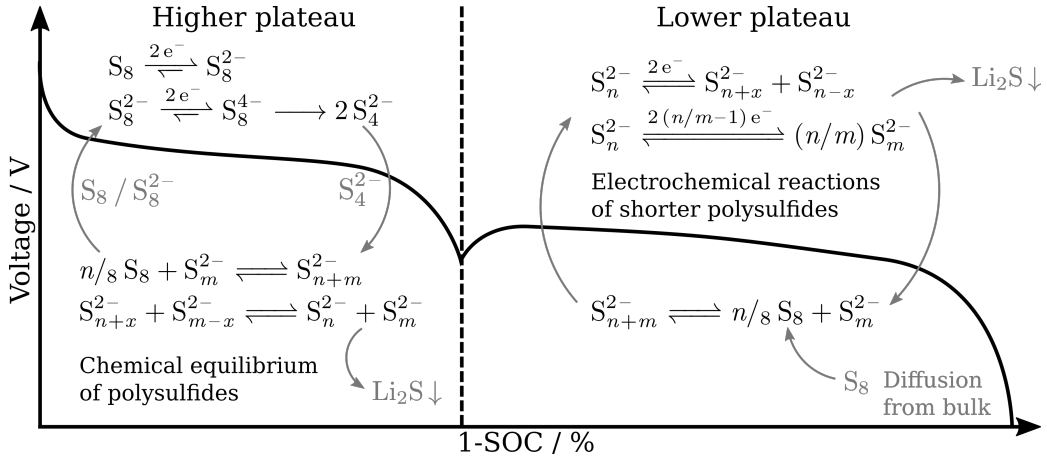

Figure 3.7: Illustration of mechanism of electron transfer and chemical reactions as a function of state of charge.

reactions on the SoC. While S_8 and long chain polysulfides are reacting on the higher potential discharge plateau, polysulfides with shorter chain length reduce at the potential of the lower potential discharge plateau. Additionally, the reaction is becoming more reversible in course of discharge showing the decreasing portion of worse oxidizeable species.

The presented insights and data now allow to formulate sound experimentally validated non-formal reaction kinetic models, which is done in Chapter 5. These give a detailed quantitative insight into the complex interaction of electron transfer and chemical reactions. However, further information about the involved species at different SoC facilitate the determination of a physically motivated mechanism. A HPLC study described in the next Chapter 4 is conducted to deliver these additional information.

Chapter 4

Spectroscopic analysis of sulfur and polysulfides during discharge

4.1 Introduction

A more detailed understanding of the occurring species during S_8 reduction in the LSB will be investigated by characterization of the electrolyte composition during discharge. The most promising analysis method for species identification and quantification in literature as described in Chapter 1.4 is HPLC-MS analysis. It enables to characterize the dissolved polysulfides produced in the electrolyte during galvanostatic discharge. The problematic chemical disproportionation of different polysulfides, that would continuously change the composition, is eliminated by derivatization of unstable polysulfides into stable dimethyl-sulfides. Therefore, the original composition of the electrolyte is maintained for analysis [36, 145]. HPLC separates the polysulfides depending on their chain lengths and each dimethyl polysulfide can be identified based on the monotonous relationship between retention time and chain length [36, 82, 107, 110–112]. Except for S^{2-}, all polysulfide ions and elemental sulfur can be separated and identified by HPLC-MS after derivatization [36, 146]. In this chapter the change of electrolyte composition with SoC reveals the species involved in the electron transfer and chemical reactions. This proves the proposed mechanism and kinetics of Chapter 3 and provides additional insights needed for simulation.

4.2 Experimental set-up

A lithium sulfur cell was established, using the established setup of Chapter 3.2.1. A glassy carbon electrode with a flat round tip with an area of $0.196\,cm^2$ (Pine Research

Instrumentation, Durham, NC) was used as working electrode. The Counter electrode was prepared using Li foil (99.9 %, Merck KGaA). The electrodes were immersed in 15 mL liquid electrolyte consisting of LiTFSI (SigmaAldrich) 1 mol in a 1:1 mixture of DOL (SigmaAldrich)/DME (SigmaAldrich). Cyclic octasulfur (99.9 %, Merck KGaA) was added as active material with a concentration of 4 mmol.

Galvanostatic discharge is used to investigate the discharge at a constant current density of 3.57 A m^{-2}, until a potential of 0.6 V is reached to ensure deep discharge. A Gamry Reference 3000 is used as galvanostat. After reaching this limit the discharge was terminated. 200 µL of electrolyte is taken out of the cell at different SoC, at 100 % SoC, 87.1 % SoC, 40.3 % SoC and 0 % SoC. Immediate derivatization using the established method of Kamyshny et al. [145] is performed by adding 350 µL methanol and 50 µL methyl trifluoromethanesulfonate (MeOTf) (99.9 %, Sigma Aldrich). The occurring reaction follows Eq. (4.1) :

$$S_n^{2-} + 2\,CF_3SO_3CH_3 \longrightarrow (CH_3)_2S_n + 2\,CF_3SO_3^- \tag{4.1}$$

Preparations and electrochemical experiments were performed in argon atmosphere at 25 °C.

Chromatographic separation of the sample is performed on Thermo Scientific, Dionex UltiMate 3000 UHPLC + Focused, using a C_{18} separation column (Thermo Scientific Hypersil GOLD, particle size 1.9 m, dimension (mm) 150 x 2.1) at a flow rate of 0.20 mL min^{-1} with the mobile phase consisting of 75 % methanol (HPLC-MS Grade, Sigma Aldrich) and 25 % water. Therefore, a RP-HPLC is performed (find details about RP-HPLC in Chapter 2.2). The injection volume is 5 µL. The complete flow exiting the HPLC is entering into a Dionex UltiMate 3000 diode array detector (DAD) where ultraviolet wavelength ranges from 190 nm to 400 nm are recorded. The samples are then introduced into Thermofischer quadrupole MS. For the MS detector, APCI positive mode was set as follow: Capillary voltage 3 kV, Corona current 15 µA, Vaporizer temperature 200 °C, nitrogen gas flow was 12 L min^{-1} for drying gas flow, nebulizer pressure was 45 psi. The m/z-ratio was recorded from 40 to 400. All HPLC-MS data was analyzed in the Chromeleon software (Dionex, Version 7.20) using the National Institute of Standards and Technology library by the U.S. Department of Commerce [147].

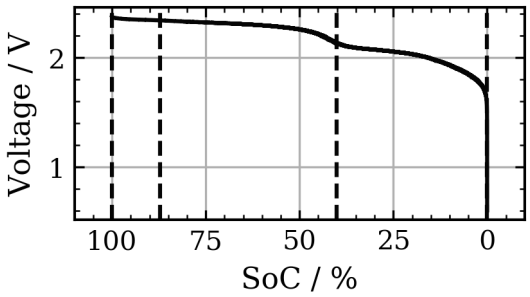

Figure 4.1: Discharge voltage curve of the investigated cell vs. state of charge. The state of charge at which samples for HPLC analysis were taken are indicated by dotted lines.

4.3 Results and discussion

In the following, the compositions of the electrolyte at different SoC will be investigated. The examined system shows the characteristic discharge plateaus of LSBs, Fig. 4.1. The higher potential discharge plateau exhibits a potential of >2.3 V before the transition phase. At ∼2.1 V the lower potential discharge plateau begins. The lower potential discharge plateau is relatively short indicating a low rate capability of the cell.

Fig. 4.1 indicates the SoCs when the samples are taken. While the first and last sample is taken at the beginning and the end of discharge, the second sample is taken at the higher potential discharge plateau and the third at the lower potential discharge plateau. Identification of species is done using HPLC-MS as illustrated in Fig. 2 in the appendix. Only analysis results taken at a wavelength of 210 nm are shown and discussed in this work, because of the strongest UV-adsorption of S_8 and polysulfides at this wavelength.

The chromatogram at 100 % SoC (Fig. 4.2a) shows two peaks. The first peak with a retention time of 21.2 min is identified as DOL and the second peak with a retention time of 35 min is identified as S_8. The absence of other peaks assures that no polysulfides are present at the beginning of galvanostatic discharge. Analyzing the chromatogram at 87.1 % SoC, seven additional peak are observed and generation of polysulfides can therefore be confirmed. Except for the fourth and the last peak, all peaks are present until the end of discharge, as seen in Fig. 4.2c and d. In addition,

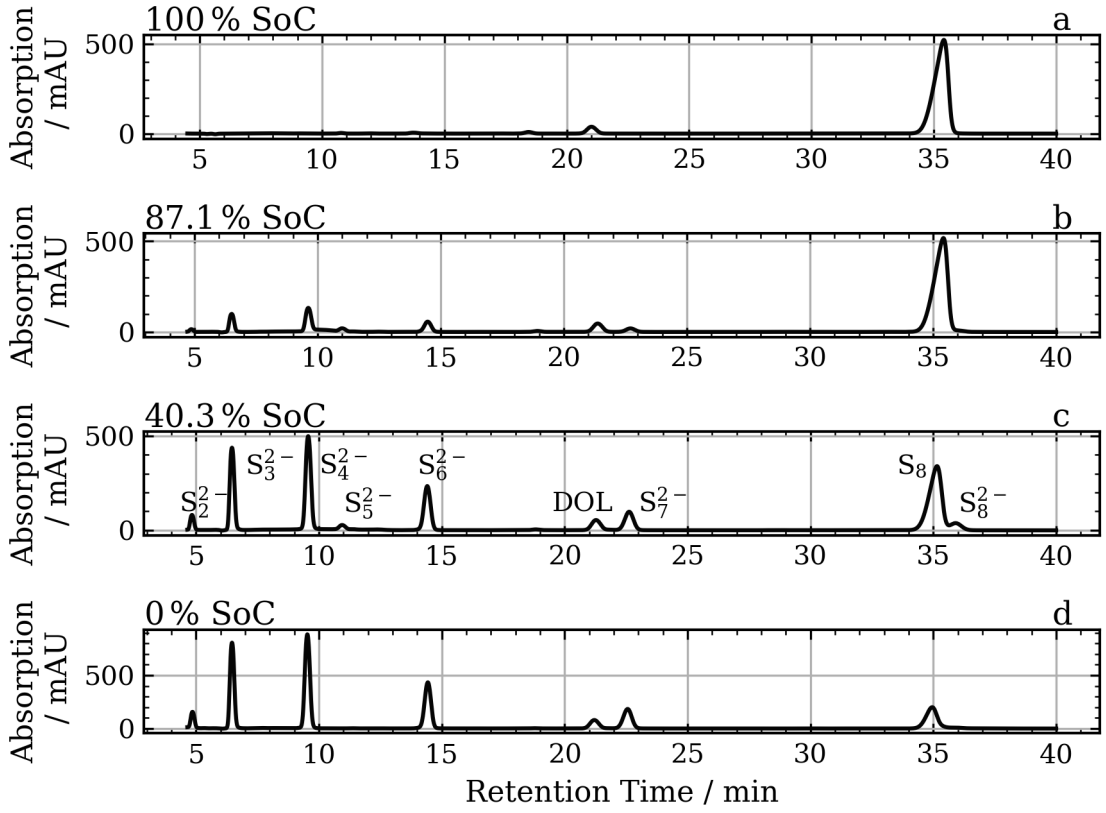

Figure 4.2: Chromatograms of separated polysulfides at different states of charge.

Table 4.1: Relative areas of polysulfides at different SoC.

Species	Retention Time / min	Relative Area / %			
		100 % SoC	87.1 % SoC	40.3 % SoC	0 % SoC
S_8	35	100	82.6	43.6	33.2
S_8^{2-}	36.8	0	0	1.8	0
S_7^{2-}	22.3	0	1.4	6.1	8
S_6^{2-}	14.1	0	3.3	11.4	14.3
S_5^{2-}	11	0	1.2	1.6	0
S_4^{2-}	9.2	0	6.7	20.3	23.5
S_3^{2-}	6.1	0	4	14.5	18
S_2^{2-}	4.8	0	0.5	2.3	3.2

an increase in these peaks areas can be observed throughout galvanostatic discharge. At the same time the S_8 peak decreases in peak area (Fig. 4.3).

The identification of polysulfides is done by the combined results of three different techniques (i) comparison of the retention times of standards, (ii) confirmation that polysulfides are present via MS, (iii) correlation of retention times with polysulfide chain lengths. [36, 82, 107, 110–112] Retention times of the individual separated species in the chromatogram in Fig. 4.2 can be seen in Tab. 4.1.

Additionally, Tab. 4.1 contains the peak areas related to the initial S_8 peak area. The S_8 peak area decreases from 100 % to 33.2 %, while the relative area of different polysulfides increases during the galvanostatic discharge. These are all detected by HPLC-MS. The concentration of S_8 is known to be 4 mmol at the beginning, therefore the final S_8 concentration is 1.32 mmol. This concentration change with SoC can be correlated to the electrochemical results. Regarding the systems response to the galvanostatic discharge at the end of each cycle in Chapter 3 potential drop is low while discharge is still at the higher potential discharge plateau. The assumption that S_8 concentration is high is verified. CV validates, that the electron transfer reaction of S_8 to S_8^{2-} and further to S_4^{2-} have high formal potentials. This results in a fast consumption of S_8 at the higher potential discharge plateau, which can also be confirmed by measuring the concentrations. Finally, S_8 concentration is still decreasing, when the electron transfer reactions yield a much lower mixed potential. This proves the presence of chemical reactions that consume S_8 at the lower potential discharge plateau.

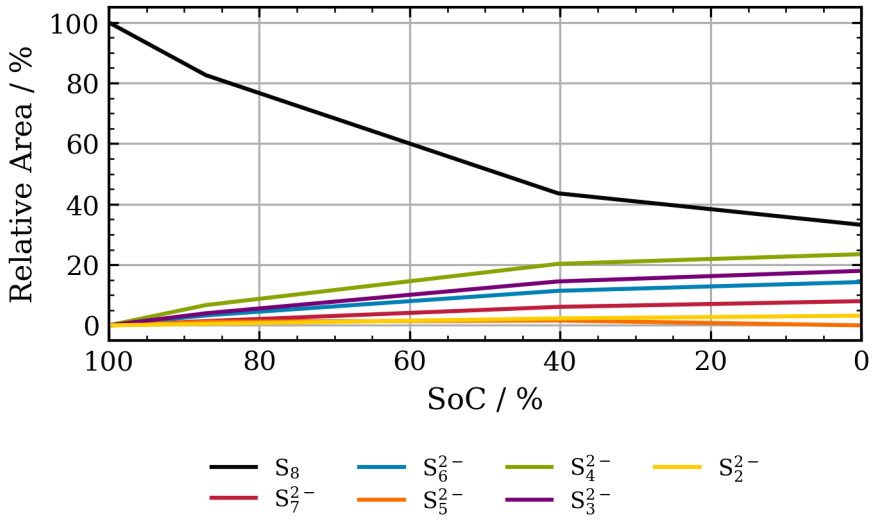

Figure 4.3: Relative areas of investigated polysulfides vs. state of charge.

Concentrations of polysulfides cannot be quantified because standards are unavailable. Multiple short chain polysulfide ions are produced during electrochemical reduction of S_8, of which S_3^{2-} and S_4^{2-} are the main products. Fig. 4.3 shows that the decrease of S_8 and increase of polysulfides is highest at the beginning and is slowing down during the experiment. This supports the assumption of the important role of disproportionation reactions. The polysulfide increase is higher at the higher potential discharge plateau compared to the lower potential discharge plateau indicating S^{2-} was produced at the end of the higher potential discharge plateau, which is not analyzed by HPLC-MS. Therefore, overall the results of the chemical analysis confirms the assumptions of the reaction mechanism from the previous Chapter 3.

4.4 Conclusion

Analysis of the electrolyte composition during discharge is done by applying rapid derivatization of polysulfides to suppress disproportionation reactions or chemical interaction with elemental sulfur. This allows for real time monitoring of the reduction progress at different points of time during galvanostatic discharge. Derivatization is reported not to influence the reduction products present when taking the sample

[36]. Therefore, identification of products of electron transfer and chemical reactions is feasible. In addition to CV measurements, this method provides complementary insights into the reaction mechanism and kinetics. The combination shows, that the higher potential discharge plateau is caused by reduction of S_8 and S_8^{2-}. In a circular route S_8 is reproduced by chemical reactions. All polysulfides are present from the beginning, showing the strong influence of disproportionation. Precipitation of S^{2-} is mainly present at the lower potential discharge plateau.

Simulation of dynamic experiments with a physicochemical model, that incorporates the determined reaction mechanism and is able to exhibit the characteristics of the resulting potential response, is needed to confirm the experimental results and deliver kinetic and transport parameters to further describe the examined system.

Chapter 5

Model supported analysis of the sulfur reaction mechanism[1]

5.1 Introduction

Various simulation studies have already proven to give deep insights into LSB processes as described in Chapter 1.3 [99–101, 103]. However, important aspects that are mostly unattended so far are the reaction kinetics. Mostly, a consecutive reduction of S_8 to increasingly short polysulfides has been assumed in modeling [61, 97, 102].

$$S_8 \longrightarrow S_8^{2-} \longrightarrow S_6^{2-} \longrightarrow S_4^{2-} \longrightarrow S_2^{2-} \longrightarrow S^{2-} \tag{5.1}$$

Dynamic methods with modeling supported analysis have shown great potential in identifying characteristics of reaction mechanisms and kinetics in different context. While they have not been systematically applied for S_8 reduction, they have been for methanol oxidation using electrochemical impedance spectroscopy [149], for oxygen reduction using nonlinear frequency responses [150], or even microbial glucose and acetate oxidation [151]. The latter study also presented a parameter sensitivity analysis and parameter identifiability study to identify parameter dependencies and reliability of the model and model parameters. A similar approach is followed in this work to identify a credible mechanism and kinetics.

In the Chapter 3, dynamic CV experiments are used to analyze the electron transfer reactions between electrode and S_8 or polysulfide species and its interaction with chemical reactions in the electrolyte. Further HPLC analysis, described in Chapter 4, gave the involved species and verified the underlying processes. Based on these results

[1] Parts of this chapter have been published in Schön and Krewer [148]

a 1-d physicochemical model is implemented to reveal the interaction of reaction and transport processes causing the CVG. In combination with sensitivity analysis, it reveals significant additional insights into the electron transfer and chemical reaction routes and aids in identifying complex interactions. The goal is to identify a feasible mechanism and kinetics of the lithium-sulfur electrode. With the experimental results of Chapter 3 the model is tailored to precisely analyze reaction currents, concentrations and reaction rate and their evolution over time and distance to the electrode/electrolyte interface. In addition, a sobol sensitivity analysis is performed to reveal the impact of transport and kinetic parameters on the current, i.e. electrode performance [152–154]. Two different scenarios are analyzed, (i) an EEC_{irr}-mechanism as simple generic mechanism to evaluate its applicability to give insights to the mechanism and (ii) a physically motivated E3C4-mechanism to enlighten different aspects of the reaction mechanism regarding reaction routes, transferred electrons and importance of transport in detail. This study is the first to demonstrate simulation of dynamic experimental with a realistic mechanism implemented. New fundamental information about the reaction kinetic and transport parameters can therefore be given.

5.2 Model

The modeled system consists of a static graphite working electrode immersed in a stagnant solution containing the electrochemically active S_8 as well as an excess of supporting electrolyte. The electron transfer reactions of S_8 and polysulfides take place at the surface of the working electrode. Chemical reactions take place in the electrolyte. Finally, the counter electrode completes an electrical circuit with the working electrode.

A chemical gradient will exist as a consequence of the different concentrations of the electrochemically active species depending on the distance to the electrode surface. The system will respond in order to balance the concentration gradient with the corresponding flux of material by diffusion. For typical electrochemical experiments, where a very large number of molecules are involved, the diffusion process can be described by the statistical Fick's laws [155] which accounts for the changes in concentration with time and location. Compared to the thickness of

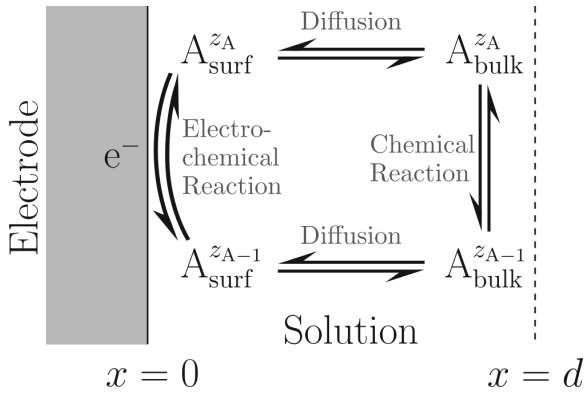

Figure 5.1: Illustration of modeled transport and kinetic processes implemented in the 1d-physicochemical model.

the diffusion layer $\delta \sim \sqrt{Dt}$ where D is the largest diffusion coefficient and t is the maximum simulated time, the area of the electrode is large, therefore a one dimensional approach is applicable.

The problem is thus reduced to one spatial dimension, x, which is the distance normal to the surface of the electrode. In general, the electrode is flat and large in comparison to the thickness of the diffusion layer δ. The electrode potential is not affected by a current. Experimentally this is the case when a reference electrode is used. Also, transport by ion migration in the electric field is eliminated by assuming an excess of electrolyte. Also, transport by ion migration in the electric field is eliminated by assuming an excess of electrolyte. In addition, the electrolyte is non-reactive, the environment is isotherm and substrates have a homogeneous concentration at beginning of the simulation. Fig. 5.1 illustrates the electrode with the underlying processes.

The implementation of the 1d-physicochemical model to simulate CV is described in Chapter 2.1.2.

Solving the ordinary differential equation system

In order to solve the ordinary differential equation system, the CVode solver, which was first introduced by Cohen, Hindmarsh, and Dubois [156] and implemented by Hindmarsh et al. [157] in the Suite of Nonlinear and Differential/Algebraic Equation Solvers, is applied. The most suitable numerical integration method for this set of

equations is the Backward Differentiation Formulas [158]. The generalized minimal residual method [159] is used as linear solver type. Absolute tolerances are 1×10^{-16} while relative tolerances are 1×10^{-6}. Convergence of the solution, especially regarding grid parameters was confirmed as refining the parameters lead to no visual changes of the CVs. programming interface for Python of this solver is provided by the Assimulo package [160].

Sensitivity analysis

To evaluate sensitivities of the CVs to parameters, a variance-based global sensitivity analysis was applied [152, 153]. Through this global sensitivity analysis, the variance of the output of the system is decomposed into fractions, which can be attributed to model parameters or sets of model parameters. These fractions, so called Sobol indices, are directly interpreted as values of sensitivity that are measured across the whole input space [154]. This method also allows to reveal correlations between parameters. The first-order sensitivity index, Φ_i, measures the direct variance-based sensitivity. This is the contribution to the output variance of the main effect of an examined parameter, therefore it measures the effect of varying this parameter alone, but averaged over variations in other input parameters. It is normalized by the total variance to provide a fractional contribution. The sum of first-and higher-order interaction indices $\Phi_{i,j}$, $\Phi_{i,j,k}$, ... implicates that,

$$\sum_{i=1}^{d} \Phi_i + \sum_{i<j}^{d} \Phi_{i,j} + \cdots + \Phi_{1,2\ldots d} = 1. \tag{5.2}$$

In order to calculate the variance, the number of samples is calculated by $N(2D+2)$, with D the number of model inputs, where in this study the argument N is set to be 1000 [152–154]. The Python implementation of the sensitivity analysis is realized in the SALib package [161].

5.3 Reaction mechanisms and governing equations

All simulated data is compared to experimentally measured CVGs taken from Chapter 3, see Fig. 3.2. At $100\,\mathrm{mV\,s^{-1}}$ the shape of the CVG in Fig. 3.2 shows

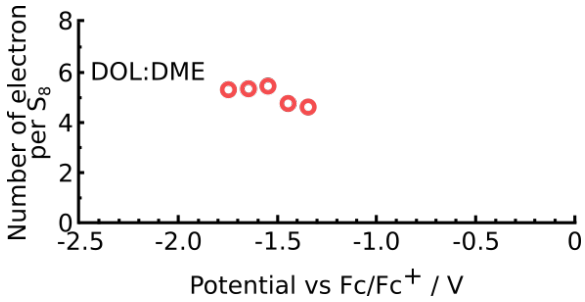

Figure 5.2: Transferred electrons during potentiostatic operation over potential of a glassy carbon electrode immersed in 1:1 DOL/DME electrolyte with 1 mol LiTFSI salt measured using. The number of electrons transferred per S_8 is identified by applying the Koutecký–Levich equation based on sulfur and polysulfide diffusion coefficients determined by analyzing the inverse of the rotation speed and transient time in potential step experiments using a rotating disk electrode. [35]

two cathodic peaks at 2.21 V and 1.91 V with peak currents of −428.29 µA and −314.12 µA. After the second cathodic peak, the system exhibits the diffusion limited current which is overlapping with an electrolyte degradation reaction. During the reverse scan, the current changes to zero at ∼2.0 V and remains at zero before electron transfer to the electrode causes the anodic peak with a peak potential of 2.69 V and a current of 401.03 µA.

Two reaction mechanisms are evaluated in the following towards their applicability to reproduce the experimental electrochemical behavior. The first mechanism represents the simplest generic option to reproduce the main characteristic features of the CV from a top-down view, with only the electrochemical result as foundation, and is an EEC_{irr}-mechanism. The second is named E3C4-mechanism containing three electron transfer and four chemical reactions, which allows to analyze all characteristics of the CVs, but at the expense of higher complexity. The chemical and electron transfer reactions implemented in the E3C4-mechanism were chosen bottom-up with the foundation of physical plausibility.

EEC-mechanism

In the first scenario, the experimental CV data is analyzed by a mechanism containing two reversible electron transfer steps followed by an irreversible chemical

reaction, which is known as EEC_{irr}-mechanism. This mechanism is derived from the experimental results, where two phenomena are obvious: (i) Two cathodic peaks that originate from at least two electron transfer steps, and (ii) a decreasing anodic to cathodic peak current ratio with decreasing scan rate. The two cathodic peaks lead to the assumption of two electron transfer reactions with different formal potentials. For the total electron transfer in the potential window of 3.8 V to 1 V, Lu, He, and Gasteiger [35] propose a transfer of $5.4\,e^-\,mol_{S_8}^{-1}$. This is applied to the first electron transfer reaction Ia. The second electron transfer reaction IIa causes the second reduction peak, where two electrons are assumed to be transferred, giving the correct current response for the second peak. The decreasing peak ratio is assumed to be caused by a chemical reaction that consumes reactants that otherwise oxidize by the anodic electron transfer reaction. The irreversible step can indicate precipitation reaction of S^{2-}. As the reactions are empirically derived, X and Y are used instead of S_8 and polysulfide species. As a result the reaction mechanism is defined as:

$$X \rightleftharpoons \ldots \xrightleftharpoons{\text{-}5.4\,e^-} X^{5.4-} \tag{Ia}$$

$$X^{5.4-} \rightleftharpoons \ldots \xrightleftharpoons{\text{-}2\,e^-} X^{7.4-} \tag{IIa}$$

$$X^{7.4-} \longrightarrow \ldots \xrightarrow{+\,7.4\,Li^+} Y. \tag{IIIa}$$

Reduction of X results in the product $X^{5.4-}$ by consecutively transferring $5.4\,e^-$ from the electrode to the species. The amount of $5.4\,e^-$ is the accumulated sum of electrons that are transferred per mole of X. Here, underlying consecutive elementary reaction steps with single electron transfer are assumed with the last step being rate limiting. The same assumption holds for the reduction of $X^{5.4-}$ to $X^{7.4-}$, where only the slower of the two one-electron transfer reactions defines the reaction rate. Reversing the scan direction, does not change the hypothesis since these electron transfer steps are assumed to be reversible. This leads to the mass balances and kinetic equations system in Tab. 5.1 according to the described physicochemical model in Chapter 2.1.2.

E3C4-Mechanism

A majority of literature publications propose electron transfer reactions, where four electrons are transferred during two consecutive electron transfer steps, reducing S_8

Table 5.1: Mass balances and kinetic equation system of the $\mathrm{EEC_{irr}}$-mechanism.

Mass balances in the electrolyte:

$$\frac{\partial c_{\mathrm{X}}}{\partial t} = D_{\mathrm{X}} \frac{\partial^2 c_{\mathrm{X}}}{\partial x^2} \tag{5.3}$$

$$\frac{\partial c_{\mathrm{X}^{5.4-}}}{\partial t} = D_{\mathrm{X}^{5.4-}} \frac{\partial^2 c_{\mathrm{X}^{5.4-}}}{\partial x^2} \tag{5.4}$$

$$\frac{\partial c_{\mathrm{X}^{7.4-}}}{\partial t} = D_{\mathrm{X}^{7.4-}} \frac{\partial^2 c_{\mathrm{X}^{7.4-}}}{\partial x^2} - k_{\mathrm{f,III}a} c_{\mathrm{X}^{7.4-}} \tag{5.5}$$

$$\frac{\partial c_{\mathrm{Y}}}{\partial t} = D_{\mathrm{Y}} \frac{\partial^2 c_{\mathrm{Y}}}{\partial x^2} + k_{\mathrm{f,III}a} c_{\mathrm{X}^{7.4-}} \tag{5.6}$$

Boundary conditions:

$$\left(-D_{\mathrm{X}} \frac{\partial c_{\mathrm{X}}}{\partial x} \right)_{x=0} = \frac{i_{\mathrm{I}a}}{z_{\mathrm{I}a}\mathrm{F}} \tag{5.7}$$

$$\left(-D_{\mathrm{X}^{5.4-}} \frac{\partial c_{\mathrm{X}^{5.4-}}}{\partial x} \right)_{x=0} = -\frac{i_{\mathrm{I}a}}{z_{\mathrm{I}a}\mathrm{F}} + \frac{i_{\mathrm{II}a}}{z_{\mathrm{II}a}\mathrm{F}} \tag{5.8}$$

$$\left(-D_{\mathrm{X}^{7.4-}} \frac{\partial c_{\mathrm{X}^{7.4-}}}{\partial x} \right)_{x=0} = -\frac{i_{\mathrm{II}a}}{z_{\mathrm{I}a}\mathrm{F}}. \tag{5.9}$$

The remaining flux terms at the boundaries $x = 0$ and $x = \delta$ are zero.

Partial currents of electron transfer reactions Ia and IIa

$$i_{\mathrm{I}a} = z_{\mathrm{I}a}\mathrm{F}k_{\mathrm{I}a} \left(\exp\left(\frac{\alpha_{\mathrm{I}a}\mathrm{F}}{\mathrm{R}T} \left(E - E^0_{\mathrm{f,I}a} \right) \right) c_{\mathrm{X}^{5.4-}} - \exp\left(-\frac{(1-\alpha_{\mathrm{I}a})\,\mathrm{F}}{\mathrm{R}T} \left(E - E^0_{\mathrm{f,I}a} \right) \right) c_{\mathrm{X}} \right) \tag{5.10}$$

$$i_{\mathrm{II}a} = z_{\mathrm{II}a}\mathrm{F}k_{\mathrm{II}a} \left(\exp\left(\frac{\alpha_{\mathrm{II}a}\mathrm{F}}{\mathrm{R}T} \left(E - E^0_{\mathrm{f,II}a} \right) \right) c_{\mathrm{X}^{7.4-}} - \exp\left(-\frac{(1-\alpha_{\mathrm{II}a})\,\mathrm{F}}{\mathrm{R}T} \left(E - E^0_{\mathrm{f,II}a} \right) \right) c_{\mathrm{X}^{5.4-}} \right). \tag{5.11}$$

Total reaction current:

$$i = i_{\mathrm{I}a} + i_{\mathrm{II}a} \tag{5.12}$$

(reaction I) and S_8^{2-} (reaction II) [35, 36, 82, 85, 111]. This finding is confirmed by the conducted CV and HPLC studies described in Chapters 3 and 4. In this context it seems quite unrealistic, that $5.4\,e^-/mol_{S_8}$ transfer always jointly as assumed in the EEC_{irr}-mechanism. And as the mechanism cannot cover the variety of identified species, the more physically motivated E3C4-mechanism is investigated. Compared to the EEC_{irr}-mechanism, less electrons are transferred during the first two reduction steps. The missing electrons per mole S_8, that would therefore deliver a lower current, are supposed to be compensated by circular routes due to chemical reactions forming new S_8 (reaction Vb) [162]. The relaxation behavior of the investigated cell during OCP measurement, as well as the decreasing S_8 consumption at lower SoC during discharge, which is measured by HPLC (Fig. 4.3), confirms the presence of such reaction. Chemical reactions of short chain polysulfides that mainly involve S_4^{2-} to S_2^{2-} in reaction VIb and VIIb are also included taking into account the main products of HPLC analysis. The broad CV peaks at lower SoC (Chapter 3) result because S_4^{2-}, which is responsible for the reduction at the lower potential discharge plateau (IIIb), is strongly involved in these chemical reactions (IVb, Vb, VIb), that have been previously proposed. [36, 82] The proposed mechanism is as follows:

$$S_8 + 2\,e^- \rightleftharpoons S_8^{2-} \tag{Ib}$$
$$S_8^{2-} + 2\,e^- \rightleftharpoons S_8^{4-} \tag{IIb}$$
$$S_4^{2-} + 2\,e^- \rightleftharpoons 2\,S_2^{2-} \tag{IIIb}$$
$$S_8^{4-} \rightleftharpoons 2\,S_4^{2-} \tag{IVb}$$
$$3\,S_4^{2-} \rightleftharpoons S_8 + S_2^{2-} + 2\,S^{2-} \tag{Vb}$$
$$2\,S_3^{2-} \rightleftharpoons S_4^{2-} + S_2^{2-} \tag{VIb}$$
$$2\,S_2^{2-} \rightleftharpoons S_3^{2-} + S^{2-}. \tag{VIIb}$$

Applying the 1-d physicochemical model described in Chapter 2.1.2, this reaction mechanism leads to the mass balances for the electrolyte domain in Tab. 5.2.

Table 5.2: Mass balances and kinetic equation system of the E3C4-mechanism.

Mass balances in the electrolyte:

$$\frac{\partial c_{\mathrm{S}_8}}{\partial t} = D_{\mathrm{S}_8}\frac{\partial^2 c_{\mathrm{S}_8}}{\partial x^2} + r_{\mathrm{V}b} \tag{5.13}$$

$$\frac{\partial c_{\mathrm{S}_8^{2-}}}{\partial t} = D_{\mathrm{S}_8^{2-}}\frac{\partial^2 c_{\mathrm{S}_8^{2-}}}{\partial x^2} \tag{5.14}$$

$$\frac{\partial c_{\mathrm{S}_8^{4-}}}{\partial t} = D_{\mathrm{S}_8^{4-}}\frac{\partial^2 c_{\mathrm{S}_8^{4-}}}{\partial x^2} - r_{\mathrm{IV}b} \tag{5.15}$$

$$\frac{\partial c_{\mathrm{S}_4^{2-}}}{\partial t} = D_{\mathrm{S}_4^{2-}}\frac{\partial^2 c_{\mathrm{S}_4^{2-}}}{\partial x^2} + 2r_{\mathrm{IV}b} - 3r_{\mathrm{V}b} + r_{\mathrm{VI}b} \tag{5.16}$$

$$\frac{\partial c_{\mathrm{S}_3^{2-}}}{\partial t} = D_{\mathrm{S}_3^{2-}}\frac{\partial^2 c_{\mathrm{S}_3^{2-}}}{\partial x^2} - 2r_{\mathrm{VI}b} + r_{\mathrm{VII}b} \tag{5.17}$$

$$\frac{\partial c_{\mathrm{S}_2^{2-}}}{\partial t} = D_{\mathrm{S}_2^{2-}}\frac{\partial^2 c_{\mathrm{S}_2^{2-}}}{\partial x^2} + r_{\mathrm{V}b} + r_{\mathrm{VI}b} - 2r_{\mathrm{VII}b} \tag{5.18}$$

$$\frac{\partial c_{\mathrm{S}^{2-}}}{\partial t} = D_{\mathrm{S}^{2-}}\frac{\partial^2 c_{\mathrm{S}^{2-}}}{\partial x^2} + 2r_{\mathrm{V}b} + r_{\mathrm{VII}b} \tag{5.19}$$

Reaction rates:

$$r_{\mathrm{IV}b} = k_{\mathrm{f,IV}b} c_{\mathrm{S}_8^{4-}} - k_{\mathrm{b,IV}b} c_{\mathrm{S}_4^{2-}}^2 \tag{5.20}$$

$$r_{\mathrm{V}b} = k_{\mathrm{f,V}b} c_{\mathrm{S}_4^{2-}}^3 - k_{\mathrm{b,V}b} c_{\mathrm{S}_8} c_{\mathrm{S}_2^{2-}} c_{\mathrm{S}^{2-}}^2 \tag{5.21}$$

$$r_{\mathrm{VI}b} = k_{\mathrm{f,VI}b} c_{\mathrm{S}_3^{2-}}^2 - k_{\mathrm{b,VI}b} c_{\mathrm{S}_4^{2-}} c_{\mathrm{S}_2^{2-}} \tag{5.22}$$

$$r_{\mathrm{VII}b} = k_{\mathrm{f,VII}b} c_{\mathrm{S}_2^{2-}}^2 - k_{\mathrm{b,VII}b} c_{\mathrm{S}_3^{2-}} c_{\mathrm{S}^{2-}}. \tag{5.23}$$

Boundary conditions:

$$\left(-D_{\mathrm{S}_8}\frac{\partial c_{\mathrm{S}_8}}{\partial x}\right)_{x=0} = \frac{i_{\mathrm{I}b}}{z_{\mathrm{I}b}\mathrm{F}} \tag{5.24}$$

$$\left(-D_{\mathrm{S}_8^{2-}}\frac{\partial c_{\mathrm{S}_8^{2-}}}{\partial x}\right)_{x=0} = -\frac{i_{\mathrm{I}b}}{z_{\mathrm{I}b}\mathrm{F}} + \frac{i_{\mathrm{II}b}}{z_{\mathrm{II}b}\mathrm{F}} \tag{5.25}$$

$$\left(-D_{\mathrm{S}_8^{4-}}\frac{\partial c_{\mathrm{S}_8^{4-}}}{\partial x}\right)_{x=0} = -\frac{i_{\mathrm{II}b}}{z_{\mathrm{II}b}\mathrm{F}} \tag{5.26}$$

$$\left(-D_{\mathrm{S}_4^{2-}}\frac{\partial c_{\mathrm{S}_4^{2-}}}{\partial x}\right)_{x=0} = \frac{i_{\mathrm{III}b}}{z_{\mathrm{III}b}\mathrm{F}} \tag{5.27}$$

$$\left(-D_{\mathrm{S}_2^{2-}}\frac{\partial c_{\mathrm{S}_2^{2-}}}{\partial x}\right)_{x=0} = -2\frac{i_{\mathrm{III}b}}{z_{\mathrm{III}b}\mathrm{F}}. \tag{5.28}$$

The remaining flux terms at the boundaries $x = 0$ and $x = \delta$ are zero.

Partial currents of electron transfer reactions Ib, IIb and IIIb:

$$i_{\mathrm{I}b} = z_{\mathrm{I}b}\mathrm{F}\Delta x_1 k_{\mathrm{I}b}\left(\exp\left(\frac{\alpha_{\mathrm{I}b}\mathrm{F}}{\mathrm{R}T}\left(E - E^0_{\mathrm{f,I}b}\right)\right) c_{\mathrm{S}_8^{2-}} - \exp\left(-\frac{(1-\alpha_{\mathrm{I}b})\,\mathrm{F}}{\mathrm{R}T}\left(E - E^0_{\mathrm{f,I}b}\right)\right) c_{\mathrm{S}_8}\right) \tag{5.29}$$

$$i_{\mathrm{II}b} = z_{\mathrm{II}b}\mathrm{F}\Delta x_1 k_{\mathrm{II}b}\left(\exp\left(\frac{\alpha_{\mathrm{II}b}\mathrm{F}}{\mathrm{R}T}\left(E - E^0_{\mathrm{f,II}b}\right)\right) c_{\mathrm{S}_8^{4-}} - \exp\left(-\frac{(1-\alpha_{\mathrm{II}b})\,\mathrm{F}}{\mathrm{R}T}\left(E - E^0_{\mathrm{f,II}b}\right)\right) c_{\mathrm{S}_8^{2-}}\right) \tag{5.30}$$

$$i_{\mathrm{III}b} = z_{\mathrm{III}b}\mathrm{F}\Delta x_1\left(k_{\mathrm{III}b,\mathrm{f,el}}\exp\left(\frac{\alpha_{\mathrm{III}b}\mathrm{F}}{\mathrm{R}T}\left(E - E^0_{\mathrm{f,III}b}\right)\right) c_{\mathrm{S}_2^{2-}} - k_{\mathrm{III}b,\mathrm{b,el}}\exp\left(-\frac{(1-\alpha_{\mathrm{III}b})\,\mathrm{F}}{\mathrm{R}T}\left(E - E^0_{\mathrm{f,III}b}\right)\right) c_{\mathrm{S}_4^{2-}}^2\right). \tag{5.31}$$

Total reaction current:

$$i = i_{\mathrm{I}b} + i_{\mathrm{II}b} + i_{\mathrm{III}b} \tag{5.32}$$

Table 5.3: Identified parameters for the EEC_{irr}-mechanism.

D_X	$D_{X^{5.4-}}$	$D_{X^{7.4-}}$	D_Y
$m^2\,s^{-1}$	$m^2\,s^{-1}$	$m^2\,s^{-1}$	$m^2\,s^{-1}$
2.60×10^{-10}	7.6×10^{-10}	1.25×10^{-9}	3.64×10^{-10}
$E_{f,Ia}$	$E_{f,IIa}$	k_{Ia}	k_{IIa}
V	V	$m\,s^{-1}$	$m\,s^{-1}$
2.44	2.20	5.73×10^{-10}	1.64×10^{-10}
$k_{f,IIIa}$	$k_{b,IIIa}$		
s^{-1}	s^{-1}		
1.13×10^{-3}	0		

5.4 Parameterization

EEC-mechanism

Following the experimental conditions, the starting concentration of reactant X is 4 mmol, and initial concentrations of $X^{5.4-}$, $X^{7.4-}$ and Y are zero. The temperature is set to 293.15 K. The diffusion parameters are taken from Lu, He, and Gasteiger [35] where rotating ring-disk electrode measurements revealed a value of $2.6 \times 10^{-10}\,m^2\,s^{-1}$ for sulfur in 1:1 DOL:DME with 1 M LiTFSI. Charge transfer coefficients for each of the electron transfer reactions are chosen to be 0.5. Following the experimental procedure, CV is simulated for two cycles in a range between 3.8 V to 1.0 V whereas the evaluated part of the CV is the second cycle. At potentials lower than 1.8 V the experimental results show undesired side reactions of the electrolyte, that are not included in the model. Diffusion coefficients $D_{X^{5.4-}}$, $D_{X^{7.4-}}$, D_Y, as well as reaction constants k_{Ia} and k_{IIa}, formal potentials $E^0_{f,Ia}$ and $E^0_{f,IIa}$ of the electron transfer reactions and the reaction constants of the chemical reaction $k_{f,IIIa}$ and $k_{b,IIIa}$ are identified using a least square approach on the experimental CVs at $100\,mV\,s^{-1}$. They are given in Tab. 5.3.

E3C4-mechanism

The starting concentration of S_8 is set to 4 mmol, and initial concentrations of the remaining species are set to zero. The temperature is set to 293.15 K. The diffusion

parameter of S_8 is taken from Lu, He, and Gasteiger [35] with $2.6 \times 10^{-10}\,m^2\,s^{-1}$. Charge transfer coefficients for each of the electron transfer reactions are chosen to be 0.5. Following the experimental procedure, CV is simulated and recorded for two cycles in a range between 3.8 V to 1.0 V whereas the evaluated part of the voltammogram is the second cycle. At potentials <1.8 V, the experimental results show undesired side reactions not included. Diffusion coefficients of all polysulfides as well as reaction constants, formal potentials of the electron transfer reactions and the reaction constants of the chemical reaction are identified to reproduce the experimental data at $100\,mV\,s^{-1}$. They are given in Tab. 5.4. A local availability of S^{2-} is integrated at the electrode/electrolyte interface by choosing an artificially low diffusion coefficient for this species to account for its precipitation at the surface, which is not included in the model. For the here presented reaction kinetic modeling, integrating intricate inhomogeneous precipitation processes would heavily complicate the model and would distract from the focus of identifying the reaction kinetics. To assure quasi steady state of surface and solution, the second scan is used both in experiment and simulation.

5.5 Results and discussion

In the following, the two proposed kinetic models and their ability and shortcoming to describe the experimentally observed CV is discussed and a parameter sensitivity analysis elucidates the parameter impact. This procedure is first implemented for the EEC_{irr}-mechanism and then repeated for the more complex, physically motivated E3C4-mechanism.

EEC_{irr}-mechanism

In Fig. 5.3a the simulated CV of the model with EEC_{irr} kinetic is shown in comparison to the experiment. In addition, characteristic points in the experimental graph are marked from A to F, where B, C and E are points in time which correspond to oxidation and reduction peaks. It can clearly be seen, that the EEC_{irr}-mechanism matches the experiment in good agreement regarding all points except at low potential point D. The behavior at point D deviates significantly which is expected, because it is caused by electrolyte degradation, which is not included in the model. However,

Table 5.4: Identified parameters for the E3C4-mechanism.

D_{S_8}	$D_{S_8^{2-}}$	$D_{S_8^{4-}}$	$D_{S_4^{2-}}$
$m^2\,s^{-1}$	$m^2\,s^{-1}$	$m^2\,s^{-1}$	$m^2\,s^{-1}$
2.6×10^{-10}	2.6×10^{-10}	2.6×10^{-9}	7.6×10^{-10}
$D_{S_3^{2-}}$	$D_{S_2^{2-}}$	$D_{S^{2-}}$	$E_{\mathrm{fI}b,\mathrm{II}b}$
$m^2\,s^{-1}$	$m^2\,s^{-1}$	$m^2\,s^{-1}$	V
9×10^{-10}	1.25×10^{-9}	1×10^{-11}	2.44
$E_{\mathrm{f,III}b}$	$k_{\mathrm{I}b,\mathrm{II}b}$	$k_{\mathrm{f,III}b}$	$k_{\mathrm{b,III}b}$
V	$m\,s^{-1}$	$m\,s^{-1}$	$(m^3\,mol^{-1})\,m\,s^{-1}$
2.3	2×10^{-6}	7×10^{-8}	7×10^{-8}
$k_{\mathrm{f,IV}b}$	$k_{\mathrm{b,IV}b}$	$k_{\mathrm{f,V}b}$	$k_{\mathrm{b,V}b}$
s^{-1}	$m^3\,mol^{-1}\,s^{-1}$	$(m^3\,mol^{-1})^2\,m\,s^{-1}$	$(m^3\,mol^{-1})^3\,s^{-1}$
3.75	15	1	4
$k_{\mathrm{f,VI}b}$	$k_{\mathrm{b,VI}b}$	$k_{\mathrm{f,VII}b}$	$k_{\mathrm{b,VII}b}$
$(m^3\,mol^{-1})\,m\,s^{-1}$	$(m^3\,mol^{-1})\,m\,s^{-1}$	$(m^3\,mol^{-1})\,m\,s^{-1}$	$(m^3\,mol^{-1})\,m\,s^{-1}$
0.5	0.5	1	1

two parts of the simulated CV show a different characteristic. First, directly after point C the cathodic current decreases too fast compared with the experiment. The reason for this behavior is, that in the experiment more electrons per mole of substrate are transferred after the peaks. Second, during the positive scan at a potential of 2.0 V, a current approaching zero is expected which can also not be reproduced by the EEC_{irr}-mechanism. Here, the EEC_{irr}-mechanism exhibits a diffusion limited current, while the experimentally observed drop to zero indicates that sulfur (X) is not available at the surface for reduction despite sufficient sulfur concentration in the bulk. This in turn suggests that the mechanism misses a chemical reaction that consumes the reactant in experiments before it reaches the surface. In the following, reactions and concentrations are correlated to elucidate the origin of the CV features and dominant processes.

During the sweep to lower potentials, sulfur (X) is reduced to the intermediate $X^{5.4-}$ and this intermediate gets consecutively reduced to $X^{7.4-}$. The respective change of concentration is shown in Fig. 5.3b. The concentration of sulfur (X) at the electrode/electrolyte interface drops to zero, while the concentration of $X^{5.4-}$ increases and then it decreases again in favor of the final reduction product $X^{7.4-}$. Reduction of sulfur (X) starts and causes a cathodic current when the potential approaches the formal potential of reaction Ia, which is 2.44 V. Similarly, the formal potential of reaction IIa of 2.20 V is the potential at which reduction of $X^{5.4-}$ starts and current increases to form the second cathodic peak. At B and C, the concentrations have the highest gradient with respect to potential change. Here, reaction rates are maximal, resulting in the cathodic current peaks. When approaching point D, the concentrations at the surface are nearly constant, indicating a diffusion limitation of X to the electrode/electrolyte interface. At the surface sulfur (X) entirely reacts to $X^{7.4-}$, which diffuses away from the surface with the same magnitude.

When surpassing the formal potential of reaction IIa during the backward scan, the rate of $X^{5.4-}$ conversion to $X^{7.4-}$ decreases, resulting in two effects that are displayed in Fig. 5.3c. Firstly, the concentration of $X^{7.4-}$ at the electrode/electrolyte interface diminishes because of diffusion. Secondly, the concentration of $X^{5.4-}$ is increasing because the reaction rate Ia is still high at this potential. Reaching point E, reaction Ia stops and the concentration gradients for sulfur (X) and $X^{5.4-}$ with respect to potential pass their maximum resulting in the anodic peak. Finally, when approaching point F, the concentrations at the surface are nearly constant and only few reduced

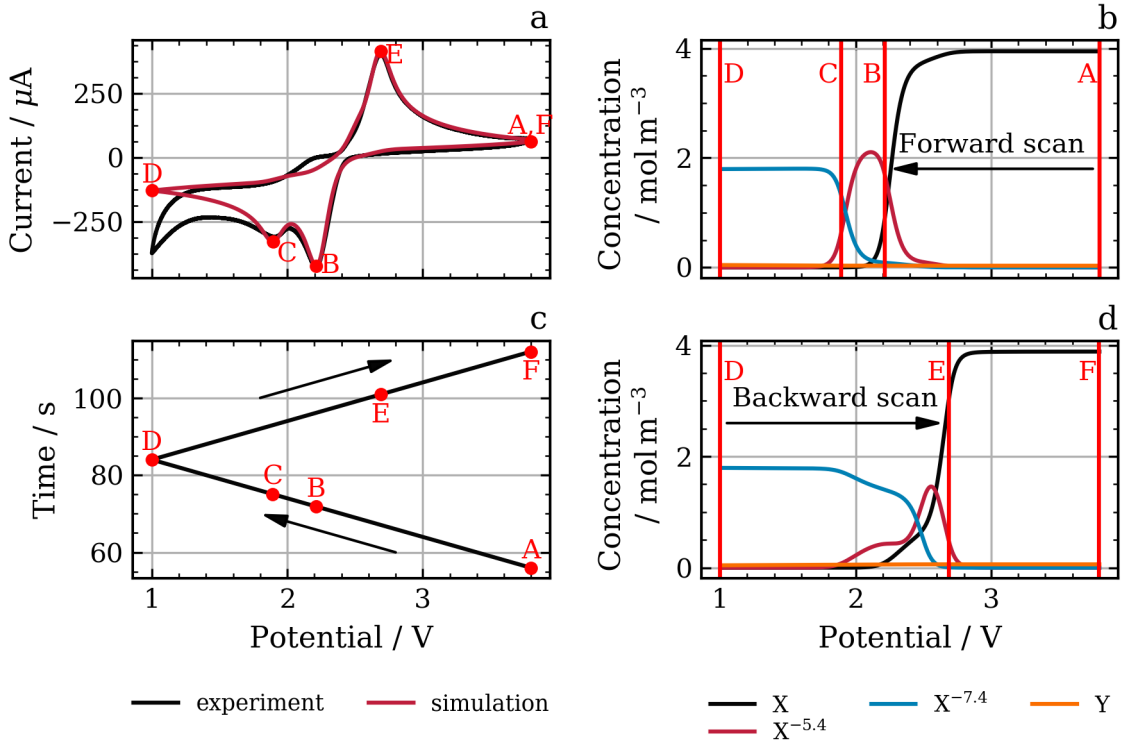

Figure 5.3: Cyclic voltammetry results of the EEC_{irr}-mechanism for a scan rate of $\nu = 100\,\mathrm{mV\,s^{-1}}$. Points A to F indicate significant states of the system (a) Simulated CV compared to experimental results of the 2nd cycle from Chapter 3. (b) Concentrations at the surface of the electrode $x_f = 0\,\mathrm{mm}$ during the forward scan and (c) the backward scan.

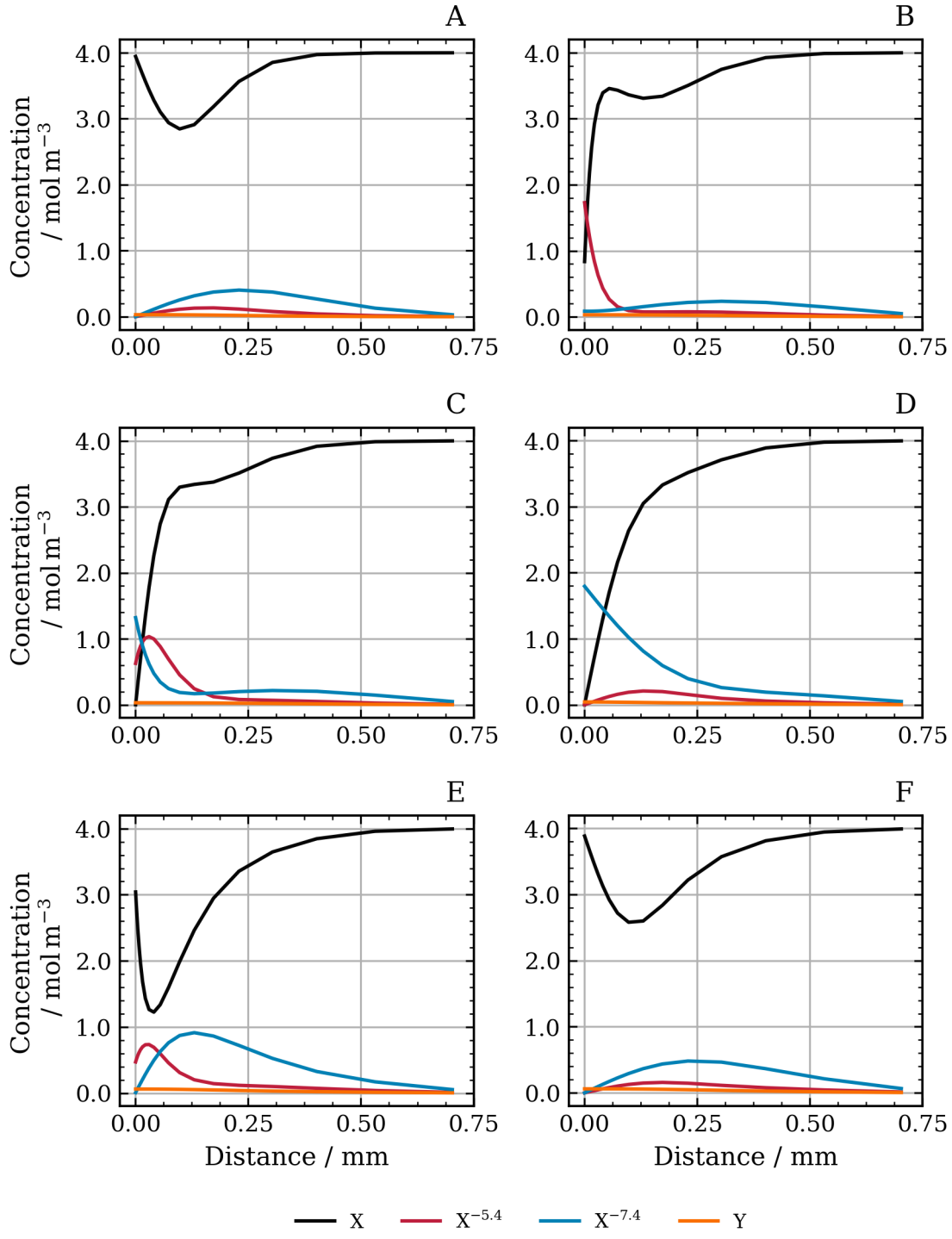

Figure 5.4: Concentration profiles of the EEC_{irr}-mechanism during CV simulation with optimized parameters with a scan rate $\nu = 100\,\mathrm{mV\,s^{-1}}$ at points A to F. Results are shown for the second cycle.

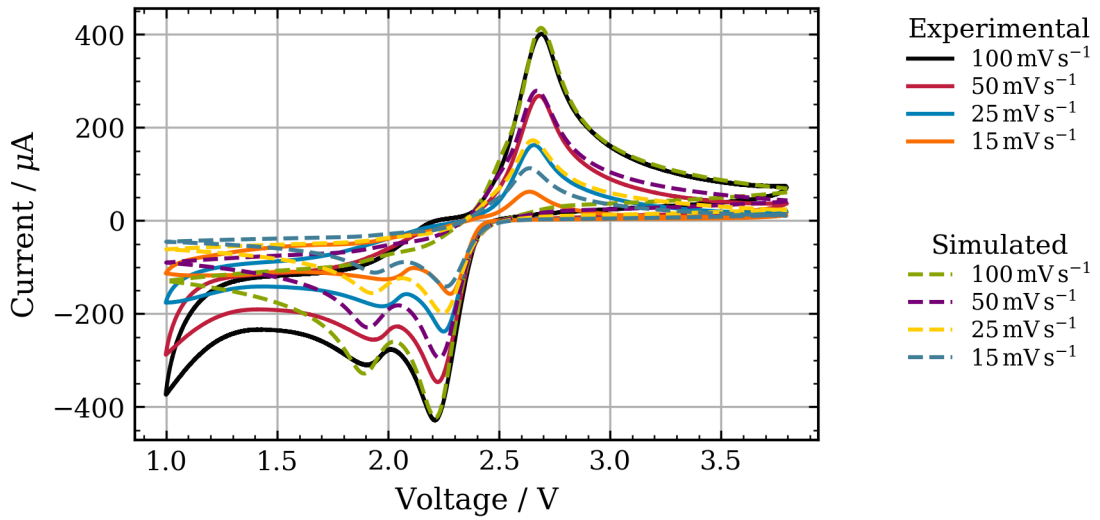

Figure 5.5: Comparison of experimental and simulation cyclic voltammetry of the 2nd cycle results vs. potential of the EEC_{irr}-mechanism evaluating scan rate dependency with 100 mV s^{-1}, 50 mV s^{-1}, 25 mV s^{-1} and 15 mV s^{-1}.

species still exist and diffuse to the surface causing a diffusion limited current.

To elucidate the above seen important role of diffusion in the CV, distinctive concentration profiles of species X, $X^{5.4-}$ and $X^{7.4-}$ vs. distance from the electrode/electrolyte interface are observable from Fig. 5.4. Sulfur (X) has a concentration minimum between the electrode/electrolyte interface and the bulk, because X is produced from $X^{5.4-}$ by reaction Ia at the end of cycle one and it is sufficiently available in the bulk. After point C, the current is dictated by the delivery of additional X via diffusion from the bulk solution causing a decrease till point D. Due to diffusion the layer at the electrode/electrolyte interface containing the reduced $X^{5.4-}$ and $X^{7.4-}$ continuously grows throughout the scan. Fig. 5.4 shows, that during dynamic operation reacting species are always in mixture with other species. Therefore, the system behavior always depends on multiple reactions and to the best of our knowledge, analytical solutions are not possible in this case. The courses of concentrations of sulfur (X), $X^{5.4-}$ and $X^{7.4-}$ are almost identical at point A and F indicating the good reversibility of the mechanism at this scan rate.

Chemical reaction IIIa is slow compared to the electron transfer reactions Ia and IIa. This results in a CV that appears reversible. Consequently, the concentration of

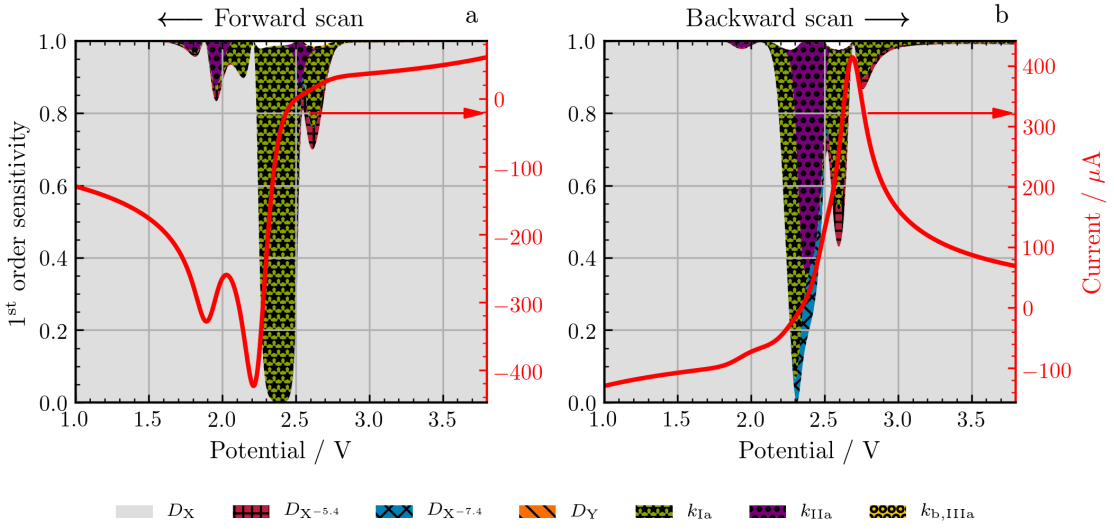

Figure 5.6: First order sensitivity results for each parameter influencing the current of the EEC_{irr}-mechanism. The values are stacked as they sum up to 1. The current (red line) is displayed for better correlation to the CV results. 16 000 simulations were recorded varying the parameters by ±10 %.

Y throughout the experiment at all places is negligible, as it can be seen in Fig. 5.4. The amount of Y produced in the chemical reaction IIIa increases as the scan rate of the experiment decreases, thereby creating a more irreversible response of the system. The ratio of the anodic to cathodic peak currents decreases because the reduced species $X^{7.4-}$ is consumed by the subsequent chemical reaction, resulting in fewer species to oxidize on the anodic scan, see Fig. 5.5.

The sensitivity of each model parameter on the observed current during a CV is displayed in Fig. 5.6; for direct correlation of the sensitivities with the current at a given potential, the current is also displayed (red line). The sum of all single parameter sensitivities at a given potential sums up to 1, and we thus the single parameter sensitivities (colored bars) stacked on each other. Each parameter sensitivity value represents the relative impact the parameter has on the current at the given potential. Over a wide range of the scan, diffusion of sulfur (X) has the largest impact. When reaching the formal potential of reaction Ia, kinetic parameters dominate and the current gets significantly influenced by the reaction rate constant of reaction Ia, until the first cathodic peak is reached. At the second cathodic peak, the sensitivity of

the current to the reaction rate constant of reaction IIa is much lower, because only a small share of the total current is added by reaction IIa. The bigger amount is added by reaction Ia, which explains the remaining strong significance of sulfur (X) diffusion.

In contrast during the backward scan, the anodic peak, displayed in Fig. 5.6b, is influenced by both reaction rate constants Ia and IIa, because these reactions overlap. The second reaction influences the beginning of the increase, therefore the current is most sensitive to $k_{\mathrm{II}a}$. When $\mathrm{X}^{7.4-}$ concentration rapidly decreases at the surface at $\sim$2.4 V, the electron transfer reaction Ia takes over and the sensitivity of $k_{\mathrm{I}a}$ is dominant.

In conclusion, the $\mathrm{EEC_{irr}}$-mechanism is able to achieve qualitative agreement with the experimental data. Pure analytical investigation of such mechanisms without the here presented macrokinetic modeling is limited as peaks and profiles are overlapping and lead to complex patterns. Therefore, simulation and identification of the parameters, as demonstrated here, is the only way of gaining a complete insight and understanding of the complex interaction of thermodynamic, kinetic and transport properties of the sulfur reaction mechanism through CV. Yet, parts of the experimental CV characteristics are missing. In particular, the $\mathrm{EEC_{irr}}$-mechanism exhibits diffusion limitation, when chemical reactions should be influencing the current. In the following section, a more physically motivated mechanism will be applied to see how the species and reactions proposed in literature interact and, together with diffusion, are able to explain CV behavior of sulfur electrodes.

E3C4-Mechanism

The E3C4-mechanism is primarily characterized by three electron transfer reactions occurring at two different formal potentials: 2.44 V for reaction Ib and IIb and 2.3 V for reaction IIIb. Compared to the $\mathrm{EEC_{irr}}$-mechanism, the electrons directly transferred by electron transfer reactions differ by $1.4\,\mathrm{e^-\,mol_{S_8}^{-1}}$. To compensate this missing charge, chemical reactions Vb, VIb and VIIb are introduced that are able to produce additional $\mathrm{S_8}$. In Fig. 5.8a the simulation results are shown in comparison to the experiment. A comparison to different scan rates is shown in Fig. 5.7. It can clearly be seen, that also this mechanism matches the experiment in good agreement regarding all relevant points. Point F deviates because of experimental electrolyte degradation,

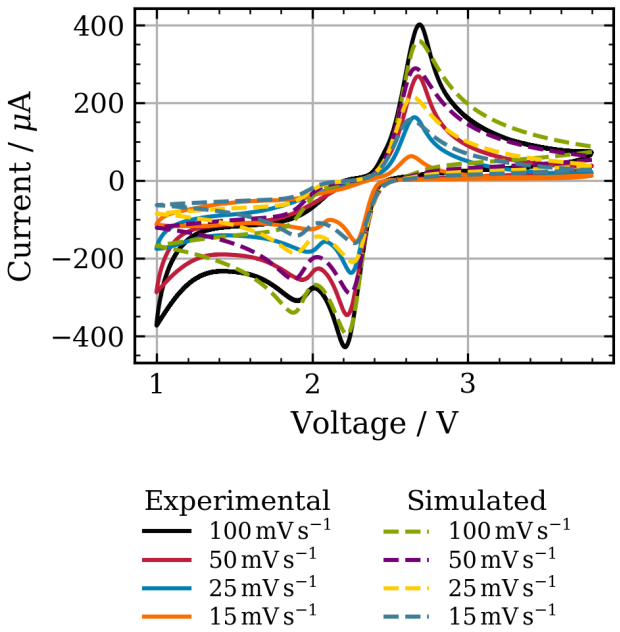

Figure 5.7: Comparison of experimental and simulation cyclic voltammetry results vs potential of the E3C4-mechanism evaluating scan rate dependency with $100\,\mathrm{mV\,s^{-1}}$, $50\,\mathrm{mV\,s^{-1}}$, $25\,\mathrm{mV\,s^{-1}}$ and $15\,\mathrm{mV\,s^{-1}}$.

as explained earlier. In contrast to the $\mathrm{EEC_{irr}}$-mechanism, the E3C4-mechanism better reproduces the two previously missing features: (i) the slow current decrease directly after point C and (ii) zero current when increasing voltage to 2 V.

During the forward scan from 3.8 V to 1.0 V, S_8 reduces to S_8^{4-} via S_8^{2-} when passing the formal potential of reaction Ib and IIb. The intermediate is only present for a short time period, see Fig. 5.8b. Reactions Ib and IIb overlap, as indicated by the single reaction currents displayed in Fig. 5.9a. Reaction Ib and IIb are related to the upper potential discharge plateau with a potential >2.3 V during galvanostatic discharge. Because of the fast chemical reaction IVb between S_8^{4-} and S_4^{2-} (Fig. 5.8c), these species exhibit a similar course in concentration over potential. In addition, the influence of the circular route through reaction Vb is obvious at a potential of 2.4 V. Chemical reaction Vb converts S_4^{2-} back to S_8 and to the smaller molecules S_2^{2-} and S^{2-}. In addition, chemical reactions VIb and VIIb run backward consuming more S_4^{2-} to produce more S_8. This drives the system to a more reduced state. The here discussed quite complex interplay of the chemical reactions causes the negative

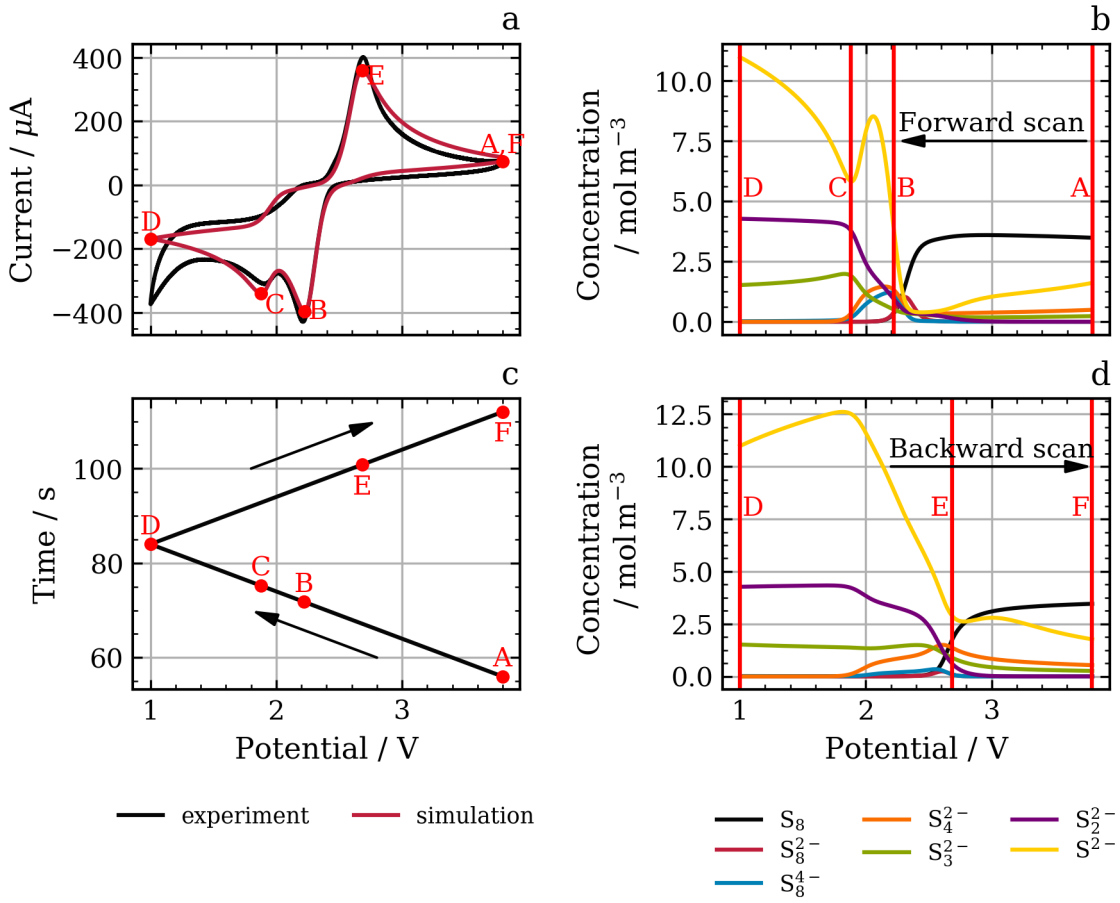

Figure 5.8: Cyclic voltammetry results of the E3C4-mechanism for a scan rate of $\nu = 100\,\mathrm{mV\,s^{-1}}$. Points A to F indicate significant states of the system and are further analyzed. (a) Simulated cyclic voltammograms of the 2$^{\mathrm{nd}}$ cycle compared to experimental results from Chapter 3 (b) Concentration at the surface of the electrode $x_\mathrm{f} = 0\,\mathrm{mm}$ during the forward scan and (c) the backward scan.

and positive reaction rates displayed in Fig. 5.9b. We thus deduces that the occurring reactions at the higher potential discharge plateau of a LIB can be summarized as follows:

$$S_8 + 2\,e^- \longrightarrow S_8^{2-} \quad \text{(Ib)}$$

$$S_8^{2-} + 2\,e^- \longrightarrow S_8^{4-} \quad \text{(IIb)}$$

$$S_8^{4-} \longrightarrow 2\,S_4^{2-} \quad \text{(IVb)}$$

$$3\,S_4^{2-} \longrightarrow S_8 + S_2^{2-} + 2\,S^{2-} \quad \text{(Vb)}$$

$$2\,S_3^{2-} \longleftarrow S_4^{2-} + S_2^{2-} \quad \text{(VIb)}$$

$$2\,S_2^{2-} \longleftarrow S_3^{2-} + S^{2-} \quad \text{(VIIb)}$$

The mechanism also clearly explains the usually observed slow but strong relaxation behavior in Li-S batteries. Though the mechanism is complex, it agrees well with the large range of polysulfides detected by HPLC analysis starting at 87.1 % SoC (Fig. 4.2).

In the following, the behavior at lower potential is discussed. At ∼2.2 V, the third electron transfer reaction IIIb of reducing S_4^{2-} to S_2^{2-} kicks in (Fig. 5.9a). As S_4^{2-} concentration decreases, the competing chemical reaction Vb and so S_8 rapidly decreases. When diffusion diminishes in addition the S_4^{2-} concentration reaction Vb even changes direction and consumes S_8 before it reaches the electrode/electrolyte interface. With both, S_8 and S_8^{4-} concentration being strongly diminished, electron transfer reactions Ib and IIb no longer contribute to the total current when reaching a potential of ∼1.8 V. In addition to the reversal of Vb due to missing S_4^{2-}, the reactions VIb and VIIb which convert S_4^{2-} with S_2^{2-} and S^{2-} are reversed as well. In summary, the lower potential discharge plateau starts, when S_8 is no longer present at the electrode/electrolyte interface, and there is a radical change in the mechanism. The only electron transfer reaction that continues is reaction IIIb. A circular route is formed that produces S_4^{2-} for the electrochemical reduction, which is an explanation for the broad CV peaks during the lower potential discharge plateau. This leads to the following reduction mechanism at the electrode/electrolyte interface which will prevail during the lower potential discharge plateau of Li-S cells:

$$S_4^{2-} + 2\,e^- \longrightarrow 2\,S_2^{2-} \quad \text{(IIIb)}$$

$$2\,S_3^{2-} \longrightarrow S_4^{2-} + S_2^{2-} \quad \text{(VIb)}$$

$$2\,S_2^{2-} \longrightarrow S_3^{2-} + S^{2-} \quad \text{(VIIb)}$$

In addition, further away from the electrode/electrolyte interface, S_8 is consumed by reaction Vb, which produces new reactant for reaction IIIB:

$$3\,S_4^{2-} \longleftarrow S_8 + S_2^{2-} + 2\,S^{2-} \quad \text{(Vb)}$$

This mechanism is much simpler than at high potential but can still explain also the observed relaxation behavior at open circuit voltage (OCV). At point D, the reversal point, the system reaches a steady state condition with constant polysulfides compositions, diffusion and constant reaction rates (Fig. 5.8). In the following we analyze the positive scan, i.e. the sulfur electrode behavior during charge.

Approaching 2.6 V, the electrochemical oxidation sets in, first of reaction IIIb, then IIb and IB (see Fig. 5.9a). The reaction rate constant of reaction IIIb is significantly lower than that of reactions Ib and IIb. Thus, the anodic peak potentials of all three electron transfer reactions are close, resulting in one anodic peak. In addition, the chemical reactions Vb, VIb and VIIb support the formation of the oxidizeable species S_2^{2-} and therefore ensure more complete oxidation of the system.This can be seen in the large amount of S_2^{2-} over a wide potential range with decreasing S_3^{2-} (Fig. 5.8c) and the strongly negative rate of VIIb and positive rate of Vb (5.9c). Note that also the S^{2-} decrease is slow due to reproduction by reaction Vb. Following Fig. 5.9c, the complete set during oxidation at the sulfur electrode is thus:

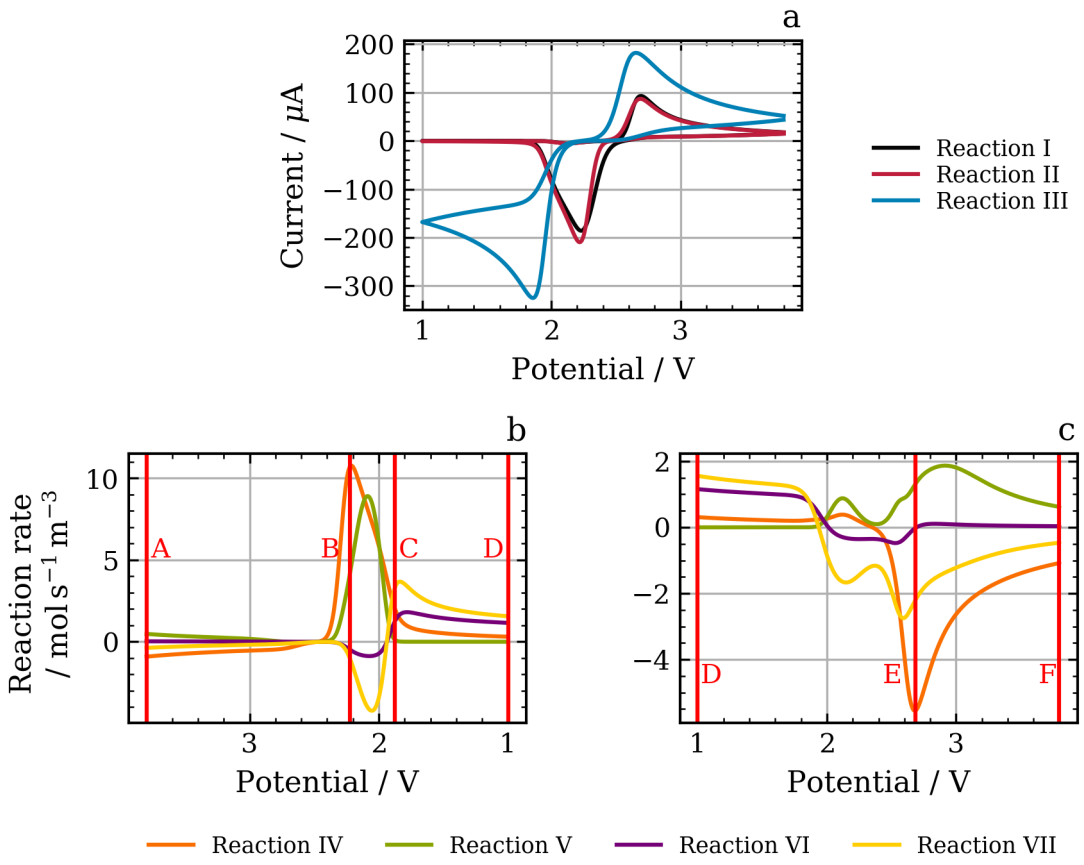

Figure 5.9: (a) Reaction currents of the implemented electron transfer reactions of the E3C4-mechanism. (b) Reaction rates of the chemical equilibrium reactions for the forward scan at the electrode surface. (c) Reaction rates of the chemical equilibrium reactions for the backward scan at the electrode surface.

$$S_8 + 2\,e^- \longleftarrow S_8^{2-} \tag{Ib}$$

$$S_8^{2-} + 2\,e^- \longleftarrow S_8^{4-} \tag{IIb}$$

$$S_4^{2-} + 2\,e^- \longleftarrow 2\,S_2^{2-} \tag{IIIb}$$

$$S_8^{4-} \longleftarrow 2\,S_4^{2-} \tag{IVb}$$

$$3\,S_4^{2-} \longrightarrow S_8 + S_2^{2-} + 2\,S^{2-} \tag{Vb}$$

$$2\,S_3^{2-} \longrightarrow S_4^{2-} + S_2^{2-} \tag{VIb}$$

$$2\,S_2^{2-} \longleftarrow S_3^{2-} + S^{2-} \tag{VIIb}$$

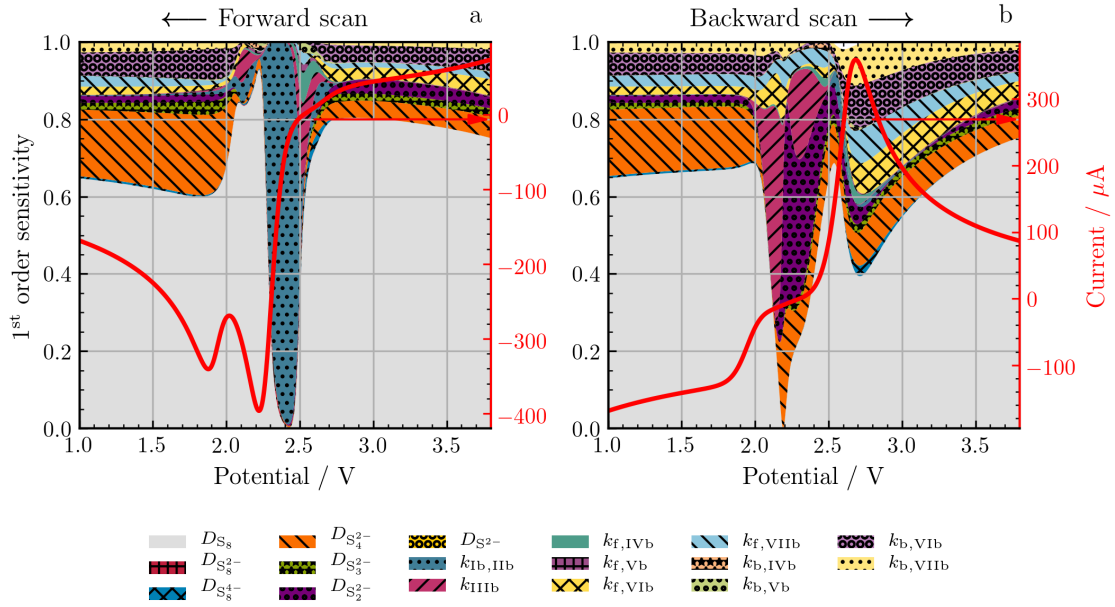

Figure 5.10: First order sensitivity results for each parameter influencing the current. The values are stacked as they sum up to 1. The current (red line) is displayed for better correlation to the CV results. 40 000 simulations were recorded varying the optimized parameters of Tab. 5.4 ±10 %.

Similar as for the EEC_{irr}-mechanism, the concentration profiles of S_8 and polysulfides in the electrolyte depend on the potential applied in course of time, see Fig. 5.4. The concentration of S_8 drops to zero at and close to the electrode/electrolyte interface after the second reduction peak (points C and D) as S_8 is more rapidly consumed than diffusing from the bulk.

Thus also in this physicochemical motivated mechanism, diffusion an even more chemical reactions in the bulk play a significant role in explaining the experimentally observed behavior in CV, and will have non negligible and complex impact on sulfur electrode behavior during charge. This will always lead to extremely complex behavior of sulfur electrodes during charge and discharge. Whereas the suggested set of electrochemical and chemical reactions may not be the only possible set explaining the CVs, it explains the HPLC and relaxation behavior well, and is thus a robust and suitable choice for analyzing, modeling and understanding typical behavior of sulfur electrodes in DOL/DME electrolyte.

Analyzing the sensitivity of the diffusion coefficients and reaction rate constants of each species and reaction on the current, the result is quite different from the EEC_{irr}-mechanism as it is much more affected by chemical reactions, see Fig. 5.10. In the kinetic limited area of the reduction reaction from 3.8 V to 2.6 V, the current is most sensitive to the diffusion of substrate from the bulk to the electrode/electrolyte interface, in this case S_8. In addition, we observe a notable sensitivity of the diffusion coefficients of the short chain polysulfides, S_4^{2-}, S_3^{2-} and S_2^{2-}, as oxidation of the short polysulfides still takes place. When reaching the first cathodic peak, the electron transfer reactions Ib and IIb show the highest sensitivity impact. This emphasizes, that the current is mainly influenced by these reactions. However as expected, the peak current is almost exclusively sensitive to the S_8 diffusion, as it strongly depends on fresh substrate to be delivered to the electrode/electrolyte interface. The peak current of the second cathodic peak is more affected by diffusion of S_4^{2-} and chemical reactions ($k_{IVb-VIIb}$). These are also important when reaching diffusion limitation. During the reverse scan, in the voltage range of 2.0 V to 2.3 V, the current's sensitivity on kinetic parameters is very high. This supports the earlier findings, that the introduction of multiple chemical reactions is necessary to reproduce and explain the experimental behavior of the sulfur electrode. The anodic peak current is strongly affected by chemical reactions, which explains its scan rate dependence that was demonstrated by the irreversible reaction when analyzing the EEC_{irr}-mechanism (Fig. 5.5). Possible irreversible processes to be included in the future are the precipitation of S_2^{2-} and S^{2-}. Introducing chemical irreversibly of either reaction Vb-VIIb does not lead to the desired result, because the equilibrium of the reaction mechanism gets disturbed.

In summary, the proposed mechanism including electron transfer reactions summarized by Wild et al. [37], and circular routes including the reproduction of S_8 [1, 35, 81] shows good agreement of the CV. Compared to the EEC_{irr}-mechanism, introducing a circular route enabled the current increase to zero at 2.0 V during the forward scan. This indicates the S_8 consumption before reaching the electrode/electrolyte interface. In addition, the circular route compensates for the missing charge because only 4 e^- per S_8 are transferred by electron transfer reactions Ib and IIb compared to 5.4 e^- for the EEC_{irr}-mechanism. In general, the current is greatly influenced by the chemical reactions Vb, VIb and VIIb.

5.6 Conclusion

In this study the reaction mechanism and kinetics at the sulfur electrode of LSBs is analyzed by physicochemical simulation of CV. Two mechanisms were introduced to evaluate the influence of diffusive transport and interaction of electron transfer and chemical reaction kinetics on the resulting current in a CV experiment. First, the kinetic model based on the EEC_{irr}-mechanism results in the desired reduction and oxidation peaks. It fails reproducing the diffusion limiting current directly after the second cathodic peak and exhibits a cathodic current that is not measured in the experiment when crossing 2.0 V during the reverse scan. Nevertheless, this mechanism can be used to replicate general sulfur electrode characteristics, which are two reduction steps and rate dependency due to chemical reactions. However, the application of this mechanism should be restricted to models, where an exact electrolyte composition is irrelevant. Studies of the shuttle mechanism or S^{2-} precipitation should use the physically motivated reaction mechanism to simulate real LSB behavior.

The second reaction kinetic model uses a more realistic and complex reaction mechanism that incorporates results of several prior research studies from literature. In addition to three electron transfer reactions, chemical reactions of short chain polysulfides have a significant impact on the behavior of the system. Throughout all SoC states, the important role of disproportionation is pointed out while the direction of different reactions and the influence of the reactions on the current varies. Strongly different prevailing reactions on the different discharge plateaus and between reduction and oxidation of the system can be seen, i.e. discharge and charge.

An important feature of the mechanism is the circular route that converts shorter polysulfides to S_8. It leads to a more reduced state of the products of the higher potential discharge plateau that could not be reproduced by the EEC_{irr}-mechanism. The presence of diverse polysulfides in the electrolyte as seen by the HPLC measurements can only be represented by the complex E3C4-mechanism, which is particularly suitable for more exact investigations of the LSB limitations like the shuttle mechanism or insulation of the electrode by S_8 or S^{2-} precipitation. Our studies emphasize that profound knowledge of the reaction mechanism and its kinetics needed to understand and control the complex electrode behavior and is therefore key to further improve LSBs performance. It is proven, that implementation of solely electron transfer reactions in LSB models is not sufficient to reproduce the real

behavior of a LSB. Future model-supported studies will exceedingly benefit when dealing with degradation, optimization of electrolyte composition or prevention of passivizing surfaces.

Chapter 6

C-rate dependence of Li-S batteries and its conjunction with reaction kinetics[1]

6.1 Introduction

Compared to current state-of-the-art LIBs a major disadvantage of LSB is the 40 % to 50 % lower discharge voltage of about 2.1 V [27, 163]. However, because of higher voltage demand of many technical applications and gain in energy density, achieving higher voltages is advantageous.

In ether-based electrolytes, typically two discharge plateaus are observed upon cycling a LSB. One at around 2.3 V to 2.4 V, the higher voltage discharge plateau, corresponding to the reduction of S_8 and long chain polysulfides down to medium chain lengths as described in Chapter 5. This plateau overall contributes to about 25 % to the overall discharge capacity. The lower voltage discharge plateau at around 2.1 V accounts for the remaining 75 % [13, 34, 164].

Fig. 6.1 shows the discharge curves of the C-rate test of cell EX1200. The dependence of the specific capacity on the C-rate is evident. Nevertheless, the contribution of each plateau should be analyzed in more detail to evaluate how transport, electron transfer and chemical processes influence the C-rate dependence of the cell. Furthermore, the comparison between the two production variations in dispersion and calendaring shows, if production parameters that increase the coatings density influence the reaction kinetics.

[1] Parts of this chapter have been published in Titscher et al. [53]

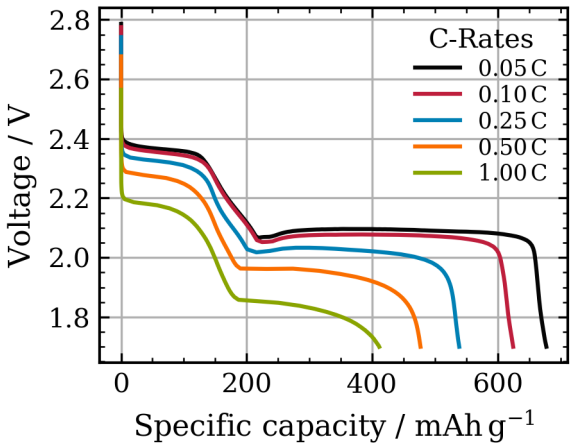

Figure 6.1: Discharge curves of the C-rate test for electrode EX1200.

6.2 Experimental set-up

Multiple LSBs are fabricated in the coin cell format. Electrode manufacturing, cell assembling and experimental characterization was done by the BatteryLab Factory Braunschweig (BLB). The results are published by Titscher et al. [53].

The cell configuration is varied in the dispersion and calendaring process. A laboratory co-rotating twin-screw extruder is used for the first dispersing step. The second dispersing process is performed using a triple-roller mill. The electrodes are calendared discontinuously with final compressions shown in Tab. 6.1. For each configuration, three cells are built and cycled between 1.7 V to 2.8 V. After five cycles at 0.1 C, a C-rate test is with the following scheme is performed: 3x0.05 C, 3x0.1 C, 3x0.25 C, 3x0.5 C and 3x0.1 C. C-rates are calculated based on the theoretical discharge capacity of S_8 with 1672 mA h $g_{S_8}^{-1}$. However, in this analysis results are related to the discharge current.

6.3 Determination of voltage plateaus

The voltages of the discharge plateaus were identified in a two-step approach. (i) The data points of the higher and lower voltage plateau are identified by the criterion $dU/dt < 0.004\,\mathrm{V\,min^{-1}}$, with U, the cell voltage. (ii) For each plateau, the mean

Table 6.1: Specifications of cathodes manufactured with various dispersing and calendering parameters. 60 wt% of the cathode consisted of S_8.

Name	Ex speed min^{-1}	TRM speed min^{-1}	Compression[a] %	Drying profile[b]	S_8 mass loading $mg\,cm^{-1}$	Coating density $g\,cm^{-2}$
Ex120	120	–	0	DP1	2.98	0.45
Ex240	240	–	0	DP1	2.98	0.47
Ex600	600	–	0	DP1	3.01	0.50
Ex1200	1200	–	0	DP1	3.10	0.56
Ex1200 + TRM	1200	480	0	DP1	3.04	0.57
Cal0 %	1200	–	0	DP2	2.92	0.60
Cal4.5 %	1200	–	4.5	DP2	2.92	0.63
Cal20 %	1200	–	20	DP2	2.92	0.72
Cal50 %	1200	–	50	DP2	2.92	0.90

a) the compression is calculated by the increase of the coating density relative to the initial coating density. b) DB1 = drying temperature 80 °C; DP2 = drying temperature 65 °C, Ex = extruder; TRM = triple-roller mill.

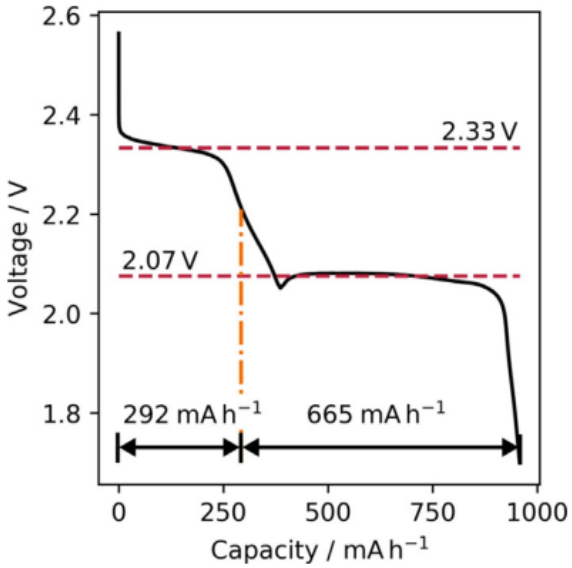

Figure 6.2: Illustration of how the discharge curve is separated in two distinct plateaus.

value of the identified data points is calculated to determine the corresponding plateau voltage. The discharge curve is separated in two parts. Therefore, the capacity of the higher voltage plateau is defined as the capacity at which the discharge voltage reaches the mean value of the two plateaus, as indicated in Fig. 6.2. The capacity of the lower voltage discharge plateau is defined as the remaining capacity from this point to breakdown.

6.4 Results and discussion

At first, the discharge curves of the samples produced with varied dispersion intensities are analyzed. The C-rate test of the cells is shown in Fig. 6.3. Only minor differences regarding the specific capacity distinguish the different cells. The best performing cells are dispersed with an extruder speed of 600 rpm. The volumetric energy increases up to an extruder speed of 600 rpm. Above 600 rpm, the difference of the volumetric energy is within the standard deviation. The cells exhibit a logarithmic dependence of the specific capacity and volumetric energy on the discharge current. The specific capacity (Fig. 6.4a) is 40 % lower when comparing 0.05 C with $\sim$710 mA h $g_{S_8}^{-1}$ to a C-rate of 1 C with $\sim$420 mA h $g_{S_8}^{-1}$. The volumetric energy, shown in Fig. 6.4b is even stronger affected by the discharge current increase. Increasing the C-rate from 0.05 C to 1 C the volumetric energy is reduced by $\sim$55 %. The causes of this current dependency is analyzed in detail by examining the two discharge plateaus of each cell in each cycle.

In the following, the discharge curve is separated in higher and lower voltage discharge plateau. The plateau voltages, specific capacities and volumetric energies are calculated and shown in Fig. 6.4. The voltage (Fig. 6.4a) has a linear dependency on the current for all examined cells. The linear decrease of voltage with current is related to the ohmic overpotential. The plateau voltage can therefore be calculated by $U = U^0 - RI$, with U^0 the open circuit voltage, R the resistance and I the current. A linear regression is performed to determine the origin, which corresponds to the OCV of the cell and the slope of the voltage decrease, which corresponds to the resistance. Overpotentials due to kinetic limitations cause a logarithmic dependency and therefore do not influence the plateau voltages. Tab. 6.2 lists the identified parameters of the linear regression. The variation of the OCV is within 0.03 V, from

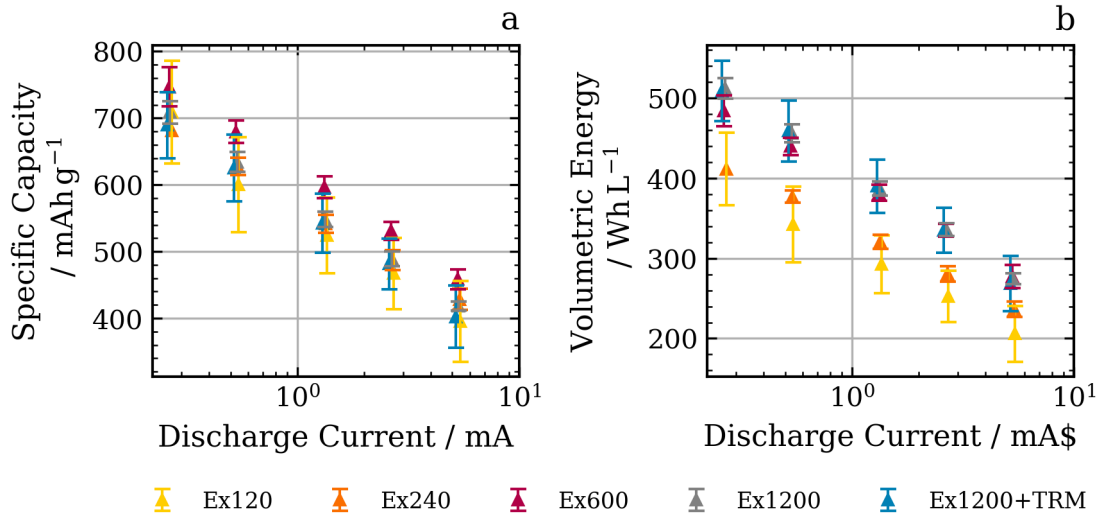

Figure 6.3: C-rate performance of lithium-sulfur cells and the analyzed cathodes processed with different dispersing intensities; specific capacity (a), and energy density on coating level (b).

2.345 f to 2.375 for the higher voltage discharge plateau and from 2.077 V to 2.106 V at the lower voltage discharge plateau.

The resistance depends on the sample. Ex600 has the lowest resistance, 0.026 Ω at the higher voltage voltage plateau and 0.036 Ω at the lower voltage discharge plateau and indicates an optimum regarding OCV and resistance. The highest resistance is calculated for Ex120 and Ex1200+TRM with 0.038 V and 0.040 V at the higher voltage discharge plateau and 0.050 Ω and 0.051 Ω at the lower voltage discharge plateau, respectively.

Comparing the specific capacity loss and the specific voltage loss between the higher and lower voltage discharge plateau, the lower voltage discharge plateau is much more dependent on the current. For example, specific capacity of Ex120 drops by 17.2 % at the higher voltage discharge plateau whereas 52.47 % of specific capacity are lost at the lower voltage discharge plateau.

As determined in the previous chapters, the higher voltage discharge plateau is primarily dependent on S_8 electron transfer reactions and therefore on the transport of S_8 to the surface as well as the circular chemical route to produce more substrate. Since mass transport of S_8 is fast and S_8 is sufficiently dispersed in the carbon matrix,

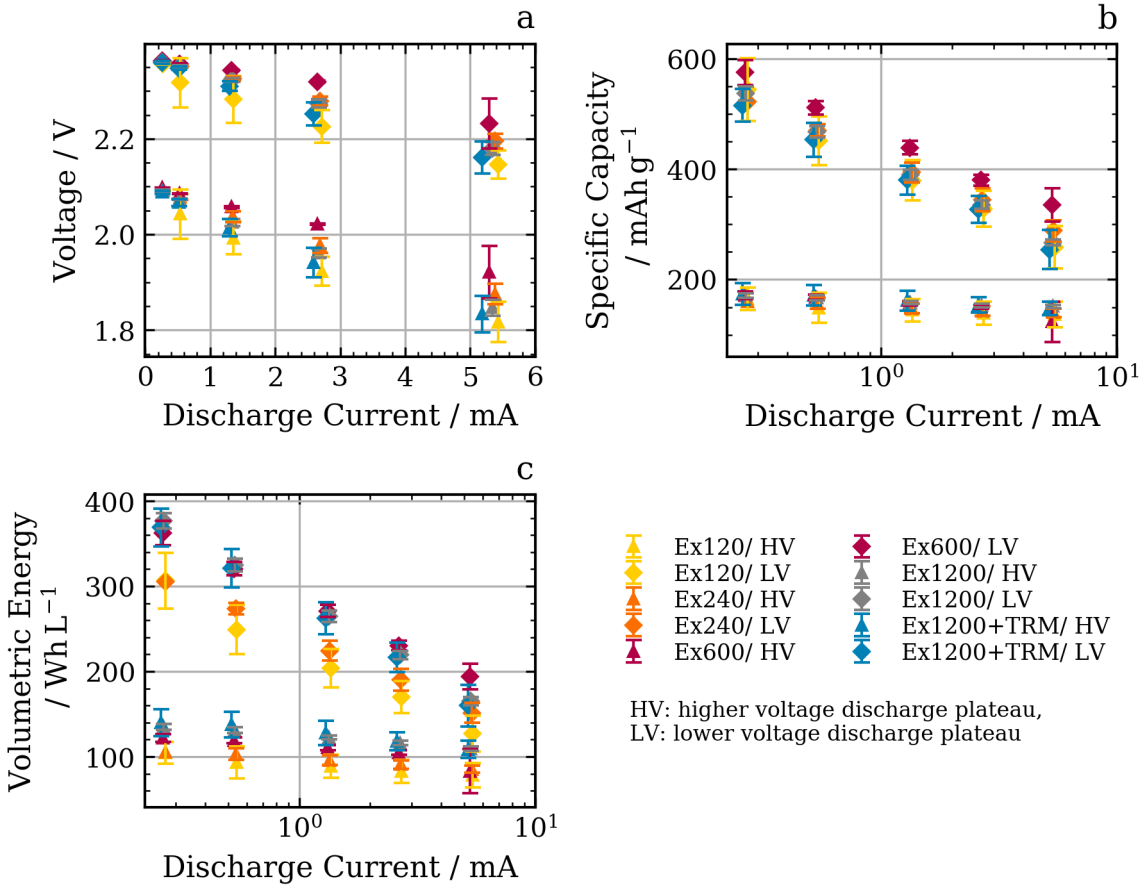

Figure 6.4: Changes of plateau voltages (a), specific capacities (b) and volumetric energies (c) in the course of the current. Cells with a fabrication variation in dispersing intensities are displayed.

Table 6.2: Voltage regression, specific capacity loss and volumetric energy loss between 0.05 C to 1 C of the higher voltage discharge plateau. The cathodes are produced at different dispersing intensities.

			Ex120	Ex240	Ex600	Ex1200	Ex1200 + TRM
			Higher voltage discharge plateau				
$U = U^0 - RI$	U^0	V	2.345	2.369	2.375	2.370	2.366
	R	Ω	0.038	0.033	0.026	0.036	0.040
Specific capacity loss		%	17.20	12.51	28.11	11.48	15.91
Volumetric energy loss		%	25.00	19.17	31.85	18.96	22.52
			Lower voltage discharge plateau				
$U = U^0 - RI$	U^0	V	2.077	2.098	2.106	2.097	2.089
	R	Ω	0.050	0.042	0.035	0.048	0.051
Specific capacity loss		%	52.47	44.71	41.72	50.29	50.66
Volumetric energy loss		%	58.46	50.46	46.39	56.20	56.67

it can be assumed, that a kinetic limitation for the chemical production of S_8 is the primary reason for the C-rate dependence of the higher voltage discharge plateau. S_8 has not vanished when reaching the lower voltage discharge plateau. More likely the concentration of polysulfides peaks and electrochemically insulating Li_2S precipitates.

At the lower voltage discharge plateau a variety of chemical reactions is responsible for production of electrochemical active species. The production is therefore time dependent explaining the strong influence of the current. At some point during discharge, chemical reaction of polysulfides become limiting for the subsequent electron transfer reaction. This is consistent with the results of the sensitivity analysis in Chapter 5.

The variation in the calendering process essentially results in the same behavior regarding its dependency on the current as previously seen. Specific capacities and volumetric energies are shown in Fig. 6.5. Again, the cells exhibit a logarithmic dependence of the specific capacity and volumetric energy on the discharge current. The volumetric energy strongly depends on the compression during calendering. The compression strongly increases the mass loading while not having a negative impact on the specific capacity.

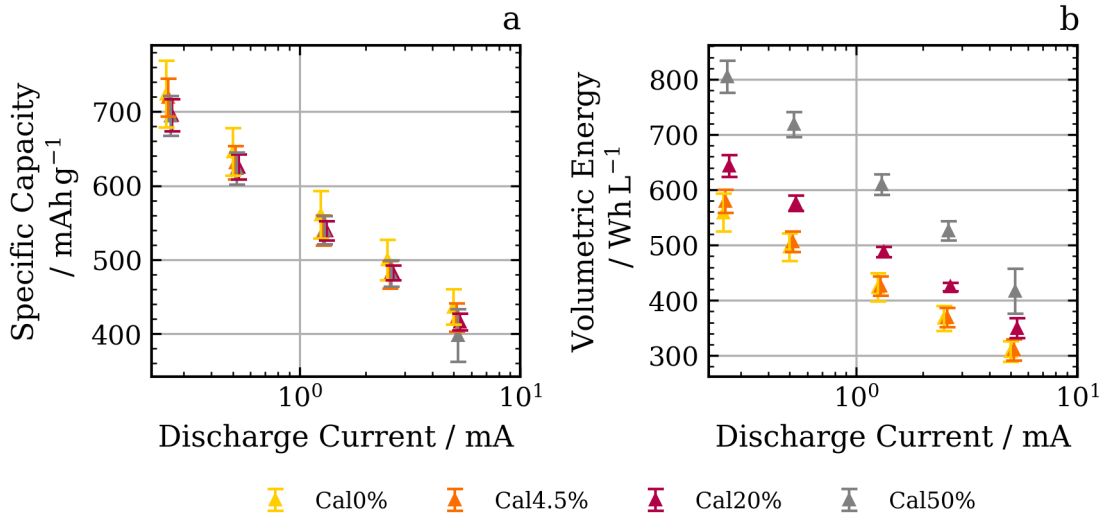

Figure 6.5: C-rate performance of lithium-sulfur cells and the analyzed cathodes (Ex1200) with different compressions after the calandering process; specific capacity (a) and energy density on coating level (b).

The behavior of the higher and lower voltage discharge plateau is slightly influenced by the compression. The OCV is decreasing, the resistance is increasing and the losses in specific capacity and volumetric energy are also increasing. This indicates some limitations that is associated with the compression of the sample. Most likely, the decreased porosity reduces the amount of electrolyte accessible for S_8 and polysulfides. This hinders the transport and electron transfer and chemical processes to occur.

6.5 Conclusion

In this study, C-rate dependency of S_8 cathodes produced with variations of dispersion intensity and compression is evaluated. The uniqueness of this investigation is the separated analysis of the higher and lower voltage discharge plateau of the LSBs. The current dependency of the plateau voltages exhibit a linear behavior for both plateaus and can therefor be attributed to the ohmic overpotential of the cell. Specific capacity and volumetric energy show a strong C-rate dependence as they are logarithmic decreasing with current. The lower voltage discharge plateau is identified as leading cause for the overall current dependency. The losses can be attributed to kinetic

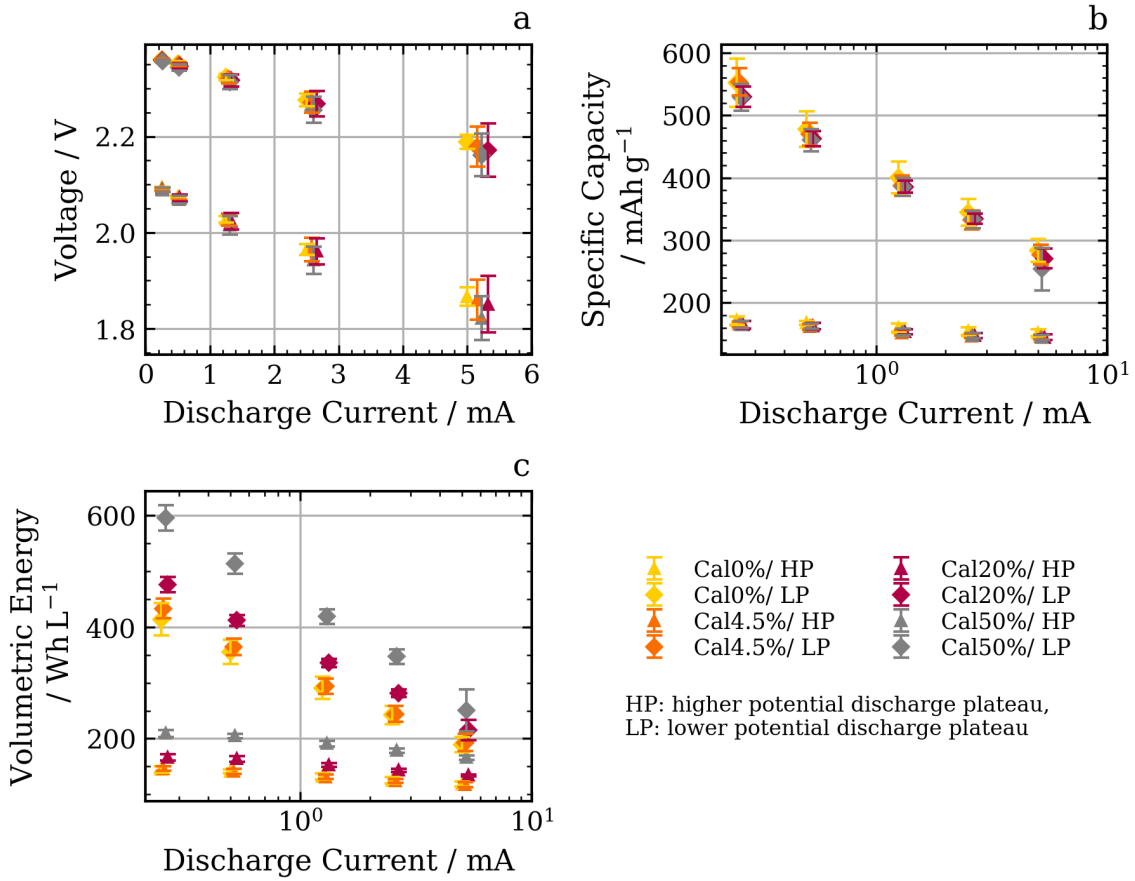

Figure 6.6: Change of plateau voltages (a), specific capacities (b) and volumetric energies (c) in the course of the current. Cathodes (Ex1200) processed with different compression are displayed.

Table 6.3: Voltage regression, specific capacity loss and volumetric energy loss between 0.05 C to 1 C of the higher voltage discharge plateau. The cathodes are produced with different compressions.

			Cal0 %	Cal4.5 %	Cal20 %	Cal50 %
			Higher voltage discharge plateau			
$U = U^0 - RI$	U^0	V	2.369	2.368	2.366	2.364
	R	Ω	0.036	0.037	0.037	0.039
Specific capacity loss		%	11.34	12.37	12.03	12.85
Volumetric energy loss		%	18.26	19.40	19.58	20.71
			Lower voltage discharge plateau			
$U = U^0 - RI$	U^0	V	2.095	2.095	2.094	2.093
	R	Ω	0.047	0.047	0.047	0.053
Specific capacity loss		%	48.61	49.95	48.94	52.04
Volumetric energy loss		%	54.37	55.52	54.82	57.96

limitations due to the high influence of chemical reactions. The importance of the chemical reactions that have been introduced in the previous chapters is therefore underlined. The limitation in reproducing new substrate for the electron transfer reaction at the lower voltage discharge plateau finally leads to the reduced specific capacity and volumetric energy at high currents. Even though the higher voltage discharge plateau includes chemical reactions to form S_8 for the electron transfer reaction, the current dependence is low, because most substrate comes from freshly dissolving S_8. Electron transfer reactions are fast enough to also not affect the plateau capacity and energy. The variations in the two examined production process steps have no major influence on the mass transfer and kinetic behavior of the LSB. Apparently, an optimization of LSBs regarding current dependency by evaluating materials has more influence than optimizing the production steps.

Chapter 7

Summary and Outlook

To pave the way to commercially competitive LSBs, fundamental insights into the reaction mechanism of S_8 reduction and the subsequent oxidation and the kinetics are provided. By applying a complementary set of chemical and electrochemical characterization methods, including CV, HPLC and galvanostatic discharge and computational simulation of CV, profound knowledge of the underlying mechanism is derived. By studying changes of relaxation behavior of galvanostatic discharge and OCP in combination with CV at different scan rates during discharge, a strong dependence of the prevailing reduction reactions and of chemical disproportionation on the SoC is determined. This includes the most probable occurring reactions and their kinetics during both of the voltage discharge plateaus. At the higher voltage discharge plateau, reduction of S_8 to S_8^{4-} in two steps is confirmed, but more specific species and chemical reactions that accompany the electrochemical reduction remain unknown. It was found by HPLC analysis, that the major polysulfide species formed during electrochemical discharge of elemental S_8 are the S_3^{2-} and S_4^{2-} species, which suggests that the chemical equilibrium of disproportionation reactions favors these. However, most polysulfides (S_x^{2-}, $x = 2 - 7$) are present at the higher and lower potential discharge plateau, confirming the strong influence of disproportionation. Precipitation of S^{2-} is mainly present at the lower potential discharge plateau. These findings have been used to suggest a suitable reaction mechanism that is implemented to a physicochemical model to simulate and analyze CV.

The first examined EEC_{irr}-mechanism represents current peaks of the CVG and scan rate dependency due to chemical reactions correctly. It is applicable to certain systems and conditions, but will not be generally be representative for S_8 reduction. In scenarios, where the electrolyte composition can be disregarded and computational costs are a crucial factor, an optimized EEC_{irr}-mechanism can be used to simulate

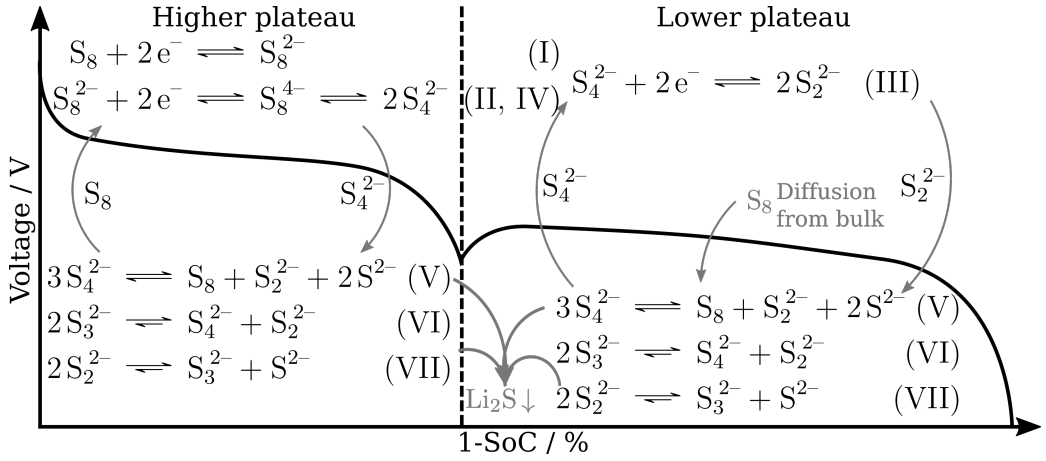

Figure 7.1: Illustration of the reaction mechanism of sulfur reduction during the two characteristic discharge plateaus.

the electrochemical behavior of a LSBs. The more complex, physically motivated E3C4-mechanism, as illustrated in Fig. 7.1, is able to model the experimental data of the CV experiment. Substantial steps already proven in the prior experimental investigations and in literature are implemented. The ability to represent the S_8 and the occurring polysulfides concentrations correctly will give superior results compared to currently published simulation studies, because there the reaction mechanism is generally simplified. This especially holds for investigation of the shuttle mechanism, electrode insulation or parasitic reactions with the electrolyte, in which the polysulfides and their concentration have an important role. The mechanisms, that is changing between the two discharge plateaus is shown in Fig. 7.1. Special regard has to be given to the circular routes that produce S_8 at the higher voltage discharge plateau and S_4^{2-} at the lower voltage discharge plateau. In addition, the changing role of S_8 between the two plateaus is remarkable. While being directly involved in the electron transfer reactions at the higher voltage discharge plateau, it is still present in the electrolyte at the lower voltage discharge plateau, but reacts chemically before reaching the surface. The electron transfer reaction of S_4^{2-} has a lower potential. From the beginning, reaction V produces S^{2-} that precipitates when reaching a certain concentration.

The separated electrochemical analysis by galvanostatic discharge of the higher and lower voltage discharge plateau of the LSBs revealed a linear decrease in plateau voltage for both plateaus, caused by ohmic overpotentials of the cell. During the

higher voltage discharge plateau, mass transport limitations were minor leading to no significant loss in specific capacity and volumetric energy with increasing current. Electron transfer reactions are fast enough to also not affect the plateau capacity. However, the chemical circular route to produce more S_8 is rate dependent and causes a decrease in specific capacity and volumetric energy.

An even stronger dependence of the specific capacity and the volumetric energy on the current is observed for the lower voltage discharge plateau. With increasing current, more S_4^{2-} has to be reduced, which either has to be already present or produced by the circular route. Therefore, the constrains are related to kinetic limitations of the ongoing chemical reactions. This is consistent with the results of the sensitivity analysis in Chapter 5, which uncovers the essential role of kinetic parameters of the chemical reactions at the lower voltage discharge plateau.

Profound knowledge of the reaction mechanism and its kinetics is key to further improve LSBs performance. It is proven, that implementation of solely electron transfer reactions is not sufficient to represent the real behavior of a LSB. Future degradation studies, optimization of electrolyte composition, which could for example include optimized dozing of electrolyte additives to suppress the shuttle mechanism, or optimized electrode design to provide sufficient electroactive surface area to not suffer from insulation, will particularly benefit from the implementation of the physically motivated mechanism. In addition, improvements in cell control can be expected, because deep insights into inner processes are exceedingly important. This could lead to overall higher voltages and better sulfur utilization, which directly increases the cell capacity. However, more work has to be done to gain comprehensive results of different LSB systems, where various electrolytes and electrode materials are used. This study therefore represents a great starting point to further investigate limiting processes of the LSB.

Appendix

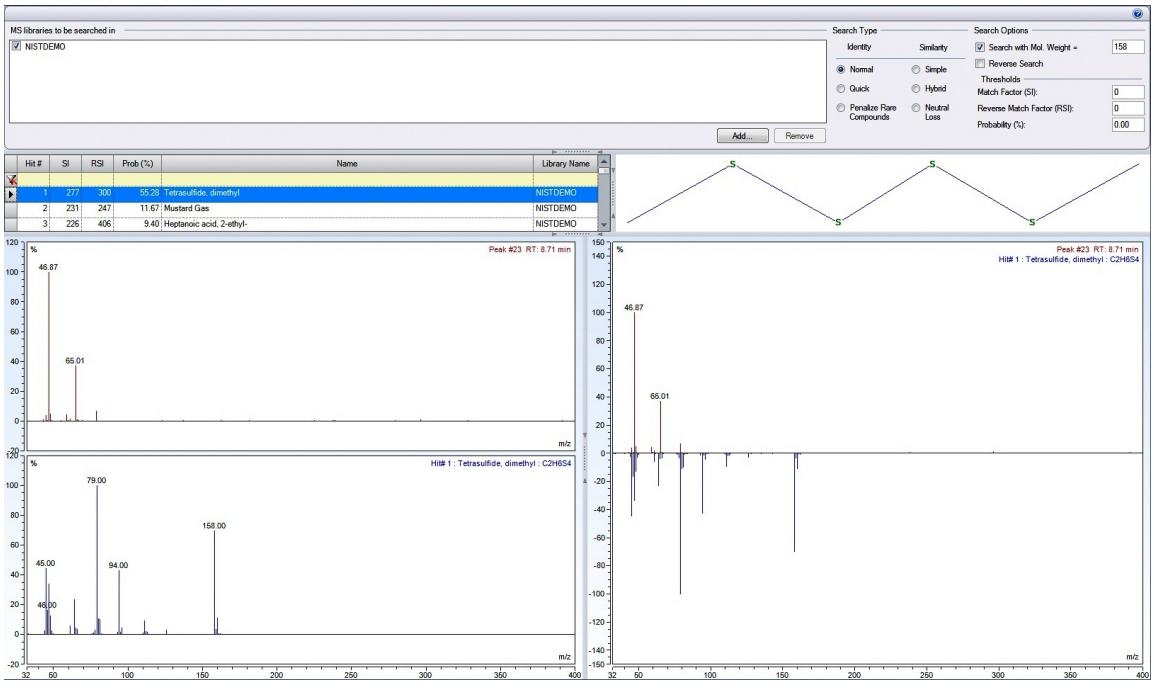

Figure 2: Identification of Me_2S_4 using Chromeleon and the NIST database

Bibliography

[1] Patrick Schön, Frederik Hintz, and Ulrike Krewer. “Electrochemical analysis of the reaction mechanism of sulfur reduction as a function of state of charge”. In: *Electrochimica Acta* 295 (2019), pp. 926–933.

[2] J-M Tarascon and Michel Armand. “Issues and challenges facing rechargeable lithium batteries”. In: *Materials for Sustainable Energy: A Collection of Peer-Reviewed Research and Review Articles from Nature Publishing Group*. World Scientific, 2011, pp. 171–179.

[3] Richard Schmuch et al. “Performance and cost of materials for lithium-based rechargeable automotive batteries”. In: *Nature Energy* 3.4 (2018), pp. 267–278.

[4] Rotem Marom et al. “A review of advanced and practical lithium battery materials”. In: *Journal of Materials Chemistry* 21.27 (2011), pp. 9938–9954.

[5] Chen-Xi Zu and Hong Li. “Thermodynamic analysis on energy densities of batteries”. In: *Energy & Environmental Science* 4.8 (2011), pp. 2614–2624.

[6] Vinodkumar Etacheri et al. “Challenges in the development of advanced Li-ion batteries: a review”. In: *Energy & Environmental Science* 4.9 (2011), pp. 3243–3262.

[7] Xin-Bing Cheng et al. “Toward safe lithium metal anode in rechargeable batteries: a review”. In: *Chemical reviews* 117.15 (2017), pp. 10403–10473.

[8] Xue-Qiang Zhang, Xin-Bing Cheng, and Qiang Zhang. “Advances in interfaces between Li metal anode and electrolyte”. In: *Advanced Materials Interfaces* 5.2 (2018), p. 1701097.

[9] Hyun Deog Yoo et al. “On the challenge of developing advanced technologies for electrochemical energy storage and conversion”. In: *Materials Today* 17.3 (2014), pp. 110–121.

[10] Yu Zhao et al. “A chemistry and material perspective on lithium redox flow batteries towards high-density electrical energy storage”. In: *Chemical Society Reviews* 44.22 (2015), pp. 7968–7996.

[11] Arumugam Manthiram, Xingwen Yu, and Shaofei Wang. “Lithium battery chemistries enabled by solid-state electrolytes”. In: *Nature Reviews Materials* 2.4 (2017), p. 16103.

[12] Feixiang Wu and Gleb Yushin. “Conversion cathodes for rechargeable lithium and lithium-ion batteries”. In: *Energy & Environmental Science* 10.2 (2017), pp. 435–459.

[13] Peter G Bruce et al. “Li-O2 and Li-S batteries with high energy storage”. In: *Nature materials* 11.1 (2012), p. 19.

[14] MN Obrovac and VL Chevrier. “Alloy negative electrodes for Li-ion batteries”. In: *Chemical reviews* 114.23 (2014), pp. 11444–11502.

[15] Iventus Power. *LITHIUM-ION POWER FOR DATA STORAGE AND SERVERS*. 2019. URL: https://inventuspower.com/lithium-ion-power-for-data-storage-and-servers/.

[16] Markus Hagen et al. “Lithium–sulfur cells: the gap between the state-of-the-art and the requirements for high energy battery cells”. In: *Advanced Energy Materials* 5.16 (2015), p. 1401986.

[17] Ian A Hunt et al. “Lithium sulfur battery nail penetration test under load”. In: *Journal of Energy Storage* 2 (2015), pp. 25–29.

[18] Abbas Fotouhi et al. “A review on electric vehicle battery modelling: From Lithium-ion toward Lithium–Sulphur”. In: *Renewable and Sustainable Energy Reviews* 56 (2016), pp. 1008–1021.

[19] Sam Estrin. *The Zephyr High Altitude Pseudo-Satellite (HAPS) Aircraft Gets Lithium Sulfur (Li-S) Batteries*. 2019. URL: https://www.droneuniversities.com/drones/the-zephyr-high-altitude-pseudo-satellite-haps-aircraft-gets-lithium-sulfur-li-s-batteries/.

[20] Ruopian Fang et al. “More reliable lithium-sulfur batteries: status, solutions and prospects”. In: *Advanced Materials* 29.48 (2017), p. 1606823.

[21] Arumugam Manthiram, Yongzhu Fu, and Yu-Sheng Su. "Challenges and prospects of lithium–sulfur batteries". In: *Accounts of chemical research* 46.5 (2012), pp. 1125–1134.

[22] Arumugam Manthiram et al. "Rechargeable lithium–sulfur batteries". In: *Chemical reviews* 114.23 (2014), pp. 11751–11787.

[23] Arumugam Manthiram, Sheng-Heng Chung, and Chenxi Zu. "Lithium–sulfur batteries: progress and prospects". In: *Advanced materials* 27.12 (2015), pp. 1980–2006.

[24] Tianyi Wang et al. "Fabrication methods of porous carbon materials and separator membranes for lithium–sulfur batteries: development and future perspectives". In: *Small Methods* 1.8 (2017), p. 1700089.

[25] Ya-Xia Yin et al. "Lithium–sulfur batteries: electrochemistry, materials, and prospects". In: *Angewandte Chemie International Edition* 52.50 (2013), pp. 13186–13200.

[26] Norman Neill Greenwood and Alan Earnshaw. *Chemistry of the Elements*. Elsevier, 2012.

[27] Xiulei Ji, Kyu Tae Lee, and Linda F Nazar. "A highly ordered nanostructured carbon-sulphur cathode for lithium-sulphur batteries". In: *Nature materials* 8.6 (2009), p. 500.

[28] Guangmin Zhou et al. "A flexible nanostructured sulphur–carbon nanotube cathode with high rate performance for Li-S batteries". In: *Energy & environmental science* 5.10 (2012), pp. 8901–8906.

[29] Meng-Qiang Zhao et al. "Graphene/single-walled carbon nanotube hybrids: one-step catalytic growth and applications for high-rate Li–S batteries". In: *ACS nano* 6.12 (2012), pp. 10759–10769.

[30] Scott Evers and Linda F Nazar. "Graphene-enveloped sulfur in a one pot reaction: a cathode with good coulombic efficiency and high practical sulfur content". In: *Chemical Communications* 48.9 (2012), pp. 1233–1235.

[31] Sen Xin et al. "Smaller sulfur molecules promise better lithium–sulfur batteries". In: *Journal of the American Chemical Society* 134.45 (2012), pp. 18510–18513.

[32] Da-Wei Wang et al. “A microporous–mesoporous carbon with graphitic structure for a high-rate stable sulfur cathode in carbonate solvent-based Li–S batteries”. In: *Physical Chemistry Chemical Physics* 14.24 (2012), pp. 8703–8710.

[33] Christian Maurer et al. “Capacity Recovery Effect in Lithium Sulfur Batteries for Electric Vehicles”. In: *World Electric Vehicle Journal* 9.2 (2018), p. 34.

[34] Sheng S Zhang. “Liquid electrolyte lithium/sulfur battery: fundamental chemistry, problems, and solutions”. In: *Journal of Power Sources* 231 (2013), pp. 153–162.

[35] Yi-Chun Lu, Qi He, and Hubert A Gasteiger. “Probing the Lithium–Sulfur Redox Reactions: A Rotating-Ring Disk Electrode Study”. In: *The Journal of Physical Chemistry C* 118.11 (2014), pp. 5733–5741.

[36] Céline Barchasz et al. “Lithium/sulfur cell discharge mechanism: an original approach for intermediate species identification”. In: *Analytical chemistry* 84.9 (2012), pp. 3973–3980.

[37] M Wild et al. “Lithium sulfur batteries, a mechanistic review”. In: *Energy & Environmental Science* 8.12 (2015), pp. 3477–3494.

[38] Zhen Li et al. “Insight into the electrode mechanism in lithium-sulfur batteries with ordered microporous carbon confined sulfur as the cathode”. In: *Advanced Energy Materials* 4.7 (2014), p. 1301473.

[39] Baogui Zhang et al. “Enhancement of long stability of sulfur cathode by encapsulating sulfur into micropores of carbon spheres”. In: *Energy & Environmental Science* 3.10 (2010), pp. 1531–1537.

[40] Zhixin Xu et al. “Enhanced performance of a lithium–sulfur battery using a carbonate-based electrolyte”. In: *Angewandte Chemie International Edition* 55.35 (2016), pp. 10372–10375.

[41] Jiulin Wang et al. “Sulfur composite cathode materials for rechargeable lithium batteries”. In: *Advanced Functional Materials* 13.6 (2003), pp. 487–492.

[42] Sheng S Zhang. “Sulfurized carbon: a class of cathode materials for high performance lithium/sulfur batteries”. In: *Frontiers in Energy Research* 1 (2013), p. 10.

[43] Feixiang Wu et al. "Harnessing Steric Separation of Freshly Nucleated Li2S Nanoparticles for Bottom-Up Assembly of High-Performance Cathodes for Lithium-Sulfur and Lithium-Ion Batteries". In: *Advanced Energy Materials* 4.11 (2014), p. 1400196.

[44] Yuan Yang et al. "New nanostructured Li2S/silicon rechargeable battery with high specific energy". In: *Nano letters* 10.4 (2010), pp. 1486–1491.

[45] Yuan Yang et al. "High-capacity micrometer-sized Li2S particles as cathode materials for advanced rechargeable lithium-ion batteries". In: *Journal of the American Chemical Society* 134.37 (2012), pp. 15387–15394.

[46] RD Rauh et al. "A lithium/dissolved sulfur battery with an organic electrolyte". In: *Journal of the Electrochemical Society* 126.4 (1979), pp. 523–527.

[47] Long Qie, Chenxi Zu, and Arumugam Manthiram. "A High Energy Lithium-Sulfur Battery with Ultrahigh-Loading Lithium Polysulfide Cathode and its Failure Mechanism". In: *Advanced Energy Materials* 6.7 (2016), p. 1502459.

[48] Ruopian Fang et al. "An integrated electrode/separator with nitrogen and nickel functionalized carbon hybrids for advanced lithium/polysulfide batteries". In: *Carbon* 109 (2016), pp. 719–726.

[49] Hongbin Yao et al. "Improving lithium–sulphur batteries through spatial control of sulphur species deposition on a hybrid electrode surface". In: *Nature communications* 5 (2014), p. 3943.

[50] Guangmin Zhou et al. "Long-life Li/polysulphide batteries with high sulphur loading enabled by lightweight three-dimensional nitrogen/sulphur-codoped graphene sponge". In: *Nature communications* 6 (2015), p. 7760.

[51] Weiyang Li et al. "Understanding the role of different conductive polymers in improving the nanostructured sulfur cathode performance". In: *Nano letters* 13.11 (2013), pp. 5534–5540.

[52] Quan Pang et al. "Surface-enhanced redox chemistry of polysulphides on a metallic and polar host for lithium-sulphur batteries". In: *Nature communications* 5 (2014), p. 4759.

[53] Paul Titscher et al. “Increasing energy densities of sulfur cathodes via dispersing and calendering processes for lithium-sulfur batteries”. In: *Energy Technology* (2018).

[54] Ge Zhang et al. “A toolbox for lithium–sulfur battery research: methods and protocols”. In: *Small Methods* 1.7 (2017), p. 1700134.

[55] Da-Wei Wang et al. “Carbon–sulfur composites for Li–S batteries: status and prospects”. In: *Journal of Materials Chemistry A* 1.33 (2013), pp. 9382–9394.

[56] Lars Borchardt, Martin Oschatz, and Stefan Kaskel. “Carbon materials for lithium sulfur batteries—ten critical questions”. In: *Chemistry–A European Journal* 22.22 (2016), pp. 7324–7351.

[57] Ji Liang et al. “Carbon materials for Li–S batteries: functional evolution and performance improvement”. In: *Energy Storage Materials* 2 (2016), pp. 76–106.

[58] Jin Won Kim et al. “Functionalized Graphene-Based Cathode for Highly Reversible Lithium–Sulfur Batteries”. In: *ChemSusChem* 7.5 (2014), pp. 1265–1273.

[59] Hailiang Wang et al. “Graphene-wrapped sulfur particles as a rechargeable lithium–sulfur battery cathode material with high capacity and cycling stability”. In: *Nano letters* 11.7 (2011), pp. 2644–2647.

[60] Liwen Ji et al. “Graphene oxide as a sulfur immobilizer in high performance lithium/sulfur cells”. In: *Journal of the American Chemical Society* 133.46 (2011), pp. 18522–18525.

[61] Andreas F Hofmann, David N Fronczek, and Wolfgang G Bessler. “Mechanistic modeling of polysulfide shuttle and capacity loss in lithium–sulfur batteries”. In: *Journal of Power Sources* 259 (2014), pp. 300–310.

[62] Kevin N Wood et al. “Dendrites and pits: Untangling the complex behavior of lithium metal anodes through operando video microscopy”. In: *ACS central science* 2.11 (2016), pp. 790–801.

[63] Hui Wu et al. “Improving battery safety by early detection of internal shorting with a bifunctional separator”. In: *Nature communications* 5 (2014), p. 5193.

[64] Yayuan Liu et al. "Lithium-coated polymeric matrix as a minimum volume-change and dendrite-free lithium metal anode". In: *Nature communications* 7 (2016), p. 10992.

[65] Michael A Pope and Ilhan A Aksay. "Structural design of cathodes for Li-S batteries". In: *Advanced Energy Materials* 5.16 (2015), p. 1500124.

[66] Zhe Yuan et al. "Powering lithium–sulfur battery performance by propelling polysulfide redox at sulfiphilic hosts". In: *Nano letters* 16.1 (2016), pp. 519–527.

[67] Weiyang Li et al. "High-performance hollow sulfur nanostructured battery cathode through a scalable, room temperature, one-step, bottom-up approach". In: *Proceedings of the National Academy of Sciences* 110.18 (2013), pp. 7148–7153.

[68] Abbas Fotouhi et al. "Lithium-sulfur battery technology readiness and applications—a review". In: *Energies* 10.12 (2017), p. 1937.

[69] Johan Scheers, Sébastien Fantini, and Patrik Johansson. "A review of electrolytes for lithium–sulphur batteries". In: *Journal of Power Sources* 255 (2014), pp. 204–218.

[70] Ninie SA Manan et al. "Electrochemistry of sulfur and polysulfides in ionic liquids". In: *The Journal of Physical Chemistry B* 115.47 (2011), pp. 13873–13879.

[71] RD Rauh et al. "Formation of lithium polysulfides in aprotic media". In: *Journal of Inorganic and Nuclear Chemistry* 39.10 (1977), pp. 1761–1766.

[72] F Gaillard and E Levillain. "Visible time-resolved spectroelectrochemistry: application to study of the reduction of sulfur (S8) in dimethylformamide". In: *Journal of Electroanalytical Chemistry* 398.1-2 (1995), pp. 77–87.

[73] E Levillain et al. "On the understanding of the reduction of sulfur (S8) in dimethylformamide (DMF)". In: *Journal of Electroanalytical Chemistry* 420.1-2 (1997), pp. 167–177.

[74] F Gaillard et al. "Polysulphides in dimethylformamide: a micro-Raman spectroelectrochemical study". In: *Journal of Raman spectroscopy* 28.7 (1997), pp. 511–517.

[75] Dong-Hun Han et al. "Time-resolved in situ spectroelectrochemical study on reduction of sulfur in N, N'-dimethylformamide". In: *Journal of The Electrochemical Society* 151.9 (2004), E283–E290.

[76] Enyue Zhao et al. "Advanced characterization techniques in promoting mechanism understanding for lithium–sulfur batteries". In: *Advanced Functional Materials* 28.38 (2018), p. 1707543.

[77] Anne Berger et al. "The importance of chemical reactions in the charging process of lithium-sulfur batteries". In: *Journal of The Electrochemical Society* 165.7 (2018), A1288–A1296.

[78] Rajeev S Assary, Larry A Curtiss, and Jeffrey S Moore. "Toward a molecular understanding of energetics in Li–S batteries using nonaqueous electrolytes: a high-level quantum chemical study". In: *The Journal of Physical Chemistry C* 118.22 (2014), pp. 11545–11558.

[79] Natalia A Canas et al. "Investigations of lithium–sulfur batteries using electrochemical impedance spectroscopy". In: *Electrochimica Acta* 97 (2013), pp. 42–51.

[80] Zhaofeng Deng et al. "Electrochemical impedance spectroscopy study of a lithium/sulfur battery: modeling and analysis of capacity fading". In: *Journal of The Electrochemical Society* 160.4 (2013), A553–A558.

[81] Yongju Jung et al. "Effect of organic solvents and electrode materials on electrochemical reduction of sulfur". In: *Int. J. Electrochem. Sci* 3.5 (2008), pp. 566–577.

[82] Ayako Kawase et al. "Electrochemical reactions of lithium–sulfur batteries: an analytical study using the organic conversion technique". In: *Physical Chemistry Chemical Physics* 16.20 (2014), pp. 9344–9350.

[83] Natalia A Cañas et al. "Experimental and theoretical analysis of products and reaction intermediates of lithium–sulfur batteries". In: *The Journal of Physical Chemistry C* 118.23 (2014), pp. 12106–12114.

[84] Jie Gao et al. "Effects of liquid electrolytes on the charge–discharge performance of rechargeable lithium/sulfur batteries: electrochemical and in-situ X-ray absorption spectroscopic studies". In: *The Journal of Physical Chemistry C* 115.50 (2011), pp. 25132–25137.

[85] Marine Cuisinier et al. “Sulfur speciation in Li–S batteries determined by operando X-ray absorption spectroscopy”. In: *The Journal of Physical Chemistry Letters* 4.19 (2013), pp. 3227–3232.

[86] Michael A Lowe, Jie Gao, and Héctor D Abruña. “Mechanistic insights into operational lithium–sulfur batteries by in situ X-ray diffraction and absorption spectroscopy”. In: *RSC Advances* 4.35 (2014), pp. 18347–18353.

[87] Johanna Nelson et al. “In operando X-ray diffraction and transmission X-ray microscopy of lithium sulfur batteries”. In: *Journal of the American Chemical Society* 134.14 (2012), pp. 6337–6343.

[88] Sylwia Waluś et al. “New insight into the working mechanism of lithium–sulfur batteries: in situ and operando X-ray diffraction characterization”. In: *Chemical Communications* 49.72 (2013), pp. 7899–7901.

[89] Jin-Tak Yeon et al. “Raman spectroscopic and X-ray diffraction studies of sulfur composite electrodes during discharge and charge”. In: *Journal of The Electrochemical Society* 159.8 (2012), A1308–A1314.

[90] Heng-Liang Wu et al. “In Situ EQCM Study Examining Irreversible Changes the Sulfur–Carbon Cathode in Lithium–Sulfur Batteries”. In: *ACS applied materials & interfaces* 7.37 (2015), pp. 20820–20828.

[91] Laura A Huff et al. “Identification of lithium–sulfur battery discharge products through 6 Li and 33 S solid-state MAS and 7 Li solution NMR spectroscopy”. In: *Surface Science* 631 (2015), pp. 295–300.

[92] Kimberly A See et al. “Ab initio structure search and in situ 7Li NMR studies of discharge products in the Li–S battery system”. In: *Journal of the American Chemical Society* 136.46 (2014), pp. 16368–16377.

[93] Jie Xiao et al. “Following the transient reactions in lithium–sulfur batteries using an in situ nuclear magnetic resonance technique”. In: *Nano letters* 15.5 (2015), pp. 3309–3316.

[94] W Zhu et al. “Investigation of the reaction mechanism of lithium sulfur batteries in different electrolyte systems by in situ Raman spectroscopy and in situ X-ray diffraction”. In: *Sustainable Energy & Fuels* 1.4 (2017), pp. 737–747.

[95] Qiang Wang et al. "Direct observation of sulfur radicals as reaction media in lithium sulfur batteries". In: *Journal of The Electrochemical Society* 162.3 (2015), A474–A478.

[96] Yuriy V Mikhaylik and James R Akridge. "Polysulfide shuttle study in the Li/S battery system". In: *Journal of the Electrochemical Society* 151.11 (2004), A1969–A1976.

[97] Karthikeyan Kumaresan, Yuriy Mikhaylik, and Ralph E White. "A mathematical model for a lithium–sulfur cell". In: *Journal of The Electrochemical Society* 155.8 (2008), A576–A582.

[98] Timo Danner et al. "Modeling of nano-structured cathodes for improved lithium-sulfur batteries". In: *Electrochimica Acta* 184 (2015), pp. 124–133.

[99] Vaclav Knap et al. "A self-discharge model of Lithium-Sulfur batteries based on direct shuttle current measurement". In: *Journal of Power Sources* 336 (2016), pp. 325–331.

[100] Karsten Propp et al. "Multi-temperature state-dependent equivalent circuit discharge model for lithium-sulfur batteries". In: *Journal of Power Sources* 328 (2016), pp. 289–299.

[101] Monica Marinescu, Teng Zhang, and Gregory J Offer. "A zero dimensional model of lithium–sulfur batteries during charge and discharge". In: *Physical Chemistry Chemical Physics* 18.1 (2016), pp. 584–593.

[102] Derek Moy, A Manivannan, and SR Narayanan. "Direct measurement of polysulfide shuttle current: A window into understanding the performance of lithium-sulfur cells". In: *Journal of the electrochemical society* 162.1 (2015), A1–A7.

[103] Teng Zhang et al. "Modelling transport-limited discharge capacity of lithium-sulfur cells". In: *Electrochimica acta* 219 (2016), pp. 502–508.

[104] David N Fronczek and Wolfgang G Bessler. "Insight into lithium–sulfur batteries: Elementary kinetic modeling and impedance simulation". In: *Journal of power sources* 244 (2013), pp. 183–188.

[105] Marzieh Barghamadi et al. "Lithium–sulfur batteries—the solution is in the electrolyte, but is the electrolyte a solution?" In: *Energy & Environmental Science* 7.12 (2014), pp. 3902–3920.

[106] Holger Schneider et al. "On the electrode potentials in lithium-sulfur batteries and their solvent-dependence". In: *Journal of The Electrochemical Society* 161.9 (2014), A1399–A1406.

[107] Dong Zheng et al. "Reduction mechanism of sulfur in lithium–sulfur battery: From elemental sulfur to polysulfide". In: *Journal of Power Sources* 301 (2016), pp. 312–316.

[108] Hong-Jie Peng et al. "Strongly coupled interfaces between a heterogeneous carbon host and a sulfur-containing guest for highly stable lithium-sulfur batteries: mechanistic insight into capacity degradation". In: *Advanced Materials Interfaces* 1.7 (2014), p. 1400227.

[109] Allen J Bard and Larry R Faulkner. *Fundamentals and Applications, New York: Wiley, 2001*. Springer, 2002.

[110] Dong Zheng et al. "Quantitative chromatographic determination of dissolved elemental sulfur in the non-aqueous electrolyte for lithium-sulfur batteries". In: *Journal of the Electrochemical Society* 162.1 (2015), A203–A206.

[111] Dong Zheng et al. "Investigation of the Li–S battery mechanism by real-time monitoring of the changes of sulfur and polysulfide species during the discharge and charge". In: *ACS applied materials & interfaces* 9.5 (2016), pp. 4326–4332.

[112] Dong Zheng et al. "Quantitative and Qualitative Determination of Polysulfide Species in the Electrolyte of a Lithium–Sulfur Battery using HPLC ESI/MS with One-Step Derivatization". In: *Advanced Energy Materials* 5.16 (2015), p. 1401888.

[113] Yan Diao et al. "Shuttle phenomenon–the irreversible oxidation mechanism of sulfur active material in Li–S battery". In: *Journal of Power Sources* 235 (2013), pp. 181–186.

[114] Chong Yan et al. "Lithium-Anode Protection in Lithium–Sulfur Batteries". In: *Trends in Chemistry* (2019).

[115] Jianming Zheng et al. "How to obtain reproducible results for lithium sulfur batteries?" In: *Journal of The Electrochemical Society* 160.11 (2013), A2288–A2292.

[116] Xiang Chen et al. "Combining theory and experiment in lithium–sulfur batteries: Current progress and future perspectives". In: *Materials Today* 22 (2019), pp. 142–158.

[117] Tom Cleaver et al. "Perspective—commercializing lithium sulfur batteries: are we doing the right research?" In: *Journal of The Electrochemical Society* 165.1 (2018), A6029–A6033.

[118] Irving Shain and Richard S Nicholson. "Theory of stationary electrode polarography: single scan and cyclic methods applied to reversible, irreversible, and kinetic systems." In: *Anal. Chem* 36 (1964), pp. 706–23.

[119] Compton Richard Guy, Laborda Eduardo, et al. *Understanding voltammetry: simulation of electrode processes*. World Scientific, 2013.

[120] Frank Marken, Andreas Neudeck, and Alan M Bond. "Cyclic voltammetry". In: *Electroanalytical methods*. Springer, 2010, pp. 57–106.

[121] David K Gosser. *Cyclic voltammetry: simulation and analysis of reaction mechanisms*. Vol. 43. VCH New York, 1993.

[122] Jianming Zheng et al. "Ionic liquid-enhanced solid state electrolyte interface (SEI) for lithium–sulfur batteries". In: *Journal of Materials chemistry A* 1.29 (2013), pp. 8464–8470.

[123] John EB Randles. "A cathode ray polarograph. Part II.—The current-voltage curves". In: *Transactions of the Faraday Society* 44 (1948), pp. 327–338.

[124] A Ševčik. "Oscillographic polarography with periodical triangular voltage". In: *Collection of Czechoslovak Chemical Communications* 13 (1948), pp. 349–377.

[125] Allen J Bard, György Inzelt, and Fritz Scholz. *Electrochemical dictionary*. Springer Science & Business Media, 2008.

[126] Jürgen Heinze. "Cyclic voltammetry—"electrochemical spectroscopy". New analytical methods (25)". In: *Angewandte Chemie International Edition in English* 23.11 (1984), pp. 831–847.

[127] Michael D Ryan. "The Effect of Slow Two-Electron Transfers and Disproportionation on Cyclic Voltammograms". In: *Journal of The Electrochemical Society* 125.4 (1978), pp. 547–555.

[128] Adrian W Bott, Stephen W Feldberg, and Manfred Rudolph. "Fitting Experimental Cyclic Voltammetry Data with Theoretical Simulations Using DigiSim [R] 2.1". In: *Current Separations* 15 (1996), pp. 67–71.

[129] LesŁaw K Bieniasz. "ELSIM—a problem-solving environment for electrochemical kinetic simulations. Version 3.0-solution of governing equations associated with interfacial species, independent of spatial coordinates or in one-dimensional space geometry". In: *Computers & chemistry* 21.1 (1997), pp. 1–12.

[130] M Rudolph. "DigiElch ver. 2.0". In: *Friedrich-Schiller-Universität: Jena, Germany* (2005).

[131] Carlo Nervi. "ESP Electrochemical Simulation Package". In: (1994).

[132] Jay H Brown. "Development and use of a cyclic voltammetry simulator to introduce undergraduate students to electrochemical simulations". In: *Journal of Chemical Education* 92.9 (2015), pp. 1490–1496.

[133] Shuo Wang, Jing Wang, and Yanjing Gao. *Development and use of an open-source, user-friendly package to simulate voltammetry experiments*. 2017.

[134] Noam Eliaz and Eliezer Gileadi. *Physical Electrochemistry: Fundamentals, Techniques, and Applications*. Wiley-Vch, 2018.

[135] Serban C Moldoveanu and Victor David. *Essentials in modern HPLC separations*. Newnes, 2012.

[136] Sandie Lindsay. *Einführung in die HPLC*. Vieweg, 1996.

[137] Bogusław Buszewski et al. "Chemically bonded silica stationary phases: synthesis, physicochemical characterization, and molecular mechanism of reversed-phase HPLC retention". In: *Analytical Chemistry* 69.16 (1997), pp. 3277–3284.

[138] Fritz Hartmann Frimmel and Michael Uwe Kumke. "Optische Parameter zur Stoffcharakterisierung vom Trinkwasser bis zum Abwasser". In: (1999).

[139] Anders Pettersson et al. "Measurement of aerosol optical extinction at 532nm with pulsed cavity ring down spectroscopy". In: *Journal of Aerosol Science* 35.8 (2004), pp. 995–1011.

[140] Edmond de Hoffmann and Vincent Strooband. *Mass Spectrometry*. John Wiley & Sons, Ltd, 2007.

[141] Carl H Hamann and Wolf Vielstich. *Elektrochemie*. Wiley-VCH-Verlag, 1998.

[142] VS Kolosnitsyn, EV Kuzmina, and EV Karaseva. "On the reasons for low sulphur utilization in the lithium–sulphur batteries". In: *Journal of Power Sources* 274 (2015), pp. 203–210.

[143] VS Kolosnitsyn et al. "A study of the electrochemical processes in lithium–sulphur cells by impedance spectroscopy". In: *Journal of Power Sources* 196.3 (2011), pp. 1478–1482.

[144] Lijiang Wang et al. "A quantum-chemical study on the discharge reaction mechanism of lithium-sulfur batteries". In: *Journal of Energy Chemistry* 22.1 (2013), pp. 72–77.

[145] Alexey Kamyshny et al. "Equilibrium distribution of polysulfide ions in aqueous solutions at 25 C: a new approach for the study of polysulfides' equilibria". In: *Environmental science & technology* 38.24 (2004), pp. 6633–6644.

[146] Dong Zheng and Deyang Qu. "Chromatographic Separation of Polysulfide Species in Non-Aqueous Electrolytes–Revisited". In: *Journal of The Electrochemical Society* 161.6 (2014), A1164–A1166.

[147] A. Kramida et al. NIST Atomic Spectra Database (ver. 5.7.1), [Online]. Available: https://physics.nist.gov/asd [2017, April 9]. National Institute of Standards and Technology, Gaithersburg, MD. 2019.

[148] Patrick Schön and Ulrike Krewer. "Revealing the complex sulfur reduction mechanism using cyclic voltammetry simulation". In: *Electrochimica Acta* 373 (2021), p. 137523.

[149] Ulrike Krewer et al. "Impedance spectroscopic analysis of the electrochemical methanol oxidation kinetics". In: *Journal of Electroanalytical Chemistry* 589.1 (2006), pp. 148–159.

[150] Qing Mao and Ulrike Krewer. "Total harmonic distortion analysis of oxygen reduction reaction in proton exchange membrane fuel cells". In: *Electrochimica Acta* 103 (2013), pp. 188–198.

[151] Fabian Kubannek et al. “Concentration pulse method for the investigation of transformation pathways in a glycerol-fed bioelectrochemical system”. In: *Frontiers in Energy Research* 6 (2018), p. 125.

[152] Ilya M Sobol. “Global sensitivity indices for nonlinear mathematical models and their Monte Carlo estimates”. In: *Mathematics and computers in simulation* 55.1-3 (2001), pp. 271–280.

[153] Andrea Saltelli. “Making best use of model evaluations to compute sensitivity indices”. In: *Computer physics communications* 145.2 (2002), pp. 280–297.

[154] Andrea Saltelli et al. “Variance based sensitivity analysis of model output. Design and estimator for the total sensitivity index”. In: *Computer Physics Communications* 181.2 (2010), pp. 259–270.

[155] John Crank et al. *The mathematics of diffusion*. Oxford university press, 1979.

[156] Scott D Cohen, Alan C Hindmarsh, and Paul F Dubois. “CVODE, a stiff/nonstiff ODE solver in C”. In: *Computers in physics* 10.2 (1996), pp. 138–143.

[157] Alan C Hindmarsh et al. “SUNDIALS: Suite of nonlinear and differential/algebraic equation solvers”. In: *ACM Transactions on Mathematical Software (TOMS)* 31.3 (2005), pp. 363–396.

[158] CF Curtiss and Joseph O Hirschfelder. “Integration of stiff equations”. In: *Proceedings of the National Academy of Sciences of the United States of America* 38.3 (1952), p. 235.

[159] Youcef Saad and Martin H Schultz. “GMRES: A generalized minimal residual algorithm for solving nonsymmetric linear systems”. In: *SIAM Journal on scientific and statistical computing* 7.3 (1986), pp. 856–869.

[160] Christian Andersson, Claus Führer, and Johan Åkesson. “Assimulo: A unified framework for ODE solvers”. In: *Mathematics and Computers in Simulation* 116 (2015), pp. 26–43.

[161] Jonathan D Herman and Will Usher. “SALib: An open-source Python library for Sensitivity Analysis.” In: *J. Open Source Software* 2.9 (2017), p. 97.

[162] Yelena Gorlin et al. “Understanding the Charging Mechanism of Lithium-Sulfur Batteries Using Spatially Resolved Operando X-Ray Absorption Spectroscopy”. In: *Journal of The Electrochemical Society* 163.6 (2016), A930–A939. DOI: 10.1149/2.0631606jes. URL: https://doi.org/10.1149%2F2.0631606jes.

[163] Michel Armand and J-M Tarascon. “Building better batteries”. In: *Nature* 451.7179 (2008), pp. 652–657.

[164] Dominic Bresser, Stefano Passerini, and Bruno Scrosati. “Recent progress and remaining challenges in sulfur-based lithium secondary batteries–a review”. In: *Chemical communications* 49.90 (2013), pp. 10545–10562.